Titre: Title:	Transient and Local Increase in the Permeability of the Blood-Brain Barrier and the Blood-Retinal Barrier by Hyperthermia of Magnetic Nanoparticles in a Rat Model
Auteur: Author:	Seyed Nasrollah Tabatabaei Shafie
Date:	2015
Type:	Mémoire ou thèse / Dissertation or Thesis
Référence: Citation:	Tabatabaei Shafie, S. N. (2015). Transient and Local Increase in the Permeability of the Blood-Brain Barrier and the Blood-Retinal Barrier by Hyperthermia of Magnetic Nanoparticles in a Rat Model [Thèse de doctorat, École Polytechnique de Montréal]. PolyPublie. https://publications.polymtl.ca/1830/

URL de PolyPublie: PolyPublie URL:	https://publications.polymtl.ca/1830/
Directeurs de recherche: Advisors:	Sylvain Martel, & Hélène Girouard
Programme: Program:	Génie biomédical

UNIVERSITÉ DE MONTRÉAL

TRANSIENT AND LOCAL INCREASE IN THE PERMEABILITY OF THE
BLOOD-BRAIN BARRIER AND THE BLOOD-RETINAL BARRIER BY
HYPERTHERMIA OF MAGNETIC NANOPARTICLES IN A RAT MODEL

SEYED NASROLLAH TABATABAEI SHAFIE

INSTITUT DE GÉNIE BIOMÉDICAL

ÉCOLE POLYTECHNIQUE DE MONTRÉAL

THÈSE PRÉSENTÉE EN VUE DE L'OBTENTION

DU DIPLÔME DE PHILOSOPHIÆ DOCTOR

(GÉNIE BIOMÉDICAL)

AOÛT 2015

UNIVERSITÉ DE MONTRÉAL

ÉCOLE POLYTECHNIQUE DE MONTRÉAL

Cette thèse intitulée :

TRANSIENT AND LOCAL INCREASE IN THE PERMEABILITY OF THE BLOOD-BRAIN BARRIER AND THE BLOOD-RETINAL BARRIER BY HYPERTHERMIA OF MAGNETIC NANOPARTICLES IN A RAT MODEL

présentée par : TABATABAEI SHAFIE Seyed Nasrollah

en vue de l'obtention du diplôme de : Philosophiæ Doctor

a été dûment acceptée par le jury d'examen constitué de :

M. SAVARD Pierre, Ph. D., président

M. MARTEL Sylvain, Ph. D., membre et directeur de recherche

Mme GIROUARD Hélène, Ph. D., membre et codirectrice de recherche

M. COHEN-ADAD Julien, Ph. D., membre

M. FORTIN David, Ph. D., membre externe

DEDICATION

First and foremost I would like to thank my research advisors, **Dr. Sylvain Martel** and **Dr. Hélène Girouard.** Dr. Martel's trust in me and my academic decisions, and Dr. Girouard's constant support and considerate mentorship provided me with a perfect atmosphere to nourish my curiosity and develop critical thinking. I would like to thank **Diane Vallerand** for her patience in answering my questions regardless of how dull they may have sounded. In addition, I would like to thank **Charles Tremblay** for his honest friendship and great technical support.

The past seven years conducting research at the **Nanorobotics Laboratory (Polytechnique)** has been quite a thrilling venture and most exciting part of my life. It has also been an honour that during the past four years I have been a member of the **Cerebrovascular Laboratory (UdM)** with its unique liberal, friendly yet professional environment.

Great gratitude goes to my family for their support of all my life choices. My parents **Reza** and **Monir**, I dedicate this to you both, for you have never limited my dreams and provided me with all I have ever asked for and more. You are the reason I have any interest in science and higher education. My sisters, **Zahra**, **Maryam** and **Mahdieh**, I thank you for your constant spiritual and a significant source of moral support. Finally and certainly not the least, I would like to thank my beloved wife, **Mona**, for being the light of my life and simply *being*; your faith in me is well cherished.

"There is only one virtue in the world, knowledge, and only one sin, ignorance, and in between, having open eyes or being blind is the difference between an informed and an uninformed man."

- *Avicenna 1740*

ACKNOWLEDGMENT

RÉSUMÉ

Après avoir réussi à propulser des agents thérapeutiques encapsulés dans des micro-transporteurs magnétiques à un endroit précis à l'intérieur d'un modèle animal en utilisant le gradient de champ magnétique dans un appareil de résonance magnétique (RM) modifié, nous visons maintenant à livrer une drogue localement dans le système nerveux central (SNC). Afin de réussir la livraison de la drogue de façon localisée et augmenter l'efficacité du traitement, ce projet met de l'avant que les agents thérapeutiques doivent être administrés par des moyens pas plus envahissants qu'une injection intraveineuse, suivis par la propulsion à distance, contrôlée, et actionnée sur commande dans le SNC.

La fonction exigeante du tissu neuronal dans le SNC (haute sensibilité/complexité du système) nécessite un environnement extrêmement stable. Un changement minime dans la composition du liquide interstitiel dans le SNC peut jouer un rôle prépondérant dans la régulation de son microenvironnement et de l'activité neuronale. Par conséquent, le SNC est conçu pour se protéger des fluctuations fréquentes de la concentration extracellulaire d'hormones, d'acides aminés, et des niveaux d'ions produits après les repas, l'exercice ou le stress (ainsi que d'agents pathogènes toxiques qui peuvent être en circulation dans le sang). Cette protection du SNC est permise grâce à la présence d'une barrière, nommée barrière hémato-encéphalique (BHE). Cette barrière préventive se compose essentiellement de cellules endothéliales étroitement reliées entre elles qui tapissent la surface intérieure de la plupart des vaisseaux sanguins dans le SNC. Bien que ceci offre un environnement neuronal stable, plus de 98% des molécules que constituent les drogues ne sont pas en mesure de franchir la BHE et leur pénétration est uniquement déterminée par les caractéristiques de perméabilité de la barrière. Ceci est alors un frein pour les traitements ciblant le SNC. Par conséquent, la recherche pharmaceutique fait un réel effort pour maximiser la livraison des médicaments vers le SNC. Pour autant, la présence des barrières physiologiques, bien qu'essentielles à la survie en conditions physiologiques, limitent les traitements qu'on a à notre disposition en conditions pathologiques. La perspective thérapeutique novatrice détaillée dans cette thèse est d'ouvrir localement et transitoirement la BHE pour permettre aux drogues thérapeutiques de diffuser au sein du SNC. Cette technique pourrait fortement augmenter la possibilité de traiter divers troubles neurologiques dans le cadre clinique.

Au niveau préclinique, nous proposons ici d'utiliser des nanoparticules magnétiques (NPM), mises de pair avec un champ magnétique alternatif. Le but étant d'augmenter la perméabilité de la barrière pour livrer une drogue de façon transitoire. Les NPM peuvent agir comme des sources de chaleur miniaturisées qui, sous l'influence du champ magnétique alternatif, dissipent de l'énergie thermique directement et exclusivement à la barrière (hyperthermie). En plus de cette nouveauté, les résultats confirment que cette technique ne porte pas atteinte à l'unité neurovasculaire, comme les neurones, les astrocytes, etc. Cette expérience in-vivo démontre que l'approche proposée va au-delà d'anciennes méthodes utilisées pour accéder au tissu du SNC. Notamment, une précision spatiale plus élevée, un meilleur contrôle et l'absence apparente de réaction immunitaire. L'ensemble des capacités de suivi et de mobilité (technologie RM), ainsi que l'hyperthermie, combinés, permettent aux NPM (composant principal du mécanisme de délivrance de médicament) d'être livrées au SNC de façon non-invasive. En raison de sa simplicité et de sa spécificité, cette technique peut entraîner d'énormes impacts économiques et sociaux au niveau de la qualité de vie des patients diagnostiqués avec des troubles liés au SNC.

ABSTRACT

After successfully propelling therapeutic agents encapsulated in magnetic micro-carriers to a specific location inside an animal model by the gradient magnetic field of a modified clinical Magnetic Resonance (MR) scanner, we are now aiming to perform local drug delivery in the region of the central nervous system (CNS). To achieve localized drug delivery and increase efficacy, this project advances the theme that the therapeutic agents must be administered by means no more invasive than an intravenous injection followed by remote propulsion, controlled tracking, and on-command actuation in the CNS.

The demanding function of the CNS requires an extremely stable environment. In fact, any small change in the composition of the interstitial fluid in the CNS plays a predominant role in regulating its microenvironment and neuronal activity. Therefore, the CNS is conceived to protect itself from frequent fluctuations of extracellular concentration of hormones, amino acids, and ion levels that occur after meals, exercise, or stress - as well as from toxic pathogens that may be circulating in the blood stream. This preventive barrier consists mainly of tightly interconnected endothelial cells that carpet the inner surface of most blood vessels in the CNS. While it provides a stable neuronal environment, more than 98% of all drug molecules are not able to cross this barrier and the extent to which a molecule enters is determined only by the permeability characteristics of the barrier. Therefore, while pharmaceutical research progresses for drug delivery to the CNS, it is limited by its pharmacokinetics through physiological barriers. Successful transient and local opening of the barrier for diffusion of therapeutics could strongly support the feasibility of treating a variety of neurological disorders.

A recent effort presented in this dissertation provides evidence for the emergence of a novel approach to overcome this problem. This technique uses magnetic nanoparticles (MNPs) in conjunction with an alternating magnetic field to transiently increase barrier permeability for drug delivery. MNPs can act as miniaturized heat sources that, when under the influence of the alternating magnetic field, dissipate thermal energy directly and exclusively to the barrier (hyperthermia). In addition to its novelty, the findings confirm that the technique does not damage the neurovascular unit, i.e. neurons, astrocytes, etc. This *in vivo* investigation provides evidence that the proposed approach goes beyond former methods to access the CNS tissue with higher spatial precision, advanced control and apparent absence of immune reaction. Evidently,

the ensemble of tracking and displacement abilities (MR technology), as well as hyperthermia, makes MNPs a principal component of the proposed non-invasive targeted drug delivery mechanism to the CNS. Because of its simplicity and specificity, this technique can introduce an enormous economical and social impact on quality of the life of patients diagnosed with CNS-related disorders.

TABLE OF CONTENTS

LIST OF TABLES

LISTE OF FIGURES

LIST OF ACRONYMS AND ABBREVIATIONS

BBB	Blood-Brain Barrier
BRB	Blood-Retinal Barrier
BTB	Blood-Tumour Barrier
CNS	Central Nervous System
CP	Cardiac Perfusion
EB	Evans Blue dye
GBM	Glioblastoma Multiforme
HIFU	High Intensity Focused Ultrasound
H_2O-dd	Double Distilled Water
ICNIRP	International Commission on Non-Ionizing Radiation Protection
ICV	Intracerebro-ventricular
LPS	Lipopolysaccharide
MBs	Micro-Bubbles
MNPs	Magnetic Nanoparticle
MRI	Magnetic Resonance Imaging
MRN	Magnetic Resonance Navigation
Na-F	Sodium Fluorescein
PBS	Phosphate Buffer Solution
PGA	Polyglycolic acid
PLGA	Poly(lactic-co-glycolic acid)
PMO-MNPs	Poly (Maleic acid-co-Olefin) coated Magnetic Nanoparticles
RF	Radiofrequency Field
SAR	Specific Absorption Rate

SLP	Specific Loss Power
TEM	Transmission Electron Microscopy
Tf-MNPs	Transferrin conjugated Magnetic Nanoparticles
VSM	Vibrating Sample Magnetometer
WHO	World Health Organization

LIST OF APPENDICES

LIST OF FIGURES IN APPENDICES

CHAPTER 1   INTRODUCTION

The emergence of a clinically viable targeted drug delivery technique for the Central Nervous System (CNS) can have a profound impact on the life of millions of people around the world. In this essential and complex collective-dream technique, therapeutics are monitored and propelled inside the vasculature of the patient towards a region of interest. Once at the target, the therapeutic molecules actively cross into the CNS and locally combat the malignancies at play. To orchestrate this important venture, it is absolutely crucial that the multidisciplinary team of researchers work in harmony. To achieve this harmony, it is essential to be aware of constrain in all aspects of the project and compromise accordingly. Therefore, while other members of the team research monitoring and propulsion of therapeutics in the vasculature, the present doctoral thesis focuses on therapeutics traversing from the vascular system to the parenchymal tissue of the CNS.

1.1 Introductory concepts

According to the latest report from the world health organization (WHO) [1], neurological disorders constitute the highest percentage of the global burden of disease (6.3%). This has contributed to 92 million disabilities in 2005 and it is projected that this number will increase to 103 million in 2030. These disorders include brain tumour. According to the brain tumour foundation of Canada [2], it is estimated that every day 27 Canadians are diagnosed with a brain tumour. Among these, the first and second year relative survival rates for some brain tumours such as the glioblastoma multiforme (GBM) are reportedly 29.6% and 9.0%, respectively [3]. Another example of an aggressive tumour that occurs in the developing retina of children is retinoblastoma. The worldwide incidence of this type of tumour is about 9,000 new cases every year [4] and it can lead to death within 1-2 years if left untreated. This extremely low life expectancy is due to high cytotoxic side effects of the therapeutic molecules on healthy cells, and of course low penetration rate of the medication to the CNS that subsequently leads to increase in dosage and therefore higher cytotoxic side effects. A preventive barrier that carpets the inner layer of most capillaries in the CNS is inarguably responsible for the lack of effective penetration of therapeutics in the tissue. While the main function of this selectively permeable barrier is to

protect the sensitive microenvironment of the CNS, overcoming it would have a great effect on the treatment of many CNS-related disorders.

1.2 Hypothesis and goals

In this doctoral dissertation, a novel technique for local delivery of large therapeutic molecules to the CNS is hypothesized and investigated. This technique is based on local elevation of endothelium temperature – hyperthermia – by magnetically excited magnetic nanoparticles (MNPs). Studies of the CNS barrier under hyperthermia have subsequently provided evidence that upon application of a radiofrequency magnetic field, the thermal energy released from MNPs can remotely, locally, and transiently increase barrier permeability in a rat model. There are many advantages to the proposed technique over others used to deliver therapeutics to the CNS; hyperthermia of MNPs operates at relatively low focal temperatures (maximum of 41 °C) and the heat is dissipated uniquely to the surface of the endothelial cells without compromising other cell types in the neurovascular unit (neurons and glia). Also, the barrier opening process is transient, as it has shown complete recovery within two hours. In addition, the use of the radiofrequency magnetic field to heat the MNPs makes this technique very effective in deep biological structures. Finally, this technique can easily be adapted to the monitoring and propulsion techniques already developed by other members of the team for targeted drug delivery [5].

Magnetic properties of the MNPs with respect to hyperthermia were previously investigated and presented as a master's degree dissertation [6]. In this doctoral thesis, the objective is to apply the findings to open CNS barrier in a rat model. This work is done in 3 phases:

Phase 1, a proof of concept with the use of an external heating apparatus on the skull of an anaesthetized mouse.

Phase 2, transient opening of the CNS barrier in the brain parenchyma with MNPs in a rat model.

Phase 3, enhanced targeting and opening of the CNS barrier in the retinal tissue with MNPs coated with transferrin in a rat model.

In this presentation, there will be a brief section on the theoretical background of the proposed technique (Chapter 2), followed by the project rationale (Chapter 3), and published peer-review articles (Chapter 4 and Chapter 5). The latest results on disruption will be presented in **Error! Reference source not found.**, followed by a general discussion (Chapter 7) and conclusion.

CHAPTER 2   THEORETICAL BACKGROUND

2.1 CNS barrier

The inner lining of all capillaries in the mammalian body including humans are composed of endothelial cells [7]. With the exception of those in the CNS, the capillaries are fenestrated to allow for rapid exchange of molecules between blood vessels and surrounding tissue. In the CNS very complex inter-endothelial tight junctions interconnect the endothelial cells (Figure 2.1). The tight junctions seal the cell interspace and form a diffusion barrier that markedly controls the flow of molecules across the epithelium. This unique vascular structure greatly contributes to the blood-brain barrier (BBB) in the brain and the blood-retinal barrier (BRB) in the ocular organ. A functioning BBB limits the passage of microscopic organisms (bacteria, viruses, etc.) and large or hydrophilic molecules into the cerebrospinal fluid while allowing diffusion of small electrically neutral lipid-soluble compounds with low molecular mass of less than 400-500 Daltons (Da) [8]–[10]. This barrier also keeps the neurotransmitters and agents that act in the CNS separate from the peripheral tissue and the blood, so that similar agents can be used in the two systems without 'crosstalk' [11]. Similarly, the BRB maintains the specialized environment of the retina and provides necessary nutrients to the eye while protecting it from toxic pathogens that may be circulating in the blood stream. By extension, more than 98% of acting biomolecules, including most anticancer drug molecules and available therapeutics are not able to reach the CNS following systemic administration [7], [12]. On the other hand, systemic administration of drugs causes the active principles to distribute throughout the body and organs and may promote side effects. The highly selective permeability of BBB and BRB, and the cytotoxicity of certain drugs reinforce the importance of non-invasive localized drug delivery to the CNS.

The BBB and the BRB are very sensitive to a broad spectrum of physiological changes that are manifest as detectable leaks of molecules from the blood into the extracellular compartment of the CNS. While manipulating the barrier is essential to drug delivery, consequences of increased barrier permeability may lead to accumulation of unwanted molecules and concomitant disruption in normal CNS function. In order to minimize subsequent risks, it is highly recommended that the CNS barrier opening technique be localized, transient, and immune-friendly.
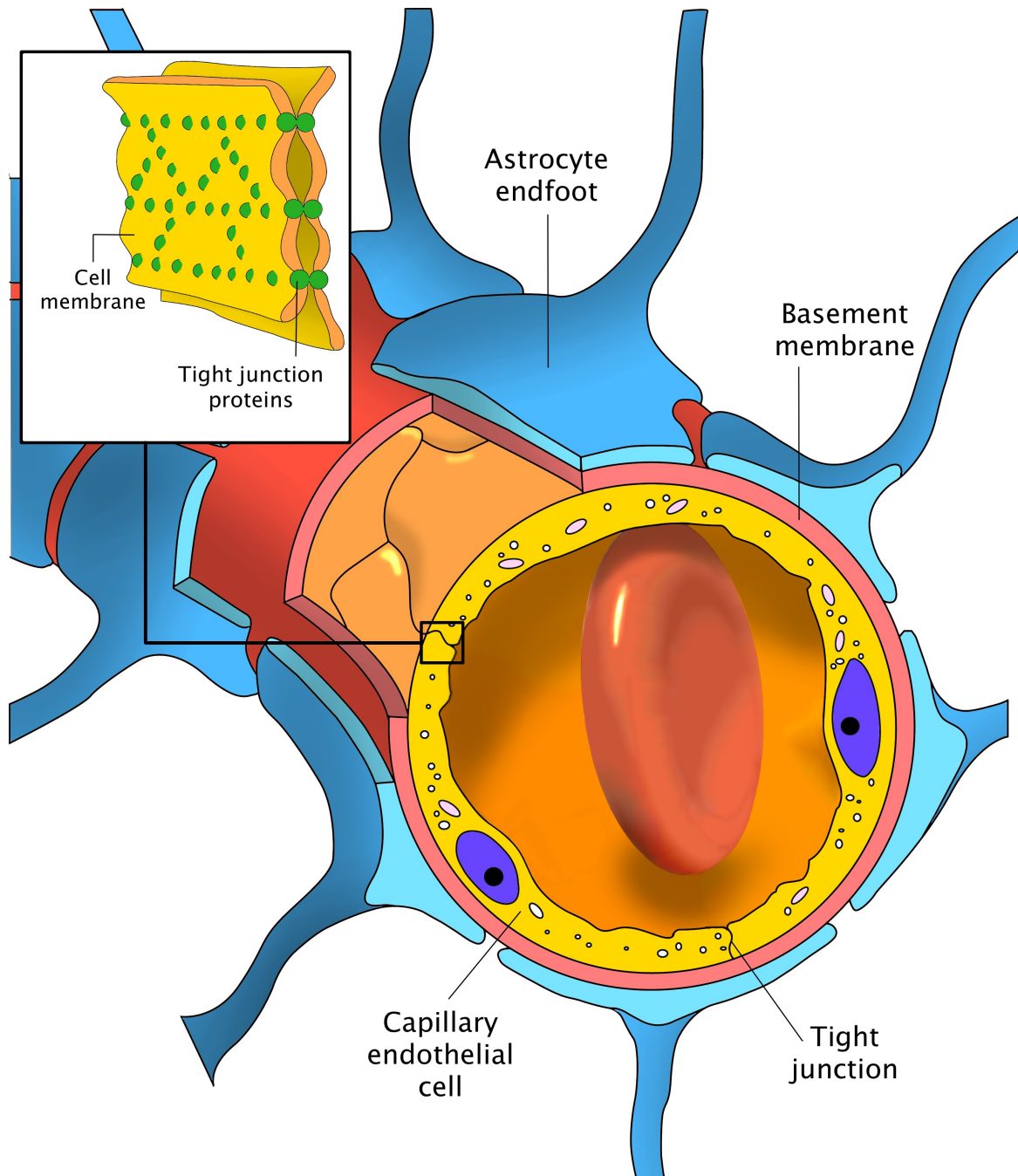
Figure 2.1: Schematics of a single capillary in the CNS

The capillaries in the CNS mostly consist of endothelial cells that are tightly interconnected and form a selective barrier. It protects the CNS from intrusive substances that could harm or alter CNS functionality. However, this also includes most drug molecules to enter the CNS.

2.2 Drug delivery to CNS

Drug delivery to the CNS remains a challenge mainly because the tightly interconnected endothelial cells (tight junctions) constitute a barrier that is reputed to be insurmountable. Following systemic administration, a functioning BBB in the brain and the BRB in the eye prevent entry of nearly 98% of drugs such as peptides, recombinant proteins, monoclonal antibodies, antisense and non-viral gene medicines to combat brain and ocular related disorders [7], [12], [13]. Due to the large surface area of the BBB (180 cm^2 per gram brain [10]), as well as the short diffusion distance between neurons and capillaries (8 – 20 μm [14]), the extent to which a molecule enters the brain is determined only by the permeability characteristics of the BBB. Similarly, drug delivery across the BRB in the highly dense microvasculature of the retina faces the same restriction. Current popular drug delivery strategies to the brain may be classified as being either invasive (Table 1) or non-invasive (Table 2). The invasive approaches require either a craniotomy, intracerebro-ventricular (ICV) infusion of drugs, or intra-cerebral implants. The non-invasive drug delivery approaches include physiological stimuli (insulin or transferrin receptor mediated transcytosis), chemical stimuli (prodrug approach such as antibody directed enzyme system) [15], biological stimuli (molecular Trojan horse approach) [16], and physical stimuli including colloidal carrier system techniques (self microemulsifying / nanoemulsifying drug delivery systems) [12]. Likewise, ocular drug delivery approaches across the BRB consist of an invasive intravitreal, intracameral, posterior juxtascleral, or retrobulbar injection of the medication into the eye, and the non-invasive (relative to surgery) approaches include application of high drug dosage through topical, oral, systemic, or sub-tenon administration [17].

Despite encouraging results presented in some preclinical models, clinical trials using these approaches have been less promising. The results vary from increased normal tissue toxicity or complete or partial lost of vision to only small increase in patients' survival rate. That is because either the approach is extremely harsh for the sensitive CNS microenvironment (ICV or intravitreal approach), or it is specific to a small group of drug molecules (molecular Trojan horse approach). Nevertheless, recent developments using physical stimuli have drawn lots of attention.

Table 1: Invasive brain drug delivery methods

Intranasal Drug Administration	Diffusion of small lipid-soluble molecules from the submucous spaces of the nose to the brain through the epithelial barrier [10].
Intracerebral Implants	Implantation of genetically engineered cells or biodegradable polymers in the brain. Minimal drug administration due to poor penetration (approximately 1 mm) into the tissue [18].
Convection-Enhanced diffusion	Effective for brain tumours yet extremely invasive neurosurgical-based technique involves the intracerebral infusion of fluid through the brain tissue [10].
Intracarotid arterial infusion	Solvents or agents such as vasoactive molecules, alkylating agents, cold saline, free fatty acids, and high dosage ethanol can presumably cause BBB disruption. They generally involve harsh applications [10].

Table 2: Non-localized minimally to non-invasive brain drug delivery methods

Lipidization	Addition of lipid groups to increase permeability
Nano-carriers	Employment of nano-sized particles to infiltrate large molecules through the BBB [19], [20].
Endogenous transports	Chemical modification of drugs to deceive the BBB, such as in Trojan horse technique [21].
Osmotic opening	Exposing of the BBB to a hyperosmolar solution causes the endothelial cells to shrink and place a reversible stress on the tight junctions by pulling them apart. Therefore, temporarily the BBB is considered "open" [22].

2.3 Physical stimuli for CNS drug delivery

Physical stimulation of the vessels, endothelial cells, and the tight junctions can indeed promote vascular leakage and may facilitate drug diffusion into the CNS.

2.3.1 High intensity focused ultrasound

High intensity focused ultrasound (HIFU) is among recent techniques that promise increase in BBB permeability as well as localized control [23]. This technique employs an acoustic energy to vibrate intravenously administered micro-metric lipid-encased perfluorocarbon gas microbubbles (MBs) near the target endothelium. The oscillating MBs create a mechanical stress on the endothelial tight junctions thus allowing therapeutics to enter the brain [24], [25]. Despite its enhanced synergistic effects, MBs have short half-lives in the vasculature and are quickly up-

taken by the reticuloendothelial system when circulating through the liver. Furthermore, oscillating MBs undergo a phenomenon that leads to formation of high-pressure shock waves as well as fast-moving liquid jets [26], which can seriously damage the cellular membrane near rigid surfaces in the brain. Also, the sound waves propagate non-linearly over a large region of biological structures before converging into a focal point, which may lead to undesirable side effects. While recent efforts claim to have increased efficacy by conjugating MBs with MNPs [27], HIFU offers low spatial and temporal resolution for drug delivery to the brain. This is mainly because the acoustic energy propagates non-linearly over a broad region of biological structures before converging into its relatively large focal point ($1 \times 1 \times 7$ mm^3 [23]). Similar to light waves, sound waves follow laws of reflection and refraction. Therefore, sudden variation in the acoustic impedance of the skull from that of the adjacent soft tissue can lead to reflection of the energy and thus promote intolerable change of temperature in the brain and on the surface of the skull [28].

2.3.2 Magnetic targeting

Magnetic targeting is another technique that over the years has drawn the attention of many researchers. In this technique drug molecules are loaded with MNPs and the complex is magnetically propelled to a target and then pulled across the CNS barrier using an external permanent magnet or an electro-magnet located near and above a biological target site. However, in a recent study [29], despite what the authors claim, the MNPs seem to injure the surface of the cellular membrane while being pulled across the barrier. Also, due to higher field intensity near the external magnet (higher gradient), targeting is mostly restricted to superficial areas near the skin. Furthermore, this technique lacks concurrent systematic navigational control when employed in the complex microvascular structures of the brain and may not be suitable for CNS drug delivery. Nevertheless, development of a complementary approach that employs the attractive magnetic targeting technique with imaging capabilities, transient opening effect on CNS barrier, and compatibility with CNS immune system is demonstrated to have merit.

2.3.3 Hyperthermia

In modern oncology, hyperthermia – otherwise known as elevation of body temperature – refers to heating of organs or tissues in various ways to temperatures between 40 °C and 45 °C, at

which point it causes moderate and reversible cellular inactivation [31]. This heat can preferentially lead to the death of cancer cells by enhancing cell sensitivity and vulnerability towards more established forms of cancer therapy, such as radiation and chemotherapy.

The effects of heat on CNS barrier and its microcirculation are but one example of the complex interaction between heat and the CNS circulation. Hyperthermia above 43 °C can cause vascular damage, increase in membrane permeability, and increase in cerebral blood flow. Subsequently, these in turn lead to cerebral ischemia, release of various neurochemicals, and increase in glutamate neurotoxicity [32]. The molecular mechanism of hyperthermia-induced CNS barrier leakage is not entirely understood; nevertheless, mild hyperthermia (below 40 °C) constitutes intense cellular stress and causes reversible disruption of the CNS barrier [33]. Studies suggest that the morphological changes of individual endothelial cells in the monolayer lining of the microvessels are necessary for the tight junctions between adjacent endothelial cells to loosen thereby allowing transport of large molecules through intercellular pathway [34]. During local and mild hyperthermia, systematic blood flow and movement of the interstitial fluid in the microenvironment, prevents healthy cells from overheating [35]. In these conditions, hyperthermia redirects protein synthesis in the cells to produce heat-shock proteins, increases the membrane fluidity, and changes the vesicular and tubular components of microvascular endothelial cells [36]. An interesting observation by scientists is that cells undergo a conditioning phenomenon that renders them capable of adapting to heat in order to survive [37]. Heat shock or stress conditions experienced by cells and tissues alters cell structure and function in a homeoviscotic manner and render them more resistant to further stress. Therefore, cells can build tolerance to the damaging effects of temperature if they are gradually and repeatedly heated [36], [38]. After cessation of mild hyperthermia, tight junctions commence to recover [39] and their recovery rate depends on the amount of heat and exposure time.

2.4 Hyperthermia of MNPs

While conventional hyperthermia methods such as whole body hyperthermia [40], high intensity focused ultrasound [41], radio frequency [42], and microwave [33], [43] have been applied to allow certain molecules to cross the CNS barrier, they do not have spatial precision and they are not effective in deep structures of the brain. In addition, these techniques adversely affect the cerebrovascular unit. In other words, these remedies modify the barrier functionality as well as its

surrounding biological entities such as neurons, astrocytes and glial cells. This widespread heating can induce many undesirable acute side effects.

To address the above-mentioned setbacks, the proposed alternative method is based on hyperthermia of MNPs by an external alternating magnetic field. In this configuration, an alternating magnetic field remotely excites the MNPs at a desired target vasculature in the CNS. The generated heat from the MNPs is then dissipated directly to the surface of the endothelium resulting in brief barrier leakage.

2.4.1 Advantages of using MNPs for hyperthermia

In order to make CNS drug targeting a clinically viable technique, one has to propel drug molecules towards the target and control their motion via an imaging modality. This is indeed the basic idea behind the magnetic resonance navigation (MRN) project [30]. In this approach, micro-carriers composed of drug molecules and aggregates of MNPs are used to navigate inside small capillaries. The MRN provides physicians with a platform that allows targeting and delivery of medications to any specific location in the human body. In this design, MRN relies on a clinical magnetic resonance imaging (MRI) scanner to navigate the micro-carriers along a pre-determined suitable vascular route on their journey towards the target. The MNPs function as MRI contrast agents and provide the capability to assess the targeting efficacy through imaging sequences. Biocompatible iron-oxide superparamagnetic nanoparticles used in MRN have already been proven effective to orchestrate monitoring and steering in the MRI to deliver therapeutic agents through a suitable vascular route. Hyperthermia of MNPs therefore, complements the already successful MRN system for the purpose of drug delivery to CNS. In addition, hyperthermia operates at relatively low focal temperatures (maximum of 39 °C) and the heat is dissipated directly and uniquely to the surface of the endothelial cells without compromising the neurovascular unit (neurons and glia). Moreover, blood flow and movement of the interstitial fluid in the brain microenvironment will further help prevent other sensitive structures in the CNS from overheating [14]. The low focal temperatures also help accelerate the recovery process and the return to the status quo for the tight junctions. Furthermore, the radiofrequency magnetic field allows this technique to be effective in deep biological structures of the CNS, especially in the brain. Last but not least, specific surface coating of the MNPs can increase particle affinity to the endothelium and thus enhance thermal delivery and efficiency.

For instance, transferrin, a single-chain of glycoproteins, has receptors that are unregulated on both the endothelium [44], and on the surface of many cancer types, including glioblastoma and retinoblastoma. Therefore, transferrin conjugated MNPs (Tf-MNPs) are excellent candidates to target the CNS barrier [15].

2.5 Physics of hyperthermia of MNPs

The thermal energy generated by magnetic materials inside of an alternating magnetic field is mainly caused by three major mechanisms; hysteresis loss, Néel and Brownian relaxations. Particle size, shape, composition, concentration and viscosity of the suspension medium as well as magnitude and frequency of the applied alternating magnetic field determine the relative strength of each of these mechanisms. In this section, details of scenes behind magnetic heating (hyperthermia) are explained.

2.5.1 Magnetic Domains

In order to minimize magnetostatic energy of the material, large magnetic materials consist of several domains. The magnetostatic energy is the energy of the magnet in its own field. As shown in Figure 2.2 [45], by splitting the crystal into several domains, the spatial extent of the **H** field decreases. This is because as the number of domains increase, the north and the south poles become closer and therefore it reduces magnetostatic energy of the material.
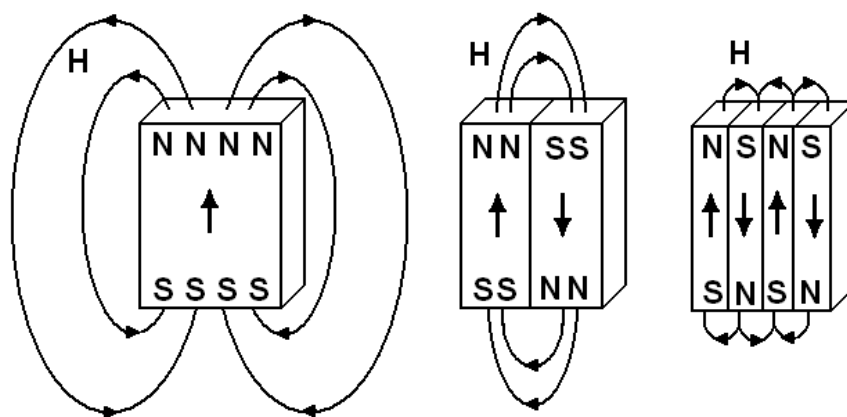
Figure 2.2: Magnetostatic energy reduces as crystal is split into domains

The boundary separating the two neighbouring domains is called a domain wall. Each domain contains large numbers of atomic magnetic moments, *m* created by microscopic current related to the spin of the electrons. Indeed, all materials are classified by the orientation of their magnetic moments and form various types of magnetism mainly known as ferromagnetism, ferrimagnetism, antiferromagnetism, paramagnetism and diamagnetism. The complete theory of magnetism is well beyond the scope of this introduction. However, Figure 2.3 [45] illustrates the orientation of the magnetic moments for these types of magnetism.

Magnetic moments of ferri-, ferro- and antiferromagnetic materials are aligned with each other below a critical temperature – the Curie temperature – to reduce the exchange energy of the material. The exchange energy is caused by the interactions among internal magnetic moments. According to the Weiss domain theory [47], the direction of the aligned moments varies from domain to domain, and in the absence of an external magnetic field this direction is aligned along magnetic crystallographic axes called 'easy axes'. In fact, domain walls consist of smooth gradual rotation of the direction of the *m* vectors within the crystal shown in Figure 2.4 [45].
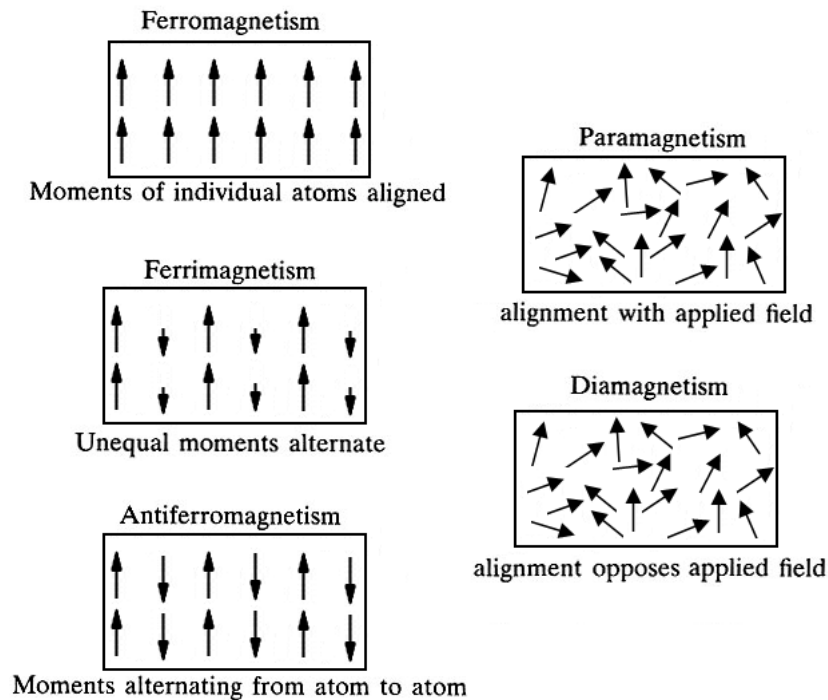
Figure 2.3: Different types of magnetism [45]

The spin-orbit coupling, meaning interaction between spin and the orbital motion of each electron, exhibits a resistive force against any attempt by an external magnetic field to rotate the spin axis. The energy required to overcome the spin-orbit coupling that keeps particles magnetized in a specific direction is called anisotropy energy, $E = KV$, where K is the effective anisotropy constant and V is the volume of the magnetic core [45], [48]. The anisotropy constant is a sum of several terms such as magnetocrystalline, shape and surface anisotropy as well as dipole-dipole interaction between the crystals [49]. Here, it is assumed that the MNPs have spherical shapes and are mono-dispersed in solvent with low volume fractions. Therefore, magnetocrystalline and surface anisotropy contribute the most to the effective anisotropy constant of MNPs.
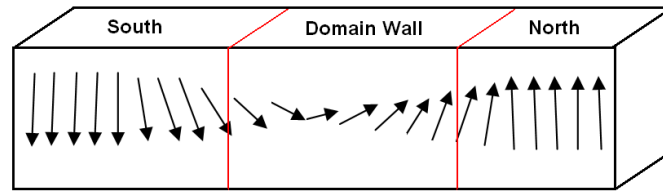
Figure 2.4: Presentation of domain wall [45]

As the external magnetic field strength increases, the net *m* vectors of the domains of a ferri- and ferromagnetic material become more aligned with the external magnetic field direction to minimize the crystal potential energy and cause displacement of the domain walls. Figure 2.5 [45] shows that as the external field strength becomes larger, the magnetic moments opposing it become smaller. If the external field is high enough, it can align all *m* vectors to the magnetic field direction and the material can act as a single domain particle with a unidirectional magnetic moments.
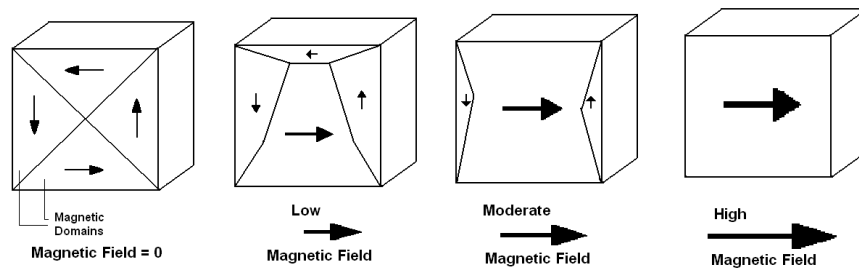
Figure 2.5: Multi-domain material inside applied external magnetic field [45]

In this investigation, ferrimagnetic iron oxide (magnetite) nanoparticles were chosen. As shown in Figure 2.3, these nanoparticles display lower magnetic response compare to ferromagnetic materials. This is because a ferrimagnetic material consist of *m* vectors that are not all aligned in one direction, therefore, the net *m* vector is smaller than that of a ferromagnetic material where the *m* vectors are all aligned in one direction. However, in addition to magnetite biocompatibility and low toxicity advantages, these particles are less sensitive to oxidation than ferromagnetic materials and therefore maintain stable magnetic behaviour [46] in rich oxygen environments such as in a human body.

2.5.2 Hysteresis

The energy from exposure to moderate external field **H** (Figure 2.6 point 1) [45] leads magnetic moments to overcome the anisotropy energy. This results in an irreversible sudden rotation of the magnetic moments into a new set of magnetic crystallographic axes. These axes are nearest to the external field direction. The directions of the moments within domain walls are indeed a balance between exchange and anisotropy energies. Therefore, a change in the external field energy can alter this balance and cause moments to rotate. Further increase in field amplitude leads to saturation of magnetization M_S of the magnetic moments (Figure 2.6 point 2) and a reversible and gradual alignment with the external field direction and hence creation of a sample that acts as a single domain [47]. The M_S value for a bulk matter is different for nanoparticles of the same material. For example, experimental values for M_S of magnetite nanoparticles are between 30 – 60 emu g^{-1}, whereas this value for the bulk magnetite is reported to be as high as 92 emu g^{-1} [46]. The reason for such difference is not yet entirely clear and still under investigation. By reducing the applied magnetic field to zero, magnetization **M** of the domains decreases gradually to remanent magnetization – M_R (Figure 2.6 point 3). The magnetization can be reduced to zero by applying a magnetic field in the opposite direction and a magnitude equal to the coercive field H_C (Figure 2.6 point 4). At this point domains are demagnetized completely, but they can gradually begin to realign in the opposite direction if the external field is increased in the negative direction and reaches M_S (Figure 2.6 point 5). Once again, by reducing the external field to strength zero, magnetic moments reach M_R in the negative **M** axis (Figure 2.6 point 6). An applied magnetic field magnitude equal to coercive field H_C in the positive direction will bring magnetization to zero and further increase of the field amplitude in this direction will trace the curve back to

positive M_S (Figure 2.6 point 2). As shown in Figure 2.6, the magnetization curves for increasing and decreasing magnetic field amplitudes do not coincide and therefore the material demonstrates "hysteresis behaviour" – hysteresis is a Greek word for 'a coming late' – and hysteresis losses are expressed in the form of heat dissipated to the surrounding medium.
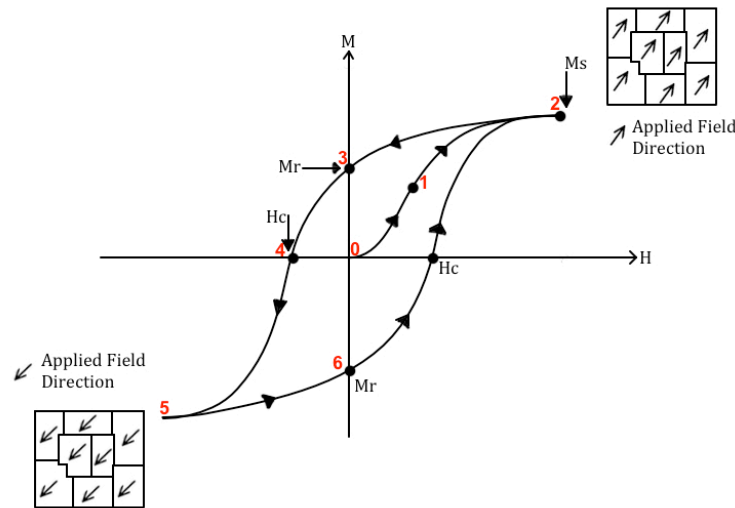
Figure 2.6: Hysteresis curve of a multi-domain particle [45]

In the case of fine ferri- and ferromagnetic single domain particles, such as iron oxide and cobalt respectively, thermal agitations are ignored when the difference between the maximum and the minimum energy per unit volume, set by the anisotropy energy of the particle, is larger than its thermal energy kT, where k is Boltzmann constant. Stoner-Wohlfarth's calculations [50] demonstrate a narrow hysteresis curve for these single domain magnetic particles. When an external magnetic field is applied to magnetize and demagnetize such particles, energy is released in the form of heat. As in multi-domain particles, when the external magnetic field amplitude is larger than the anisotropy field, the anisotropy energy barrier is overcome and the magnetic moments will rotate onto the anisotropy axis closest to the external magnetic field direction. Further increase in the external field will lead to gradual alignment of the net magnetic moment with the external magnetic field direction until saturation. Figure 2.7A demonstrates this phenomenon. In this figure, red arrows represent the magnetic moments of the particle and green arrows represent the dominant 'easy axes'. When external field **H** is applied, the magnetic moment follows the field direction. Once the external magnetic field is removed, the magnetic

moment takes a certain time to rotate back to its original lower energy 'easy axis. Release of heat is therefore due to the fact that magnetisation here lags the applied external field.
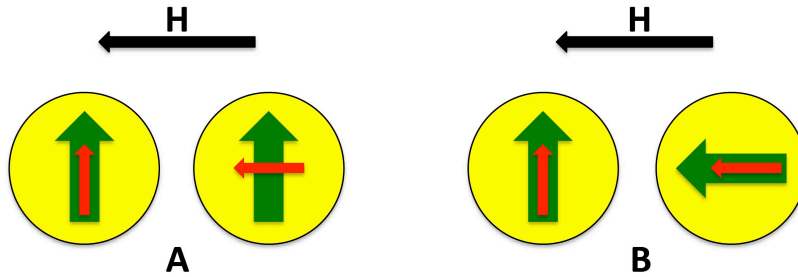
Figure 2.7: Relaxation Mechanisms

Dashed lines represent the magnetic moments of the particle and solid lines represent the dominant 'easy axes'

2.5.3 Superparamagnetic Nanoparticles

In smaller single domain magnetic particles, called superparamagnetic nanoparticles – less than 20 nm in diameter for Iron Oxide Fe_3O_4 (Magnetite) MNPs [51] – the difference between the magnetic moment maximum and minimum potential energy per unit volume of the particle is much smaller than its thermal energy kT. The orientation of the magnetic moments of these particles therefore, continuously changes due to thermal agitation [52]. In other words, thermal energy becomes significant enough to cause magnetic moments to randomly fluctuate in the absence of the energy from an external magnetic field. Due to this behaviour, as shown in Figure 2.8 measured for iron oxide nanoparticles, these particles seem to lack hysteresis losses. However coercive fields H_C do not rest at zero. Therefore, an extremely narrow hysteresis loss is formed which contributes into release of heat within superparamagnetic nanoparticles.
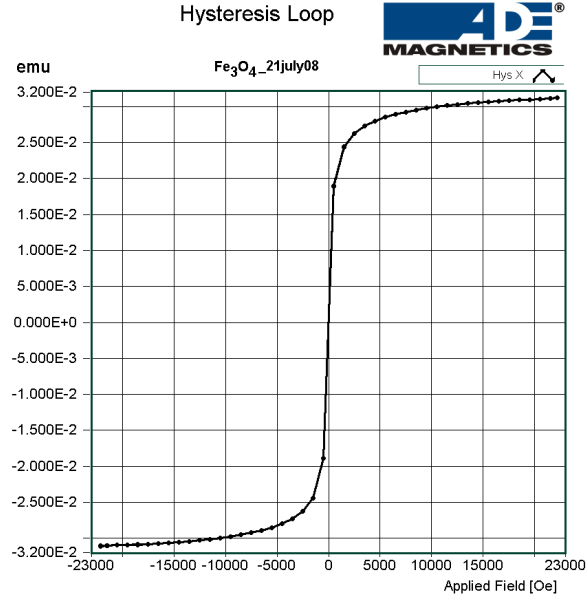
Figure 2.8: Hysteresis curve of an iron oxide superparamagnetic particle

2.5.4 Relaxation Mechanisms

By applying a moderate external magnetic field to superparamagnetic nanoparticles, the energy from the field drives the magnetic moments to rotate and aligns them with the magnetic field direction by overcoming the thermal energy barrier. Once the external magnetic field is removed, magnetic moments do not relax immediately but rather take some time to randomize their orientations. In fact, according to Néel relaxation mechanism, in superparamagnetic particles the alignments and relaxations are responsible for the generation of heat. According to Néel-Arrhenius equation [52], the time τ_N for the magnetic moments to relax and rotate back to their thermal equilibrium orientation is given by

$$\tau_N = \tau_0 \exp\left(\frac{KV}{kT}\right) \tag{1}$$

where K is the effective anisotropy constant, V is the volume of the magnetic core, kT is the thermal energy and τ_0 is a constant called 'attempt time' typically of a value equal to about 10^{-9} to 10^{-11} seconds and is slightly field dependent, however this dependency is usually ignored [53].

The third mechanism that may contribute to generation of heat within MNPs is Brownian relaxation. This type of relaxation mechanism causes both multi-domain and single domain

particles to heat up. In this case, shown in Figure 2.7B, the energy barrier for reorientation of a particle is given by rotational friction due to the rotation of the entire magnetic particle caused by the external magnetic field torque on the magnetic moment of the particle. Here, by applying the external magnetic field **H** the particle itself is able to turn towards the field direction. Brownian relaxation time τ_B, is defined by the rotational mobility of the colloidal magnetic particles and given by [54]

$$\tau_B = \frac{3\eta V_H}{kT} \tag{2}$$

where η is the dynamic viscosity of the medium in which the particles are suspended and V_H is the hydrodynamic particle volume. This volume, which is the volume of the magnetic core of the particle plus the coating shell around it, represents how the medium perceives the particle. The Brownian relaxation time is related to the applied magnetic field through the complex magnetic susceptibility. The relationship between magnetization **M** and the applied magnetic field **H** is expressed below by a parameter called magnetic susceptibility χ

$$\mathbf{M} = \chi \, \mathbf{H} \tag{3}$$

This parameter explains how magnetization varies with respect to the applied magnetic field. As described later, susceptibility consists of a complex (imaginary) and a real component. The Brownian relaxation time is accessible from the frequency (f) dependent complex susceptibility through the following equation [54]:

$$\chi(f) = \frac{\chi_0}{1 - i\,2\pi\,f\,\tau_B} \tag{4}$$

where χ_0 is the DC susceptibility.

For MNPs uniformly suspended in a liquid medium, relaxation times Néel τ_N and Brownian τ_B take place in parallel [55]. Therefore the effective relaxation time τ_{eff} or τ is given by

$$\frac{1}{\tau_{\text{eff}}} = \frac{1}{\tau_N} + \frac{1}{\tau_B} \tag{5}$$

By simulating and plotting relaxation times versus particle size in Figure 2.9, (Matlab® code is given in Appendix A.1) for any given radius, it is clear that the shorter time constant dominates the effective relaxation time. It is worth mentioning that in highly viscous media, such as thick gel or tissue, the inverse of Brownian relaxation becomes very small and therefore, the effective time becomes dependent on Néel relaxation exclusively.

Relaxation times are temperature dependent. However for mild hyperthermia at near 42 ºC, relaxation time constants does not alter by much, thus in this investigation the effect of small temperature elevations on time constants are considered negligible.
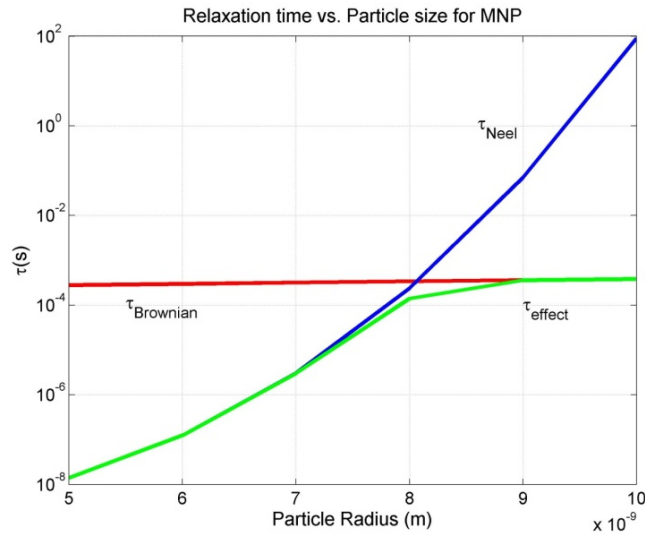
Figure 2.9: Relaxation time vs. Particle size for MNPs

2.5.5 Specific Absorption Rate (SAR) and Specific Loss Power (SLP)

In hyperthermia, Specific Absorption Rate (SAR) is a measurement of the magnetic power absorbed per unit mass of the magnetic material (W g^{-1}). SAR is proportional to the time rate of change of the temperature of the magnetic material and given by the following formula [56]:

$$SAR = \frac{c \, V_s}{m} \frac{dT}{dt} \qquad\qquad (6)$$

where c is the specific heat capacity of the sample (4185 J l^{-1} K^{-1} for water), m is the mass of the magnetic particles, V_s is the total volume and $\frac{dT}{dt}$ expressed in ºK s^{-1} is the temperature increment

which is experimentally derived from the linear regression of the initial data points seen in Figure 2.10.
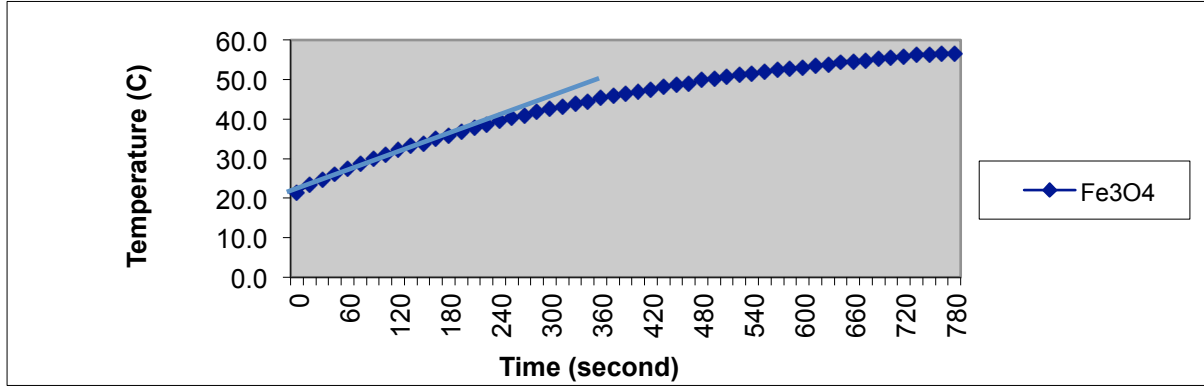
Figure 2.10: Temperature vs. time for superparamagnetic magnetite nanoparticles

Specific loss power SLP is a measurement of the magnetic power loss per unit volume of the magnetic material (W m^{-3}). The loss power is transformed into heat and dissipated to the surrounding medium. SLP is obtained by multiplying SAR by the density ρ (g cm^{-3}) of the magnetic material ($SLP = c \frac{dT}{dt}$).

According to the first law of thermodynamics, change in the internal energy dU of an adiabatic process ($\delta Q = 0$) is equal to the differential of magnetic work energy W on the system

$$dU = \delta Q + \delta W \qquad (7)$$

$$dU = \delta W = \mathbf{H} . d\mathbf{B} \qquad (8)$$

Where W is the magnetic work done per unit volume of the magnetic material [55], $\mathbf{H}$ is the external magnetic field strength and $\mathbf{B}$ is the induction flux.

As seen in Figure 2.11 [57], Equation (8) suggests that the change of $\mathbf{B}$ also lags behind that of $\mathbf{H}$ and just as seen in 2.5.2, this lag can cause the magnetic material to exhibit hysteresis.
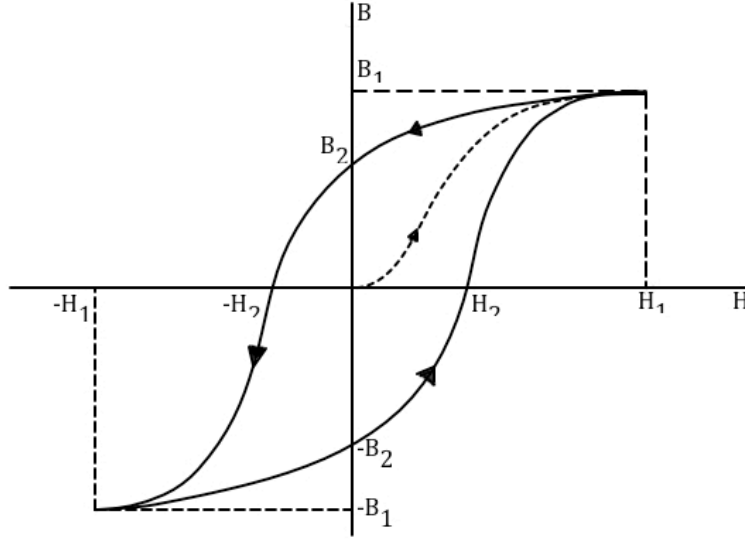
Figure 2.11: Hysteresis of a magnetic material in *B* and *H* axes.

Integration by parts of each segment of the hysteresis curve in respect to dW leads to

$$W = \int_{B_1}^{B_2} \mathbf{H}.d\mathbf{B} \ dW + \int_{B_2}^{-B_1} \mathbf{H}.d\mathbf{B} \ dW + \int_{-B_1}^{-B_2} \mathbf{H}.d\mathbf{B} \ dW + \int_{-B_2}^{B_1} \mathbf{H}.d\mathbf{B} \ dW$$

$$= \left(\mathbf{H}.d\mathbf{B} \ |_{B_1}^{B_2} - \int_{H_1}^{H_2} \mathbf{B}.\frac{d\mathbf{H}}{dW}dW \right) + \left(\mathbf{H}.d\mathbf{B} \ |_{B_2}^{-B_1} - \int_{H_2}^{-H_1} \mathbf{B}.\frac{d\mathbf{H}}{dW}dW \right) \quad (9)$$

$$+ \left(\mathbf{H}.d\mathbf{B} \ |_{-B_1}^{-B_2} - \int_{-H_1}^{-H_2} \mathbf{B}.\frac{d\mathbf{H}}{dW}dW \right) + \left(\mathbf{H}.d\mathbf{B} \ |_{-B_2}^{B_1} - \int_{-H_2}^{H_1} \mathbf{B}.\frac{d\mathbf{H}}{dW}dW \right)$$

$$W = -\oint \mathbf{B}.d\mathbf{H} \quad (10)$$

Due to co-linearity of the fields, the angle between **B** and **H** reduces to zero and therefore the dot product vanishes and *B* and *H* become magnitudes [55].

$$W = -\oint B \ dH \quad (11)$$

B in Tesla is given by [45]

$$B = \mu_0(H + M) \tag{12}$$

where M is the magnetization of the material (A m^{-1}) and μ_0 is the permeability of free space ($4\pi \times 10^{-7}$ T m A^{-1}). Substituting Equation (12) into Equation (11), magnetic work can be expressed by

$$W = -\mu_0 \oint (H + M)\, dH \tag{13}$$

When magnetization lags the field, the integration yields a positive result indicating conversion of magnetic work to internal energy [55], therefore:

$$\Delta U = -\mu_0 \oint M\, dH \tag{14}$$

Therefore, the greater the closed area within the hysteresis loop, the greater will be the internal energy.

As described in Section 2.5.4, heat is associated with the energy change through Néel relaxation due to magnetization and demagnetization of the superparamagnetic nanoparticles and rotation of the magnetic moments in an alternating magnetic field. Therefore, Néel relaxation can be seen as a form of hysteresis loss for superparamagnetic nanoparticles. For an applied time varying external magnetic field

$$H(t) = Re\left[H_0 e^{i\omega t}\right] = H_0 \cos(\omega t) \tag{15}$$

And,

$$\frac{dH}{dt} = -H_0 \omega \sin(\omega t) \tag{16}$$

Susceptibility on the other hand, consists of both real (Equation 18a) and imaginary (Equation 18b) components and are given by [55]

$$\chi = \chi' + i\chi'' = \frac{\chi_0}{1 + i\omega\tau} \tag{17}$$

$$\chi' = \frac{\chi_0}{1 + (\omega\tau)^2} \tag{18a}$$

$$\chi'' = \frac{i\,\omega\tau}{1 + (\omega\tau)^2}\chi_0 \tag{18b}$$

which is dependent on DC susceptibility χ_0, angular frequency $\omega = 2\pi f$ and relaxation time τ.

Magnetization as a function of time is therefore given in the following form:

$$M(t) = Re[\chi\,H_0 e^{i\omega t}] = H_0(\chi'\cos(\omega t) + \chi''\sin(\omega t)) \tag{19}$$

Substituting Equation (16) and Equation (19) into Equation (14), the internal energy becomes

$$\Delta U = -\mu_0 \oint H_0(\chi'\cos(\omega t) + \chi''\sin(\omega t))\,(-H_0\omega\sin(\omega t))\,dt$$

$$= \mu_0 H_0^2 \omega \left[\oint \chi'\cos(\omega t)\sin(\omega t) + \oint \chi''\sin^2(\omega t)\,dt\right] \tag{20}$$

Integrating over one period, $1/f$, where f is the frequency and equal to $\omega/2\pi$, the Equation (20) leads to

$$\Delta U = \mu_0 H_0^2 \omega \left[\chi'\frac{\sin^2(\omega t)}{2\omega}\Big|_0^{2\pi/\omega} + \chi'' \oint \sin^2(\omega t)\,dt\right]$$

$$= \mu_0 H_0^2 \omega \chi'' \int_0^{2\pi/\omega} \sin^2(\omega t)\,dt \tag{21}$$

where only the complex susceptibility component survives the integration.

The specific loss power SLP, is equal to the internal energy multiplied by its frequency.

$$\text{SLP} = \frac{SAR}{\rho} = \Delta U\,f = \mu_0 f H_0^2 \omega \chi'' \int_0^{2\pi/\omega} \sin^2(\omega t)\,dt \tag{22}$$

where ρ is the magnetic particle density and f is the frequency of the external magnetic field. Solving for the above equation

$$\text{SLP} = \frac{SAR}{\rho} = \mu_0 \, f \, H_0^2 \, \pi \, \chi'' \tag{23}$$

Hysteresis loop for ferromagnetic materials differs from a DC magnetic field to an alternating magnetic field. For constant magnetic field amplitude, as the frequency increases, the area of the hysteresis loop increases at first, and eventually decreases [58]. However to avoid complexity, here this factor has not been taken into consideration.

Magnetic nanoparticles prepared with surface stabilizers form magnetic fluids, also known as ferrofluids, are suspended uniformly in a carrier liquid. These materials are single domain and are superparamagnetic. For such particles, relaxation mechanisms are dominant. From Equations (23) and (18b), SAR is expressed as [55]

$$\text{SAR} = \mu_0 \, f \, H_0^2 \, \pi \, \chi_0 \frac{2 \, \pi \, f \, \tau_{\text{eff}}}{1 + (2 \, \pi \, f \, \tau_{\text{eff}})^2} \frac{1}{\rho} \tag{24}$$

Figure 2.12 (Matlab$^{\circledR}$ code is given in Appendix A.2) plots a simulation of the real and the imaginary components of the susceptibility as given in Equation (17). These components meet at the peak value of χ''. In fact, as seen in Equation (21), the imaginary component of susceptibility is due to the phase difference between the applied magnetic field and the corresponding magnetization and therefore, it is responsible for generation of heat. Moreover, χ'' reaches its peak value when $\omega \tau = 1$. In the following sections this will help optimize MNPs core diameter for hyperthermia.
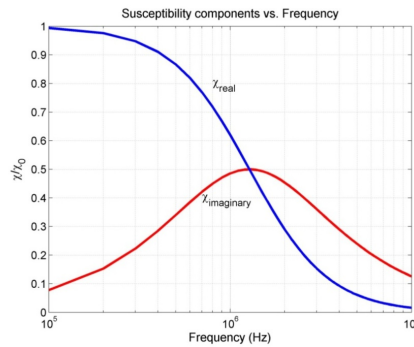
Figure 2.12: Susceptibility components vs. Frequency

2.6 Magnetic Properties Suitable For Hyperthermia

Magnetic properties suitable for hyperthermia are not only governed by the magnetic parameters of the MNPs but also by the physiological limitations that are set to protect living organisms against high magnetic fields. By optimising these properties, maximum SAR and thermal effect can be reached and therefore, fewer MNPs are required at the target area. In this section some of the magnetic parameters and limitations are discussed.

2.6.1 MNPs Physical Parameters

2.6.1.1 Size

The size of the MNPs influences the value of SAR and therefore the thermal effect. As explained before, an area within a wide hysteresis loop leads to dissipation of more heat than does a narrow hysteresis loop. Assuming constant magnetization saturation M_S, coercive field H_C defines width of the hysteresis loop. There is a relationship between particle core size and the coercive field. As shown in Figure 2.13 [45], the H_C is at its largest value for particles that are at the border of being single and multi-domain. Superparamagnetic nanoparticles show no hysteresis and therefore it is not surprising to see that they do not have any coercive field.
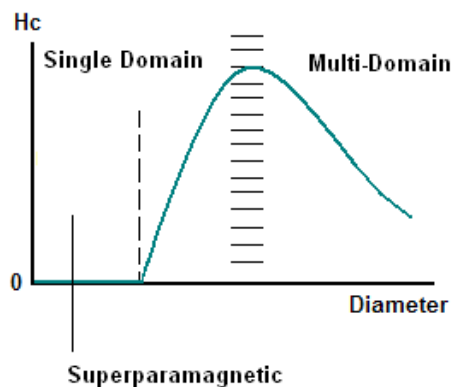
Figure 2.13: Coercive field vs. particle diameter [45]

Figure above suggests that particles resting on the border between single and multi-domain exhibit the highest value of SAR and thus are the best choices for hyperthermia. In a study, Zhang *et al*. [59] showed that due to technical and biocompatibility issues, the applied alternating

magnetic field is often much lower in amplitude than the field required to saturate all magnetic moments of MNPs. Conceptually, to benefit from heat generation by a complete hysteresis loop, particles have to magnetically saturate to extremely high fields on the order of a few thousand Oersted. Such fields may cause unwanted tissue heating, stimulation of peripheral and skeletal muscles and irreversible biological effects such as cardiac fibrillation [60]. Therefore, adequate magnetic field and frequency necessary to make use of the entire hysteresis loop would be too high to consider for hyperthermia. In addition, because an ensemble of multi-domain MNPs align randomly with the magnetic field, practically only 25% of the ideal maximum theoretical power may be dissipated as heat [61].

According to Okawa *et al.* [62], under a moderate and physiologically tolerable alternating magnetic field, the single domain MNPs of 18 nm in diameter reached target temperature of 43 ºC quicker than superparamagnetic and multi-domain MNPs. This claim is also in close agreement with the findings of Johannsen *et al.* [63] in which magnetite nanoparticles of 15 nm in diameter were used to elevate tumour temperature *in vivo* tests.

As mentioned at the end of Section 2.5.5, the imaginary component of susceptibility is responsible for the heating of MNPs inside an alternating magnetic field. It was also shown that this component is at its highest value when $\omega\tau = 1$ where ω is the angular frequency and τ is the effective relaxation time. In highly viscous media such as tissue, the effect of the Brownian relaxation time on the effective relaxation time τ is negligible and Néel relaxation time τ_N is the dominant factor [64]. Using Equation (24), Figure 2.14 (Matlab$^{®}$ code is given in Appendix A.3) simulates how SAR due to Néel relaxation behaves as size of the iron oxide MNPs varies. Frequencies of 20 kHz, 200 kHz and 2 MHz were randomly chosen to display the effect of frequency on SAR.
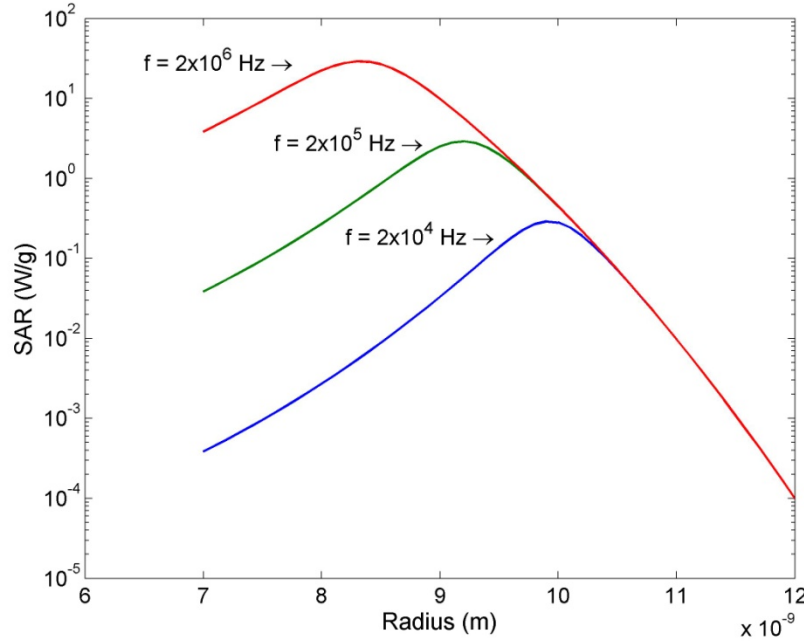
Figure 2.14: Power loss due to Néel relaxation vs. radius of MNPs

2.6.1.2   Concentration of MNPs

In steady state temperature difference ΔT is given by [65]

$$\Delta T = \text{SAR}\, \frac{c\,R^2}{3\lambda} \tag{2.25}$$

where c is the concentration of the MNPs (mass of the particles per tissue volume) and λ represents the heat conductivity of a tissue volume with a radius R. From the above equation it is evident that higher concentration of MNPs in the tissue leads to higher ΔT.

Earlier in Section 2.5.1 it was mentioned that one of the factors affecting the effective anisotropy constant K is the dipolar magnetic interaction generated by each particle in the external magnetic field on the neighbouring particles. Therefore, when the number of MNPs is altered, there will be a change in the dipolar interaction of MNPs. As a result, change in the concentration of MNPs will lead to a small change of the K value [66]. This alteration however, is considered insignificant in this investigation.

2.6.2 Limitations to Amplitude and Frequency of the alternating magnetic field

Reversible hyperthermic disruption of the CNS barrier requires a precise delivery of well-controlled thermal dose into a complex biological system of the brain that is equipped with its own thermoregulatory system. There are guidelines limiting the alternating magnetic field parameters (frequency and amplitude) to prevent deleterious physiological responses. These responses are stimulations of peripheral and skeletal muscles, possible cardiac stimulation, arrhythmia and non-specific inductive heating of tissue. The guidelines are obtained from scientific observations and epidemiological studies.

For biomedical purposes, the frequency of the alternating magnetic field has to be higher than 50 kHz to avoid neuromuscular electro-stimulation and lower than 10 MHz for appropriate penetration [67]. Available experimental data shows that the resting human body temperature can be elevated up to 1 °C if it is exposed to an electromagnetic field that produces a whole-body SAR of between 1 and 4 W kg^{-1} [60]. Eddy current loss produced by closed currents induced by alternating magnetic flux in a conductive tissue of sufficient area are responsible for this type of heating [68]. Harmful levels of tissue heating can be produced by exposure of the tissue to fields at higher SAR values. Atkinson *et al.* [69] therefore, established an upper limit of 4.85 x 10^8 A m^{-1} s^{-1} for the product of field amplitude (H$_0$) and frequency (f) for a single turn induction coil around the thorax of a normal size patient. For such body exposure, a tissue load threshold of 25 mW ml^{-1} was recommended by Jordan *et al.* [68]. Power density absorbed by the tissue is given by

$$P_{tissue} = \pi^2 \frac{\mu^2 \, \mu_0^2 \, \sigma_T}{2} f^2 r^2 H_0^2 \qquad (\text{W m}^{-3}) \qquad (26)$$

where μ is the permeability and μ$_0$ is the permeability of free space, σT is the conductivity of the tissue, f stands for frequency, H$_0$ is the external field strength and r is the distance from the central axis of the body. Using the above equation and the upper limit to the product of the field amplitude and frequency, the following graph (Figure 2.15) is simulated and plotted (Matlab$^{®}$ code is given in Appendix A.4).
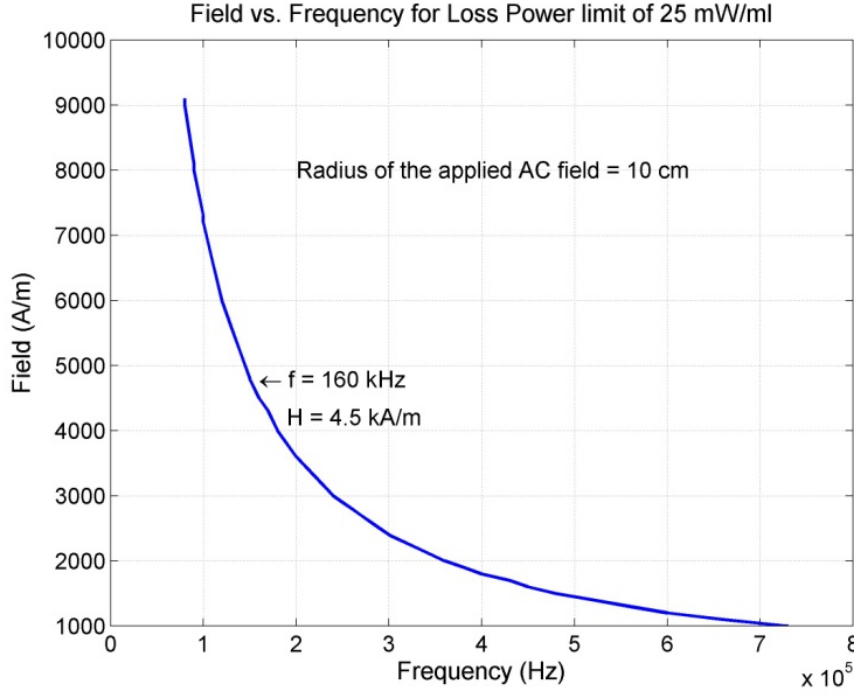
Figure 2.15: Biological limitation to field and frequency

In the above graph, the curve represents the upper limit for H_0 and f that can be used for patients with a body cross section of 10 centimetres in radius at tissue load limit of 25 mW ml^{-1}. This simulation also took into account values for biological tissue conductivity ranging from 0.0144 S m^{-1} to 0.68 S m^{-1} as tabulated in [70] for frequencies in the range of 100 kHz to 1 MHz. Since eddy current power density is proportional to the square of the diameter of the induced current loops, the proposed upper limit can be accordingly larger for smaller body regions under alternating magnetic field exposure. For example, a higher limit of $H_0 \times f = 4 \times 10^9$ A m^{-1} s^{-1} has been suggested for treatments of the breast cancer [71].

When an electromagnetic wave passes through the human body, as it heats the tissue it also declines in intensity. This is given by

$$I = I_0 \exp{(-2 \propto_E x)} \qquad (\text{W m}^{-2}) \qquad (2.27)$$

$I_0 < 100$ (W m^{-2}) maximum safe incident intensity $\qquad \propto_E = \propto_e n_E^{1/2}$

where I is the power per unit area transmitted through the tissue, x is the penetration depth of the tissue, $\propto_E$ is the total attenuation factor including scattering and absorption. n_E is the incident frequency and $\propto_e$ averages $\sim 5 \times 10^{-3}$ sec$^{1/2}$m^{-1} for soft tissue [72]. According to Equation 23, at 1000 MHz (microwave) more than 90% of power is lost in approximately 15 mm depth of the soft tissue; at 30 GHz incident power has lost 99% of its energy in less than 10 μm depth in the tissue. On the other hand, 67% of the energy is passed through a thickness of 10 cm tissue un-scattered and un-absorbed at 160 kHz. This suggests a suitable frequency range (~100 kHz) for proper penetration of the alternating magnetic field and excitation of the MNPs at a deep target area. To simplify calculations, here the biological load is assumed to be isotropic and homogeneous and it's cross section exhibits cylindrical symmetry to the induction coil. Also, the magnetic field within the coil and tissue load is assumed to be uniform and field penetration into the dielectric material is complete. Moreover, the tissue under study is far away from any metalic implants that could affect the field in any way. Last but not least, it is assumed that there is no axial electric field within the coil.

Therefore, for proper penetration and efficient hyperthermic disruption of the CNS barrier by MNPs without harmful heating of the neural tissue caused by Eddie current losses, the alternating magnetic field amplifier is set to generate an amplitude of 7.6 kA m^{-1} at 150 kHz which falls in the alternating magnetic field exposure limit and allows for a penetration of up to 70% of the energy through a 10 cm thick tissue un-scattered and un-absorbed.

CHAPTER 3   PROJECT RATIONALE

Progress in pharmaceutical research for drug delivery to the CNS is limited by its pharmacokinetics through a physiological barrier. Successful transient opening of this barrier for diffusion of therapeutics into the neural tissue could strongly support the feasibility of this treatment in a clinical setting. Therefore, the objective is to develop a localized, and transient technique to interrupt barrier functionality without activating its immune system. This technique will complement our MRN system for targeted delivery of therapeutic agents to the CNS. To realize this objective, the work was divided into 3 phases. In phase 1, an external heating apparatus was used to apply regional heat on the skull of an anaesthetized mouse (Chapter 4 – Article 1). The effect of heat on the permeability of the BBB was assessed using histological observation and tissue staining of Evans blue (a large fluorescent dye molecule). Results indicated a direct correlation between hyperthermia and BBB leakage as well as its recovery from thermal damage.

In phase 2, hyperthermic opening of the BBB with MNPs in a rat model was investigated (Chapter 5 – Article 2). Extravasation of the Evans blue clearly supports the hypothesis. In this investigation, analysis of immunoreactivity indicated that the proposed technique is not associated with any inflammation.

In phase 3 (**Error! Reference source not found.**), sodium fluorescein, a small fluorescent dye, and Evans blue dye were used to examine the integrity of the retinal tissue (BRB) after hyperthermia. In this part of the investigation, transferrin coated MNPs were used to enhance particle adherence on the surface of the endothelium during hyperthermia. Results indicate that, similar to BBB, application of mild hyperthermia by MNPs leads to transient leakage of the retinal barrier.

Therefore, it is strongly believed that the aforementioned approach could potentially increase expectation for drug delivery to the CNS and may profoundly impact those affected by CNS disorders and their quality of life.

CHAPTER 4   ARTICLE 1 - TOWARDS MR-NAVIGABLE NANOROBOTIC CARRIERS FOR DRUG DELIVERY INTO THE BRAIN

Seyed Nasrollah Tabatabaei, Sonia Duchemin, Helene Girouard, and Sylvain Martel

4.1 Abstract

Magnetic Resonance Navigation (MRN) relies on Magnetic Nanoparticles (MNPs) embedded in microcarriers or microrobots to allow the induction of a directional propelling force by 3-D magnetic gradients. These magnetic gradients are superposed on a sufficiently high homogeneous magnetic field (e.g. the Bo field of an MR scanner) to achieve maximum propelling force through magnetization saturation of the MNPs. As previously demonstrated by our group, such technique was successful at maintaining microcarriers along a planned trajectory in the blood vessels based on tracking information gathered using Magnetic Resonance Imaging (MRI) sequences from artifacts caused by the same MNPs. Besides propulsion and tracking, the same MNPs can be synthesized with characteristics that can allow for the diffusion of therapeutic cargo carried by these MR-navigable carriers through the Blood Brain Barrier (BBB) using localized hyperthermia without compromising the MRN capabilities. In the present study, localized hyperthermia induced by an alternating magnetic field is investigated for the purpose of transient controlled disruption of the BBB and hence local delivery of therapeutic agents into the brain. Here, an external heating apparatus was used to impose a regional heat shock on the skull of a living mouse model. The effect of heat on the permeability of the BBB was assessed using histological observation and tissue staining by Evans blue dye. Results show direct correlation between hyperthermia and BBB leakage as well as its recovery from thermal damage. Therefore, in addition to on-command propulsion and remote tracking, the proposed navigable agents could be suitable for controlled opening of the BBB by hyperthermia and selective brain drug delivery.

4.2 Introduction

Brain tumours are extremely lethal and incredibly invasive and therefore, intervening with complex surgery is a top priority in most medical cases. Despite many efforts, drug delivery to the brain remains a challenge mainly because the Blood Brain-Barrier (BBB), which consists of endothelial cells that are tightly interconnected and cover all the interior of the cerebral vessel walls, is reputed to be insurmountable for most therapeutic molecules. In fact, nearly 98% of new drugs used in the Central Nervous System (CNS) to combat brain cancer and other chronic diseases cannot enter the brain following systemic administration [1]. On the other hand, systemic administration of toxic agents causes the active principles to distribute throughout all the organs. Therefore, while pathological regions are treated, they also promote side effects in healthy organs.

The extremely selective permeability of BBB and high cytotoxicity of anticancer drugs reinforce the importance of non-invasive targeted drug delivery for brain tumours and other chronic brain related disorders. Previously, our team has shown successful local delivery and tracking of therapeutic agents encapsulated in miniaturized magnetic carriers in the liver of a living animal by the gradient field of a modified Magnetic Resonance Imaging (MRI) scanner [2, 3]. The proposed carriers consist of therapeutic molecules and aggregates of Magnetic Nanoparticles (MNPs) with relatively high magnetization saturation embedded inside a biocompatible and biodegradable polymer, which serves as a transport mediator in the vasculature. This encapsulation also functions as a protective shield and prevents cells from further exposure to toxic drugs during the carriers' commute to a target area.

Besides MR-propulsion and MR-tracking, the same MNPs can be synthesized to offer characteristics that will allow them to become magnetically excited by an alternating field and to release their energy in the form of heat to their surrounding area. Inside brain microvasculature, such heat may thermally disrupt an intact BBB thereby creating a transient opening for the therapeutic agents to cross into the brain tissue. In fact, it has long been recognized that hyperthermia, otherwise known as elevation of body temperature, can lead to intense cellular stress and cause temporal disruption of the BBB [4-7] as well as death of cancer cells by enhancing cell sensitivity and vulnerability towards more established forms of cancer therapy, such as radiation and chemotherapy [8]. Coincidentally, a widely suggested method of

hyperthermia is based on excitation of MNPs inside an Alternating magnetic field [9]. This technique makes use of the radiofrequency of electromagnetic waves to heat the MNPs and therefore it is just as effective in deep biological structures as it is at the surface.

To our knowledge, hyperthermic disruption of the BBB via induction of MNPs by an Alternating magnetic field for drug delivery to the brain has not yet been reported. Here, the feasibility of this technique, as well as its integration with our pioneered MRI-based propulsion and tracking technique for intervention of microcarriers and microrobots in the vasculature are discussed. Furthermore, results in this study suggest that there may be a direct relationship between the elevated brain tissue temperature and the extent of the penetration of the desired drug molecules across the BBB. This implies that by controlling the amount of heat and exposure time, we can adjust the BBB opening for various molecular dimensions. Finally in this study, the recovery of the BBB from thermal damage is examined and investigated. Although this is a preliminary study, it is in light of such technique that non-invasive local drug delivery to the region of the brain may become possible.

4.3 Background Information

4.3.1 Blood-Brain Barrier (BBB)

All capillaries in the mammalian body including humans are composed of endothelial cells. In the circumventricular organs, most of the capillaries are fenestrated to allow for rapid exchange of molecules such as the therapeutic agents between blood vessels and surrounding tissue. In the brain however, very complex inter-endothelial tight junctions interconnect the endothelial cells. The tight junctions seal the cell interspace and form a diffusion barrier that markedly controls the flow of molecules across the epithelium. In addition to the tight junctions, pericytes with smooth muscle-like properties constitute the BBB [10]. Only small electrically neutral lipid-soluble compounds with low molecular mass of less than 400-500 Daltons (Da), or those small electrically neutral lipid-soluble compounds with low air-water partition coefficients and an average cross-sectional area of 50 Å^2, are able to diffuse passively through the BBB [11-13]. As mentioned before, this restrains admission of a considerable portion of pharmaceutical agents into the brain. For instance, currently many large drug molecules such as peptides, recombinant

proteins, monoclonal antibodies, antisense and non-viral gene medicines are ineffective for the brain [14].

One of the main functions of the BBB is to keep the neurotransmitters and agents that act in the CNS separate from the peripheral tissues and blood, so that similar agents can be used in the two systems without 'cross-talk' [15]. Also, because of the BBB's large surface area (180 cm^2 per gram brain [13]) and the short diffusion distance between neurons and capillaries (8–20 μm [16]), the extent to which a molecule enters the brain is determined only by the permeability characteristics of the BBB and that has a predominant role in regulating the brain microenvironment. That is why circumventing the BBB is a priority for any drug delivery mechanism to the region of the brain. Successful crossing of this barrier will have a profound effect on the treatment of many brain related disorders and therefore hyperthermia is being investigated for that purpose.

4.3.2 Hyperthermia

In modern oncology, hyperthermia generally refers to heating of organs or tissues in various ways to temperatures between 40°C and 45°C, at which point it causes moderate and reversible cellular inactivation [8]. In this regard, induction of MNPs by an AC field has been investigated for elevation of tissue temperature on a variety of fronts. Chief among those is the fact that the MNPs can act as very small heat sources once placed in an AC field, regardless of their depth inside the biological entity. On the contrary, other techniques such as RF, microwave and High Intensity Focused Ultrasound (HIFU), are not able to accurately target desired deep-seated tissues.

During local hyperthermia to temperatures near 42°C in the region of the brain ($\Delta T = 5$°C), morphological changes of individual endothelial cells in the monolayer lining of the micro-vessels begin to cause the tight junctions between adjacent endothelial cells to loosen, therefore allowing transport of large molecules through intercellular pathway [17]. Fortunately, the BBB seems to have the capability to restore functionality after brief hyperthermic disruption [18]. The rate of this restoration however, depends on the amount of heat and the exposure time.

4.3.3 Magnetic Nanoparticles (MNPs)

Among various methods of hyperthermia, whole body [5], microwave [6] and radiofrequency hyperthermia [7] are most commonly used to disrupt the BBB. In these techniques an entire region of the brain including neurons, astrocytes, vessel wall cells, and other glial cells are equally heated. In fact, this may be the reason for many undesirable acute side effects with hyperthermic disruption of the BBB by these techniques. Conversely, in the proposed hyperthermic disruption of the BBB by induction of MNPs inside an Alternating magnetic field, heat is exclusively dissipated to the ambient vessel wall cells by thermal conduction. Consequently, only the monolayer lining of the vessel walls and the endothelial cells are directly affected by the thermal stress.

The Specific Absorption Rate (SAR) or heat generated by the MNPs is mainly caused by three major mechanisms; hysteresis loss, Néel, and Brownian relaxations. Particles' physical properties as well as magnitude and frequency of the applied Alternating magnetic field determine the relative strength of each of these mechanisms. SAR is proportional to the time rate of change of temperature of a magnetic material and is given by the following formula [19]:

$$SAR = \frac{c\,V_s}{m}\frac{dT}{dt}$$
(1)

In (1), c is the specific heat capacity of the sample $(J{\cdot}l^{-1}{\cdot}K^{-1})$, m is the mass of the magnetic particles (kg), V_s is the total volume (m^3) and $\frac{dT}{dt}$ expressed in ºK·s^{-1}, is the temperature increment which is experimentally derived from the linear regression of the initial data points obtained from the time varying temperature curve. In the steady state, the difference in temperature ΔT is given by (2) where C is the concentration of the MNPs (mass of the particles per tissue volume) and λ represents the heat conductivity of a tissue volume with a radius R [20].

$$\Delta T = SAR\frac{C\,R^2}{3\lambda}$$
(2)

From (2) it is evident that higher concentration of MNPs per unit volume of the tissue leads to higher ΔT. In reality, for most therapeutic applications, the relatively poor energy transfer efficiency of the MNPs, i.e. poor SAR, introduces a great obstacle that hinders full functionality

or demands large administration of the MNPs at the biological target location leading to an increase in possible side effects. Therefore, scientists have long been searching for MNPs with the highest possible SAR.

In contrast to other forms of magnetization, superparamagnetism can prevent formation of nanoparticle clusters in the biological entity [9]. That is why ultra-small magnetite or superparamagnetic iron oxide (magnetite: Fe_3O_4) nanoparticles have been given special attention for hyperthermia. These particles are commercially available and their physical properties are vastly studied. In addition, magnetite nanoparticles have shown great biocompatibility, biodegradability and low toxicity [21]. The SAR value of these particles varies with respect to particle diameter and magnetic properties of the Alternating magnetic field. Our previous studies with superparamagnetic magnetite nanoparticles have shown promising results with regards to hyperthermia [22]. Table 3 summarizes some of the key parameters required to elevate the temperature of the brain tissue from 37 °C to 42 °C using commercially available particles. These parameters are induced from numerous *in vitro* experiments and simulations presented in [23]. In the same table, MNPs with much higher SAR but not yet commercially available are also reported.

Table 3: Parameters required to elevate tissue temperature 5°C by hyperthermia of magnetite

	Commercial [23]	Ref [24]
Composition	Fe_3O_4	$CoFe_2O_4$
Diameter (nm)	10 nm	9 nm
Magnetism	Superpara	Superpara
Coating	PMO	$MnFe_2O_4$
Alternating field amplitude (kA m^{-1})	4.5	37.3
Alternating field frequency (kHz)	160	500
SAR (W g^{-1})	61.02	~3000

The main difficulty of localized hyperthermic disruption of the BBB by induction of the MNPs is transportation of the MNPs and therapeutic agents through the vasculature to a desired area of the brain. Several criteria have been foreseen for such transportation. First, the carrier must have the

ability to geometrically fit into the target microvasculature. Second, the carrier must allow for maximum MNPs concentration at the target area to reach sufficient thermal levels. It is also very important to consider factors such as immunological reactions, excessive toxicity, premature degradation and fast excretion of the carrier by blood enzymes, or unexpected capture by non-targeted tissues that may affect the carrier behaviour. Compositions such as polyglycolic acid (PGA), poly(lactic-co-glycolic acid) (PLGA), and various environment-sensitive hydrogels are some of the well-known biomaterials for this purpose [25].

4.3.4 MRI-Based Drug Delivery System

Magnetic nanoparticles experience a thrust force when exposed to a gradient field. As seen in (3), this magnetic force, $\vec{F}_{\text{magnetic}}$ (N) is directly proportional to the volume of the MNPs, V_{ferro} (m^3) and their magnetization properties, $\vec{M}$ (A·m^{-1}) as well as the gradient of the magnetic field, $\nabla \vec{B}$ (T) [26].

$$\vec{F}_{\text{magnetic}} = V_{\text{ferro}} \cdot \vec{M} \cdot \nabla \vec{B} \qquad (3)$$

Magnetic Drug Targeting (MDT) technique uses this to concentrate therapeutic drugs adsorbed, entrapped or covalently linked to aggregates of MNPs at a superficial target location following a local intravenous injection [27]. The main difficulty for this technique however, is that it lacks the ability to target deep tissues [9]. Therefore, instead of a conventional approach most often based on an external magnet, an improved alternative method based on the three dimensional gradient magnetic field of the MRI was proposed by our team [28]. In this technique, due to the large main magnetic field of the MRI, aggregates of the MNPs become magnetically saturated once inside the relatively high homogeneous field of a clinical MRI scanner and therefore, relatively small shifts in the gradient field can steer them towards a target anywhere in the tissue. Furthermore, the aggregates of the MNPs create a magnetic distortion on the images acquired by MRI sequences. Therefore, the same MRI platform is able to track the aggregates in real-time and confirm their presence at the target.

In order to manoeuvre in the microvasculature, and to avoid fast degradation of the MNPs in the blood circulation system, as well as preventing them from dissociation, which greatly limits the thrust force and distortion for tracking purposes, the MNPs along with the therapeutic agents

must be encapsulated in biocompatible micrometer size carriers. Previously, our team was able to synthesize such complex microcarriers and to use them to target a specific region of the liver of a living rabbit [3] prior to the successful release of the therapeutic agent. The vascular structure of the liver however is very different from that of the brain. Therefore, the proposed micro-entities may require appropriate modifications before attempting MRN towards the brain.

4.4 Methods

Various studies evaluated the required amount of thermal exposure and duration for temporal disruption of the BBB based on imposition of thermal stress on the tight junctions [29, 30]. According to the findings of these studies, the ideal temperature for transient disruption of the BBB falls in the range of 40 °C – 45 °C for a period of 30 minutes.

4.4.1 BBB Staining

Staining of the BBB is a traditional method for evaluating BBB leakage. Evans blue, an exogenous dye tracer is used here to assess the integrity of the BBB following a hyperthermic disruption. The dye molecules are able to easily diffuse through the fenestrated endothelial cells of all capillaries except those of the brain due to a functional BBB. However, once the BBB is compromised, Evans blue enters the brain and it fluoresces with excitation peaks at 470 and 540 nm and an emission peak at 680 nm [31]. Histological staining techniques can therefore reflect the extent of BBB leakage by studying the intensity of Evans blue dye in the brain.
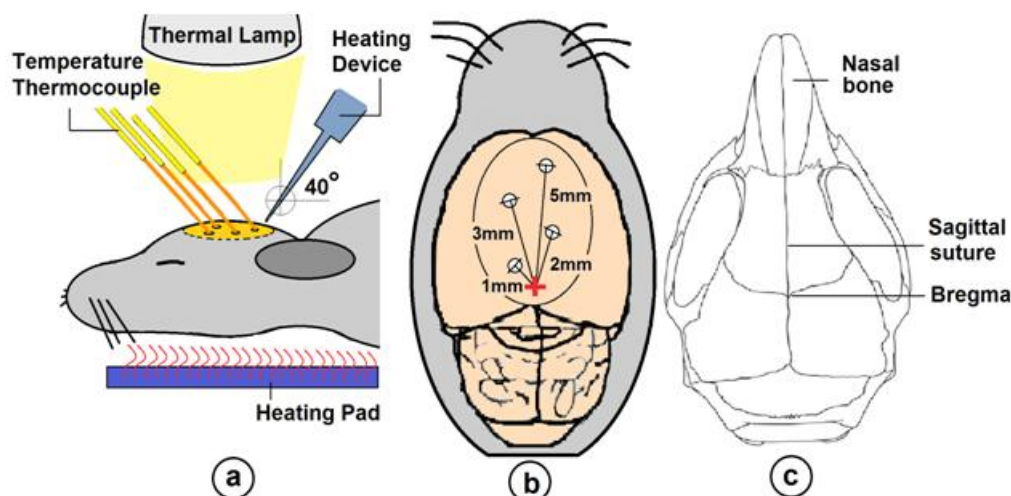
Figure 4.1: Experimental Schematics

a) Experimental schematics for Part i. b) The dorsal view of the brain. The cross in the middle represents the position of the heating point. c) Heating was done over the skull near Bregma.

4.4.2 Experimental Procedure

In the primary steps of this study, distribution of heat from an external heating device on the brain of living mice as well as feasibility studies in regards to hyperthermic disruption of the BBB were assessed. For this purpose, a two-phase *in vivo* experiment was executed:

4.4.2.1 Phase *i*

Five mice were separately anesthetised by intravenous injection of 40 mg kg^{-1} body weight of pentobarbital. Quickly after, each animal was positioned on a stereotaxic frame and the head of the animal was secured in place. Then, by removing the skin, the surface of the skull of the animal was exposed. At this point, four small holes (~1mm in diameter) were drilled into the skull at precise locations shown in Figure 4.1a. Next, fibre optic thermocouples were placed inside the holes. An external heating device was used to focally elevate the temperature of a small region of the brain near Bregma (see Figure 4.1c.) at a 40° angle for duration of 30 minutes. While the thermocouples recorded changes in temperature at specific distances (1, 2, 3, 5mm respectively) away from the heating point (see Figure 4.1b.), a rectal thermometer monitored the internal body temperature of the animal. Since the body temperature drops rapidly during anaesthetic state, each animal was placed on a thermal pad. In addition, a heating lamp was

placed 5 cm above the skull to keep the brain temperature at 37 °C during the experiment. As a consequence, the body temperature was always kept at 36.5 °C to 37 °C.

The purpose of this experiment was to examine the thermal distribution in the brain tissue. This resulted in a thermal map of the tissue represented in Section IV. It is important to mention that, the environment in the experimental suite was kept thermally neutral during all experiments.

4.4.2.2 Phase *ii*

The purpose of this part of the experiment was to examine the feasibility of hyperthermic disruption of the BBB as well as its recovery period from thermal damage using Evans blue staining technique. Here, nine mice, each 6-8 weeks of age, were randomly divided into three identical groups. In contrast to the previous part, no holes were drilled into the exposed surface of the skull of these animals. In order to correlate temperature patterns with stains left from the Evans blue dye, the heating parameters for all groups were kept the same as was described in the first part of this experiment.

4.4.2.2.1 *Group I*

All mice in this group were intravenously injected with 40 mg kg^{-1} of body weight of pentobarbital and 4 ml kg^{-1} body weight 2% Evans blue dye. As in Part i, quickly after anaesthesia each animal was positioned on a stereotaxic frame where a thermal pad and the lamp kept the body temperature steady at near 37 °C. Just as before, the heating device was also placed at a 40° angle near and above Bregma and the exposure time was set to 30 minutes. All animals in this group were sacrificed one hour after injection of the dye. The animals' brains were extracted and immersed in isopentane and kept on dry ice for further analysis.

4.4.2.2.2 *Group II*

To examine BBB's ability to recover following hyperthermic disruption, all mice belonging to this group were prepared the same way as done in Group I except that the dye was injected 2 hours after 30 minutes of thermal treatment had ended. Exactly one hour after injection of the dye, the animals were sacrificed and their brains were removed, immersed in isopentane and kept on dry ice for further study.

4.4.2.2.3 *Group III*

All mice in this group served as controls and were injected with the Evans blue and before they were sacrificed. There was no staining of the dye found on the brain tissue of the mice from this group.

4.4.3 Data Analysis

Extracted brains were embedded in Optimal Cutting Compound where 50-micron coronal slices were made at −20 °C in a cryostat. Results are shown in the next Section.

4.5 Results

Results from the first part of the experiment are shown in Figure 4.2. In this figure, recorded temperatures from 1mm and 2mm distances away from the heating device quickly raised once heating started and rapidly plateaued at approximately 44.3 °C and 39.4 °C respectively. Also, at the distances of 3mm and 5mm away from the heating device, temperatures reached 37.8 °C and 37.6 °C respectively.
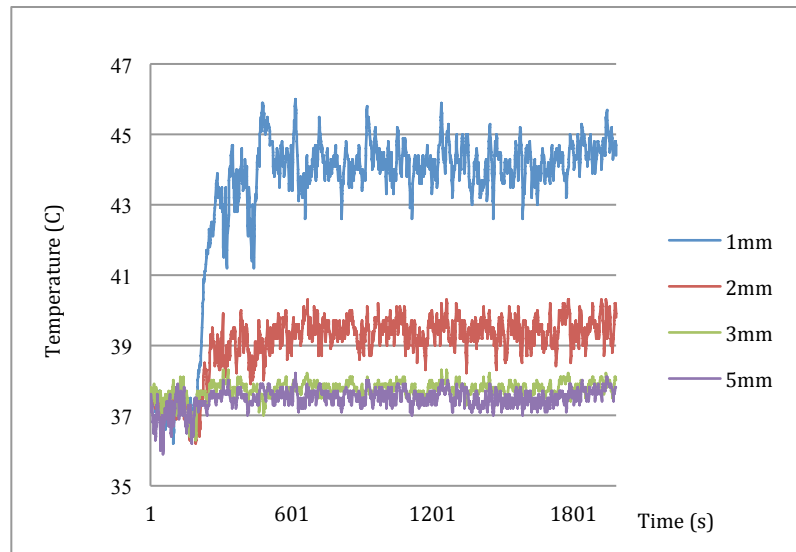
Figure 4.2: Temperature profile using the heating element.

Elevation of temperature in the brain tissue of a mouse by an external heating element

In phase ii, Evans blue dye was expected to have distributed throughout the entire body except the brain where they are forbidden entry prior to the hyperthermic disruption of the BBB. Following hyperthermia, the extracted brains from the animals of Group I revealed that

hyperthermia could indeed disrupt the BBB and allow entry of a large and heavy molecule such as Evans blue into the brain tissue. Figure 4.3 illustrates what the extracted brain from a mouse in this group resembles. As it is seen in this figure, the integrity of the BBB at where heat was applied was compromised leading to staining of that region of the brain.
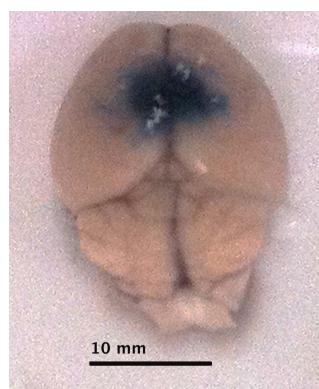
Figure 4.3: Appearance of the Evans blue dye near and around the heating point

(Group I Animal #1)
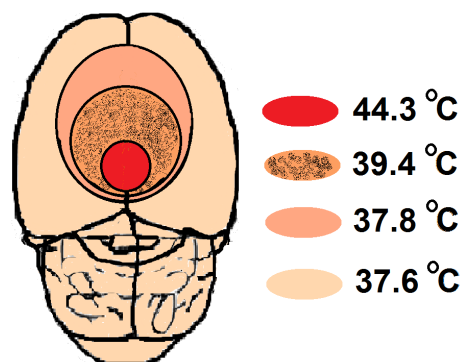
Figure 4.4: Brain Thermal Mapping

A correlation between findings depicted in Figure 4.2 and the sketch shown in Figure 4.1b, lead to a thermal mapping of the brain in Figure 4.4. The temperature curves presented in Figure 4.2 indicate conduction of heat in the brain tissue regardless of the method heat has been produced. As mentioned before, MNPs are also able to create such thermal energy by relaxation processes. Thus, in the presence of micro-robots near the Bregma, distribution of heat generated by excitation of the embedded MNPs inside an Alternating magnetic field would be similar to Figure 4.2. That is why the MNPs are considered the key component of the proposed micro-robots.

Results from the histological examination of the extracted brains are tabulated and presented in Table 4. As seen, all animals from the first group except one (#3) were affected by hyperthermia where Evans blue left a visible stain on the brain tissue around Bregma. It is believed that technical problems caused the anomaly for animal #3. Animals from the second group that received a 2-hour recovery period, showed substantial lower leakage area compared to the animals in Group I. The location of the leakage of the BBB and visible stains were also very close to the heating device where according to Figure 4.2 must have reached to temperatures higher than 40 °C. Therefore, although the BBB seem to have partially or in case of Animal #1 fully recovered from hyperthermic disruption, the recovery period may have not been sufficient for

complete rejuvenation of the BBB. This requires further investigation. No evidence of BBB leakage for Group III could be found.

Table 4: Histological examination of the BBB leakage of Evans blue dye

Phase II	Animal #	Heating point position away from Bregma (mm)	Diameter of BBB leakage of Evans blue (mm)
Group I Hyperthermic Disruption	1	1.6	4.22
	2	2.5	2.46
	3	1.66	0
Group II Recovery from Hyperthermia	1	2.3	0
	2	2.4	0.62
	3	2.2	1.98
Group III Control	1	N/A	0
	2	N/A	0
	3	N/A	0

4.6 Discussion

Overcoming the BBB is an important field of current research that seeks a technique to reach the inside of the brain. To achieve brain localized drug delivery and increased efficacy, this project suggests that the therapeutic agents must be administered to the brain by means no more invasive than an intravenous injection of microcarriers or microrobots consisting of MNPs and therapeutic agents capable of remote propulsion and tracking compatible with MRN, and on-command actuation in the brain. The results of the preliminary experiments presented in this paper indicate that temperatures of 38 °C and higher for an exposure time of 30 minutes are required for effective hyperthermic disruption of the BBB for crossing of large and heavy drug molecules. This crossing however is governed by the change of thermal energy or ΔT, which according to (2), is directly depended to the value of SAR. Therefore, controlling SAR leads to controlling the level of BBB leakage. For hyperthermia by induction of MNPs inside an Alternating magnetic field, as intended in this project, the SAR mainly depends on the field frequency and amplitude. Varying these parameters therefore, results in adjusting the BBB leakage to our favour. Thus, we have shown that this technique not only can be highly localized, it also provides advanced control over the opening of the BBB into the brain.

It must be mentioned that disturbance of the BBB at high levels may cause vasogenic edema and energy metabolic failure leading to subsequent structural brain damages. Evidently, the degree of

pathophysiological changes in the vascular system of normal brain tissue is dependent on temperature and duration of heating. To minimize local hypo-perfusion and local brain cell death, thermal dosage as well as exposure period must be carefully selected and performed in a controlled environment.

4.7 Conclusion

The main goal of modern pharmacology is the transport of drug molecules to specific targets while maintaining therapeutic efficacy. However, nearly 98% of drugs cannot enter the brain following systemic administration. Our group has previously pioneered a MRI-based drug delivery platform referred to as MRN that employs microcarriers or future microrobots capable of interventions in the vasculature. Here, our team is looking to equip these micro-entities with hyperthermic capabilities to disrupt the BBB and therefore be as effective in delivering therapeutic agents in the brain. This ability comes from the fact that these micro-entities rely on embedded MNPs that are excited once placed inside an alternating magnetic field. This excitation leads to moderate elevation of temperature and thus transient disruption of the BBB. In light of this technique, local drug delivery for various disorders such as brain tumours, psychiatric, neurological and neurodegenerative disorders may also become feasible.

CHAPTER 5   ARTICLE 2 - REMOTE CONTROL OF THE PERMEABILITY OF THE BLOOD–BRAIN BARRIER BY MAGNETIC HEATING OF NANOPARTICLES: A PROOF OF CONCEPT FOR BRAIN DRUG DELIVERY

Seyed Nasrollah Tabatabaei, Hélène Girouard, Anne-Sophie Carret, Sylvain Martel

5.1 Abstract

Despite advances in neurology, drug delivery to the brain remains a substantial challenge. This is mainly due to the insurmountable and selective nature of the blood–brain barrier (BBB). In this study, we show that the thermal energy generated by magnetic heating (hyperthermia) of commercially available magnetic nanoparticles (MNPs) in the brain capillaries of rats can transiently increase barrier permeability. Here, the fluorescent Evans Blue (EB) dye was used to verify the BBB integrity. Results indicate a substantial but reversible opening of the BBB where hyperthermia is applied. Also, in this investigation, analysis of CD68 immunoreactivity, an indicator of inflammation, implies that this technique is not associated with any inflammation. We have previously investigated theranostic (therapeutic and diagnostic) capabilities of the MNPs, therefore, the findings presented in this investigation are particularly encouraging for a novel targeted drug delivery system to the brain.

5.2 Introduction

There has been a lot of ink given to the enormous progress that scientists around the world have made in the treatment of brain related disorders, yet drug delivery to the brain remains a challenge [1]. This is mainly due to the insurmountable and selective nature of the blood–brain barrier (BBB). This barrier consists of tightly interconnected endothelial cells that circumferentially form the interior lining of the cerebral vessel walls and prevents harmful substances from entering into the brain. By extension, most drug molecules and available therapeutics are not able to reach the brain. According to Pardridge [2], more than 98% of small molecules including therapeutics do not cross this barrier. The objective of the present

investigation is to provide proof that magnetic heating (hyperthermia) of magnetic nanoparticles (MNPs) by a low radiofrequency (RF) field can increase BBB permeability without perturbing other brain cells. In order to make this proposition a clinically viable technique, it is first essential to show that the opening of the BBB is local and it is entirely reversible.

Recent literature is unanimous that improving access to the BBB holds substantial potential of improving therapeutic response to various brain related disorders including brain tumours [3]. In that regard, MNPs have been vastly researched for therapeutic and diagnostic purposes [4,13,12] as well as drug delivery to the brain [5–7]. The synergy between the current study and the ongoing research on MNPs could be pivotal in bringing more effective drug delivery technique with less toxicity to the clinic and to the market.

The permeability of the BBB between adjacent endothelial cells (tight junctions) is known to increase in response to physiologically relevant temperature increase (38–39 °C) [8,9]. We have previously observed reversible disruption of the BBB in this temperature range on the surface of the brain [10]. For the first time in this study, we examined BBB permeability at the presence of moderate heat dissipated from magnetic heating of MNPs. The physics behind magnetic heating is beyond the scope of this paper, but in summary, a low radiofrequency (RF) field can magnetically excite MNPs to release energy in the form of heat to their surroundings through a mechanism called Néel relaxation [11]. Basically, each time the magnetic moments of the MNPs align with the alternating direction of the RF field, they release this energy once they relax back to their original direction. The present investigation focuses on the influence of magnetic heating of MNPs on BBB permeability in anesthetised rats. This preliminary experiment provides evidence that our proposed approach goes beyond former methods to access the brain tissue with higher spatial precision, advanced control and lower immune reaction.

5.3 Material and methods

5.3.1 Characterization of the MNPs

MNPs with eight different coatings dispersed in separate aqueous solutions were kindly provided by Chemicell GmbH (Berlin, Germany). A small drop of diluted suspension from each sample was positioned on a 200-mesh carbon film and dried by air. TEM images were acquired on a Jeol JEM-2100 field-emission gun (École Polytechnique de Montréal, Canada) operated at 200 kV

(see Supplementary Information Appendix B, S. 2). The crystalline structure of the MNPs was analyzed by an X-ray diffractometer (X'Pertmodel from Philipps) using a Cu-Ka radiation (λ of 1.541 Å) at 50 kV and 40 mA (see Supplementary Information Appendix B, S. 5). The superparamagnetic properties and magnetization of the MNPs were measured using a vibrating sample magnetometer (VSM) device (EV5, Magnetics, Université de Montréal, Canada) at room temperature (see Supplementary Information Appendix B, S. 3).

5.3.2 Magnetic heating by radiofrequency (RF) field

In this study, the RF field was set to 7.6 kA m^{-1} at 150 kHz by a 2-kW HotShot induction heating amplifier (Ameritherm Inc., New York). To apply this field, a custom-made coil was specifically designed to generate the required field strength and frequency fitted for the head of the animal as described in Supplementary Information Appendix B, S. 6. In order to determine which commercially available MNPs would provide higher heating profile, first various coatings of the MNPs were individually placed inside the RF field (see Supplementary Information Appendix B, S. 1). The temperature rise for every sample was then recorded in respect to time. Finally, the sample with the best heating profile was chosen for the *in vivo* experiments.

5.3.3 Animal protocol

All animal procedures were performed according to the guidelines approved by the Ethics and Experimentation on Animal Committee (CDEA) of the University of Montreal. Twenty-four pathogen-free Sprague-Dawley rats (250–350 g) were examined to confirm the efficacy of the proposed approach. The animals were randomly separated into five groups, namely i) Control (n = 4), ii) Control RF (n = 4), iii) Normothermia (n = 4), iv) Hyperthermia (n = 8) and v) Recovery (n = 4). The appropriate exact protocol sequence for each group is tabulated in Table 5.

animals (RFU analysis) and 2% glutaraldehyde (stronger preservative for TEM analysis) for the last animal, to flush all the blood and EB dye out of the vascular system. Once perfusion was completed, the brain of the animal was extracted and placed inside a preservative solution (4% PFA or 2% glutaraldehyde respectively).

• Hyperthermia: An average of 60 μL PMO-coated MNPs was injected into the left MCA as described for Normothermia. Each animal was then exposed to the RF field for 30 min. The animals were then sacrificed by an intra-cardiac perfusion of 60 cc 0.9% saline followed by 100 cc 4% PFA for 7 animals (RFU analysis (n = 3) and immunohistochemistry (n = 4)) and 2% glutaraldehyde for the last animal (TEM analysis).

• Recovery: Animals in this group (n = 4) received the same PMO- coated MNP dosage via the left MCA as discussed before. They were then exposed to the RF field for 30 min and kept alive under anaesthesia for 2 h. Then the animals were infused by 0.3 mL EB dye via the tail vein. After 30 min, the animals were sacrificed via an intra-cardiac perfusion as explained in Normothermia.

• Control and Control RF: Animals without MNP injection in the Control RF group (n = 4) were exposed to the RF field for 30 min and sacrificed by intra-cardiac perfusion as described in Normothermia. Animals in the Control group (n = 4) did not receive MNPs and were not exposed to the RF field. These animals were sacrificed via an inter-cardiac perfusion 30 min after the dye was introduced in the vasculature.

5.4 MNP localization using magnetic resonance imaging

Images of the selected brain samples were acquired by a 7 Tesla magnetic resonance scanner (Agilent Technologies). The samples were securely placed inside a custom-made coil with 2 channels and positioned in the middle of the magnet. To identify the MNPs in the brain samples, contrast-enhanced T2 spin-echo sequences were acquired using the following parameters: repetition/echo time, 3000 ms/20 ms; slice thickness, 1.00 mm; matrix size, 512 × 512; and pixel spacing (in plane resolution), 0.0488 mm^2.

5.5 Analysis of BBB opening using Evans Blue

Three brains from each group were sectioned coronally into 200 μm slices, from rostral to caudal on a vibratome (Leica, Germany) and collected on gelatin-coated glass slides. Sections were then mounted using a mounting medium and the EB staining was directly visualized and imaged with an epifluorescent microscope (Leica DM2000, Germany). The EB containing samples were imaged at 1× in phase-contrast mode with a 9 ms exposure time. Images were exported for luminosity analysis in tagged image file format (TIFF).
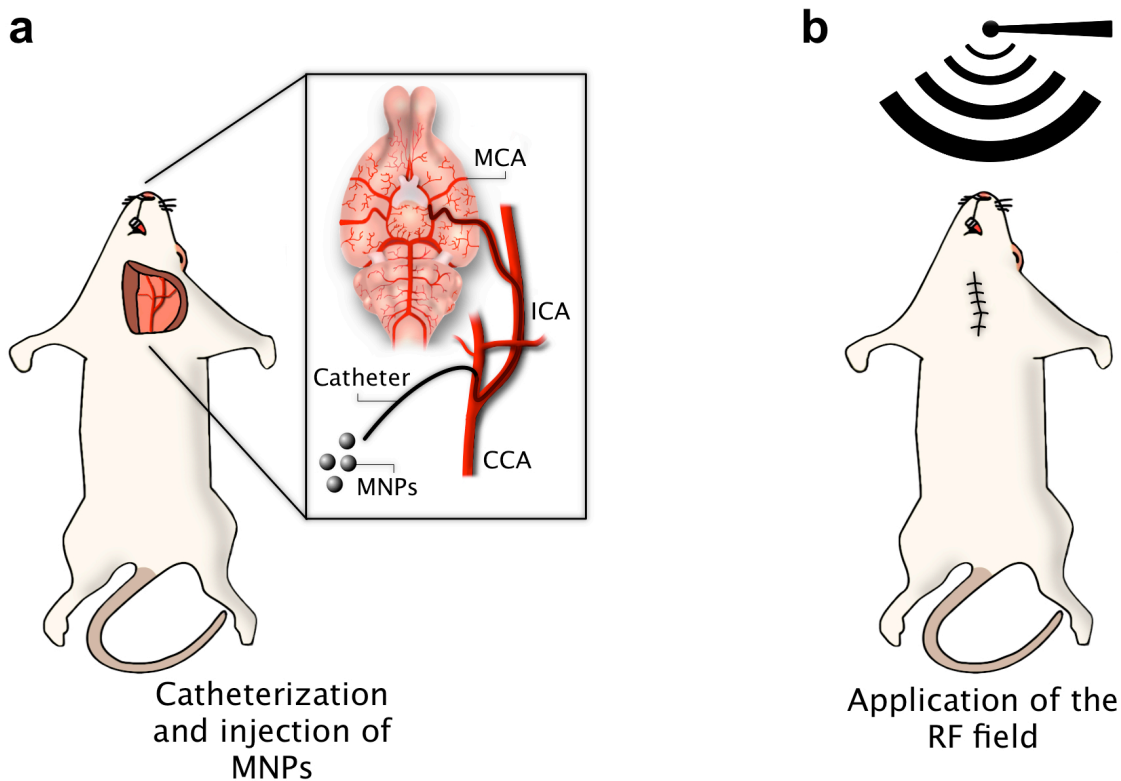
Figure 5.1: The schematics for the experimental procedure for reversible hyperthermic opening of the BBB.

a) Illustrates the MNPs being injected via a microcatheter that is inserted into the External Carotid Artery (ECA) and advanced to the Internal Carotid Artery (ICA) where its tip is finally positioned near the MCA in the Circle of Willis. b) The anesthetised animal is exposed to the RF field for 30 min.

5.6 Evans Blue fluorescence data analysis

Luminescence intensity thresholds for the contralateral images were computed and applied to their ipsilateral counterparts. The threshold was defined as the maximal luminescence intensity

for 95% of pixels in the contralateral side of the brain. EB concentration comparisons were assessed across all groups using one-way ANOVA and Bonferroni Multiple/Post-Hoc tests. Therefore, the ratio of the difference in the luminescence intensity between the two hemispheres with respect to the area of the left hemisphere was defined as the amount of fluorescence for each particular slice. These ratios were then added and averaged over a number of brain samples in each group (n = 3).

5.7 Analysis of BBB opening using transmission electron microscopy (TEM)

A group was selected for TEM imaging and fixated in 2% glutaraldehyde in PBS for 24 h. Transverse sections of the brain (200 μm thick) were produced with a vibratome and kept in antifreeze solution at −20 °C until processed for electron microscopy. The sections were washed with PBS, followed by a post-fixation with 1% osmium tetroxide in PBS for an hour at 4 °C. The brain sections were dehydrated in a graded series of ethanol (30–100%) and embedded in Epon. Ultrathin sections (70–80 nm) were cut using ultra-cut microtome and placed on copper grids for analysis. The grids were contrasted with uranylacetate and lead citrate and examined using a Philips CM100 electron microscope.

5.8 Index of brain inflammation

The detection of activated microglia/macrophages, an indicator of brain inflammation, was performed on 40-um-thick floating coronal sections from Hyperthermia group (n = 3). Sections were sequentially washed for 30 min with PBS. These sections were then incubated at 37 °C for 45 min, followed by 1 h in blocking solution of PBS containing 10% BSA, 5% NGS plus 0.3% Triton X-100 at room temperature. For CD68 immunostaining, Mouse Anti-Rat CD68 Monoclonal antibody (Millipore, USA) was used at a dilution of 1:150 in PBS blocking solution containing 0.5% BSA, 5% NGS plus 0.3% Triton X-100 at 4 °C overnight and then washed for 30 min with PBS. For visualization by fluorescence, the sections were exposed to Alexa fluor 546 Goat Anti-Mouse (Life technologies, USA) at a dilution of 1:200 in a PBS solution for 2 h on ice. Finally, the sections were rinsed and mounted on slides. Staining was observed under a 20× objective by confocal laser scanning microscopy (Olympus). To ensure the accuracy of the procedure, these steps were followed on a positive control model. For that, an animal was

anesthetised by an i.p. injection of 0.53 mL pentobarbital (1.6 mL kg^{-1}) and sacrificed 2 h after receiving an intra-cranial injection of 100 μL lipopolysaccharide (LPS).

5.9 Results

5.9.1 Physical properties of MNPs

Magnetic properties of the MNPs play a critical role in their heating ability by an RF field. Superparamagnetic magnetite (Fe$_3$O$_4$) nanoparticles have shown great potential in this regard [12]. The magnetic heating ability of eight different magnetite nanoparticles was examined *in vitro*. Among these commercially available MNPs, poly(maleic acid- co-olefin) or PMO-coated MNPs show the highest thermal effect when excited by the RF field (data shown in Supplementary Information Appendix B, S. 1). This led to the selection of magnetite MNPs with PMO coating for the *in vivo* portion of this investigation.

5.9.2 Characterization of MNPs

Transmission electron microscopy (TEM) was used to measure the relative size distribution of the PMO-coated MNPs. As shown in Supplementary Information Appendix B, S. 4, these particles had a relatively widespread distribution ranging approximately from 3 to 18 nm in diameter, peaking at 11 and 13 nm. The crystal structure of these nanoparticles measured by X-ray diffractometer confirmed that these nanoparticles were in fact magnetite (see Supplementary Information Appendix B, S. 5). The vibrating sample magnetometer (VSM) measurements show low coercive field and lack of hysteresis which further proves the superparamagnetic nature of the nanoparticles. According to these findings, the PMO-coated MNPs were magnetically saturated (*Ms*) at 60.27 emu g^{-1} (data shown in Supplementary Information Appendix B, S. 3).

5.9.3 BBB opening by magnetic heating

All animals were randomly separated into five groups, namely i) Control, ii) Control AC, iii) Normothermia, iv) Hyperthermia and v) Recovery. The appropriate protocol for each group is tabulated in Table 1 and described in the previous section. Images of the extracted brains from each group are displayed in Figure 5.2. From the camera section of these images it is clear that in the case of Normothermia group where the thermal energy was not applied, the MNPs (seen in

black) remained inside the vasculature near the target. In Hyperthermia however, only a large blue stain that is resulted from diffusion of the EB dye into the tissue is apparent. Conversely, in Recovery neither the blue stain nor the black residue of the MNPs is visible (see Figure 5.2— Camera).

5.9.4 MNPs as MRI contrast agents

The presence of the MNPs in the tissue creates distortions on the images acquired by the MRI (see Figure 5.2— MRI). While after the application of magnetic heating (in Hyperthermia and Recovery), MNPs are no longer visible by the naked eye, the distorted images provide evidence that the MNPs in fact continue to exist in the target. Nevertheless, any small quantity of the MNPs can generate such distortions, therefore, we cannot speculate on the concentration of MNPs that has remained in that location.

5.9.5 Fluorescent EB dye

Selected images taken by the epifluorescence microscope are presented in Figure 5.2— Epifluorescence Microscope. From these images, Hyperthermia seems to have a higher rate of luminosity than other groups. To further examine this observation, brains from all experimental groups were sliced, imaged and analyzed. The result of this analysis is shown in Figure 5.3. In this figure, each column represents the relative fluorescent units (RFU) computed from all brain samples in a group. As expected for Hyperthermia ($p < 0.05$ vs. Control), the RFU is clearly higher than in any other group. Also in the case of Recovery ($p < 0.01$ vs. hyperthermia), the amount of fluorescent units counted after 2 h of recovery from magnetic heating is substantially lower than Hyperthermia and Normothermia.
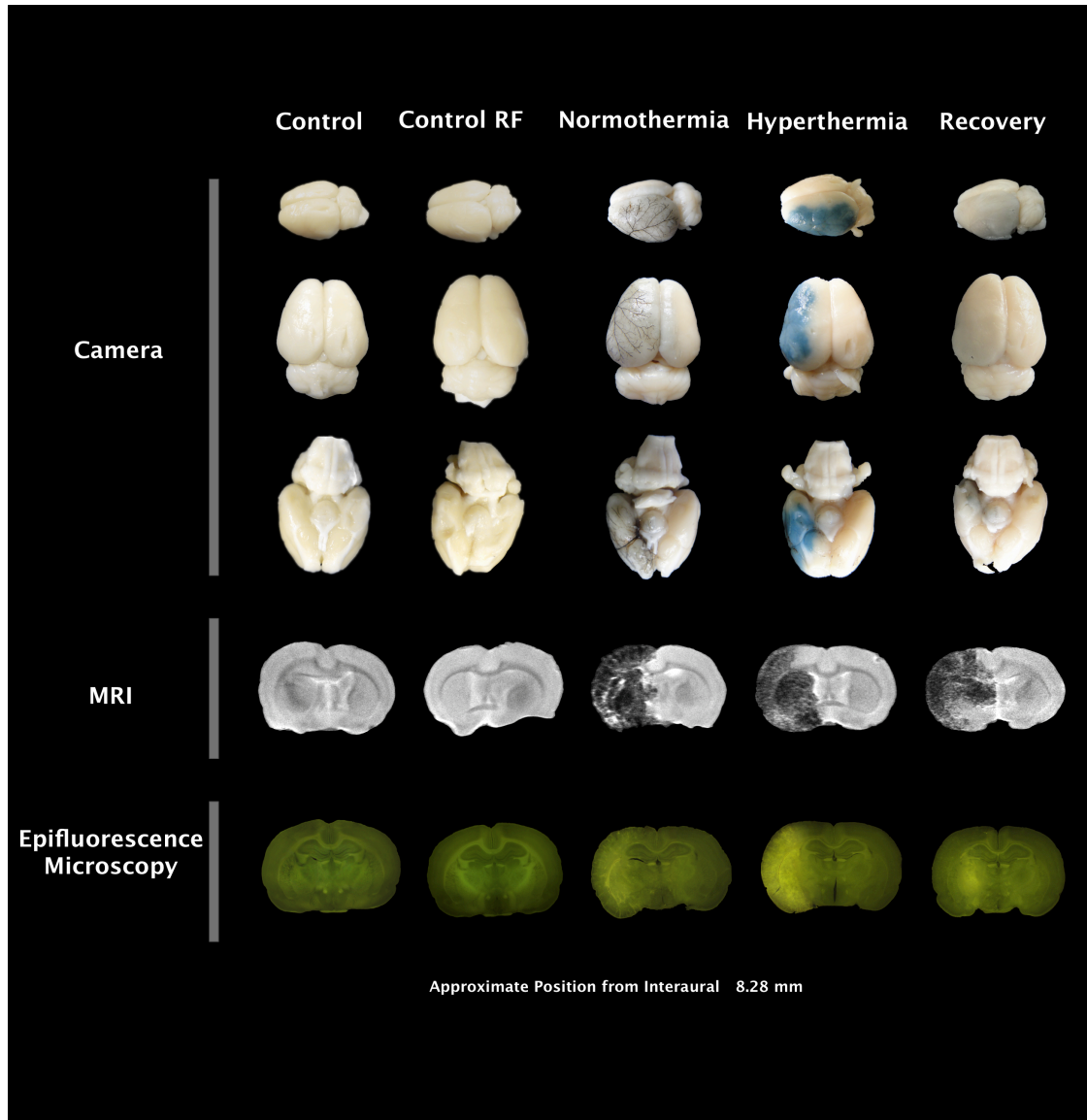
Figure 5.2: Results of randomly selected brain samples from every experimental group is shown in this figure.

i) Camera: images taken by a digital camera from 3 different angles. The fact that after intra-cardiac perfusion the EB dye is visible indicates that it has successfully diffused into the target brain tissue (Hyperthermia). In the case of Normothermia where the RF field was not applied, the MNPs (black) remained inside the vasculature. In the Recovery group, there is no indication of dye diffusion nor MNPs residue in the target area. ii) MRI: these images are taken by a 7 Tesla animal MRI. The MNPs are shown as distortions of the image (black) around the target tissue in the left hemisphere for the Normothermia, Hyperthermia and Recovery groups. iii) Epifluorescence Microscope: images from 200 μm slices (approximately 8.28 mm from interaural) are shown under this microscope. The fluorescent EB dye has a higher rate of luminosity in Normothermia than any other group.

Evans blue fluorescence
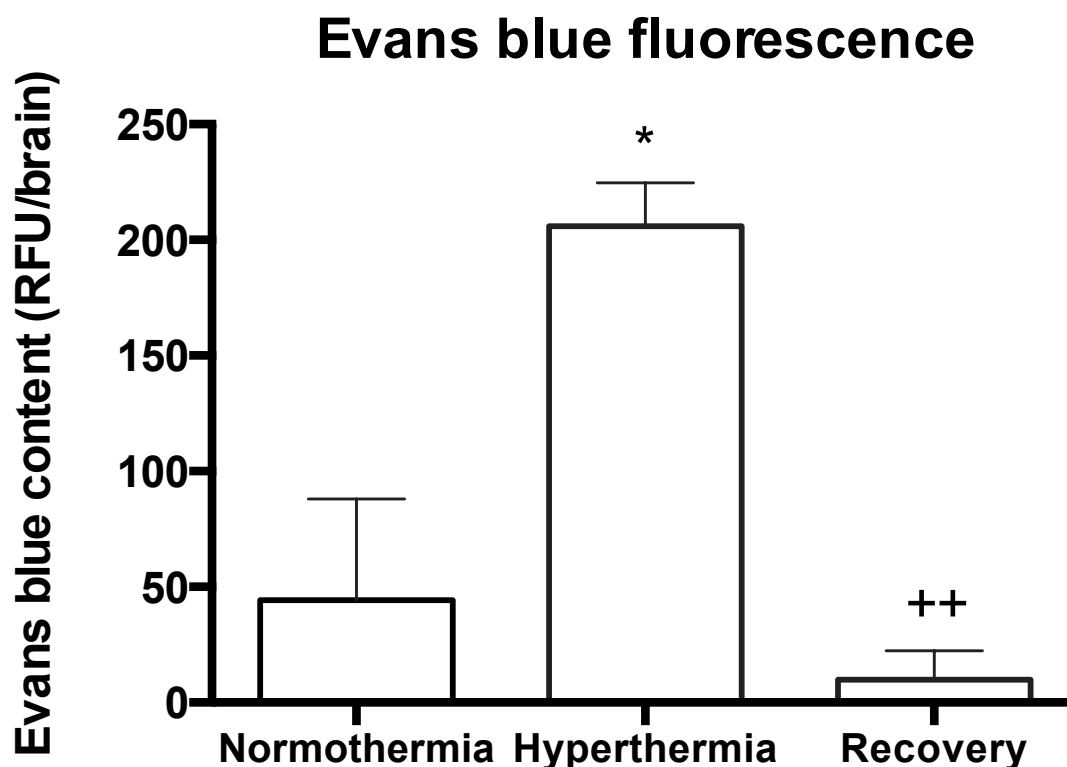
Figure 5.3: Relative fluorescence unit

This graph represents the relative fluorescence unit (RFU) for the Normothermia, Hyperthermia and Recovery groups. These values are in fact average of the sums of the amount of fluorescence that were computed from three brains in each group. Expectedly, Normothermia (* $p < 0.05$ vs. Control) has the highest RFU value and Recovery (++ $p < 0.01$ vs. Hyperthermia) has the lowest one.

5.9.6 TEM analysis of the BBB

A brain from each experimental group was specially prepared for TEM imaging as described in the previous section. Some of these images are presented in Figure 5.5. For Hyperthermia and Normothermia, the MNPs are clearly visible inside the capillaries (shown by an arrow in Figure 5.5b and c). Red blood cells and macrophages as well as cellular debris are also easily detected in these capillaries. There was no difference between images from the Control group and the Control RF group. Last but not least, TEM images from the Recovery group indicated a substantial decrease in the concentration of the MNPs inside the capillaries.

5.9.7 Brain immune response

As described in the previous section, immunohistochemistry analysis was performed to detect the presence of the CD68 marker in brain tissue following BBB opening by magnetic heating. The presence of this marker indicates that the brain immune system has been activated. As illustrated in Figure 5.4a, samples from the injected brain with lipopolysaccharide (LPS) (positive control) were thoroughly lit by the CD68 fluorescent markers on activated microglial and/or microphages. Remarkably, other than expected evidence of monocytes in the capillaries (reticuloendothelial), no other trace of CD68 was found in the parenchyma of brains that were treated with magnetic heating.

5.10 Discussion

5.10.1 Transient opening of the BBB

In this investigation, we propose a novel method to deliver therapeutic agents to the brain tissue. The objective of this study is to provide preliminary evidence that under the influence of RF field the thermal energy released from the MNPs can transiently increase BBB permeability. Our team has previously shown propulsion of the same MNPs in the vasculature towards a target site using a modified clinical MRI [20]. In this study, we used a simple cannulation technique to deliver MNPs to the surface of the target endothelium (the left MCA). We believe that the combination of the transient BBB opening and the MRI-based targeting technique can have a high impact on localized drug delivery to the brain.

Due to the dismal prognosis of patients with brain related disorders, overcoming the BBB for drug delivery is highly desirable. Apart from surgery, which is the most invasive yet standard clinical approach for many types of brain tumours, the conventional administration of therapeutics is rigorously limited by poor drug penetration. In addition, some disorders are located in the middle of the brainstem, where they infiltrate amidst the nerves, thereby making surgery practically impossible. Transient disruption of the BBB can be attained by intra-arterial injection of an osmotic agent such as mannitol [14], or alkyl-glycerol [15]. However, osmotic agents lack targeted delivery and they can result in widespread BBB disruption with the potential for deleterious consequences. High intensity focused ultrasound (HIFU) is among prominent strategies for local delivery of therapeutics to the brain. This technique employs an acoustic

energy to vibrate intravenously administered micro-metric lipid-encased perfluorocarbon gas microbubbles (MBs) near the target endothelium. The oscillating MBs create a mechanical stress on the endothelial tight junctions thus allowing therapeutics to enter the brain [16,17]. Despite its enhanced synergistic effects, MBs have short half-lives in the vasculature and are quickly up-taken by the reticuloendothelial system when circulating through the liver. On the other hand, when MNPs are deposited, they remain on the surface of the target endothelium for the duration of our technique. Furthermore, in the presence of HIFU, MBs undergo a phenomenon that leads to the formation of high pressure shock waves as well as fast-moving liquid jets [18], which can seriously damage the cellular membrane near a rigid surface in the brain. Also, the sound waves propagate non- linearly over a large region of biological structures before converging into a focal point, which may lead to undesirable side effects. The affinity of the MNPs on the surface of the target endothelium however, assures that the thermal energy is exclusively dissipated to the BBB. Therefore, this cell-specific approach ultimately minimizes potential side effects and overheating of the surrounding structures such as astrocytes and neurons. In addition, HIFU is also debatably performed without the benefit of real-time visualization. In other words, the time interval between intravenous administration of MBs and their arrival at the target location prior to the application of the acoustic energy is often roughly approximated. This and HIFU's current relatively large focal point ($1 \times 1 \times 7$ mm^3 [19]) result in low spatial resolution for intervention in a highly sensitive organ such as the brain. The MNPs in our cell-specific method can be visualized as artifacts on the images of the MRI, and relatively low frequency RF field is just as effective in deep structures as it is at the surface of the brain.

5.10.2 *In vivo* transient opening of the BBB by hyperthermia of MNPs

To examine BBB integrity, all animals received an intravenous dosage of the florescent EB dye which is a tetrasodium diazo salt marker of albumin extravasation (MW 68 kDa [21]). Other dye molecules with different molecular weights will be used to further measure BBB opening in the future studies. We also used rat models due to their remarkable genetic overlap with humans and the availability of well-documented protocols. As shown in Figure 5.2— Camera, the dye molecules could not cross an intact BBB (Control, Control RF, Normothermia, and Recovery), but after magnetic heating of MNPs that were injected into the left MCA, the dye noticeably penetrated into the target brain tissue. Interestingly, while the exact time it may take for the BBB

to recover from magnetic heating is yet to be determined, after a two-hour recovery period the dye could no longer cross into the brain tissue. This signifies that the BBB is able to naturally redeem full functionality and recover from magnetic heating. In order to obtain a quantitative sense, the dye penetration in each experimental group was analyzed by an epifluorescence microscope and presented in terms of relative fluorescent units (RFU) in Figure 5.3. Remarkably, this figure suggests that the amount of dye diffused into the brain tissue after application of magnetic heating is over 4-fold larger than when it is not applied.

Reversible opening of the BBB by magnetic heating of MNPs requires a precise delivery of a well-controlled thermal dose into a complex biological system of the brain that is equipped with its own thermoregulatory system. While theoretical calculation of the temperature near the BBB by thermodynamic equations is possible, exact empirical readings are practically impossible. Therefore, instead of relying on thermometers, MNPs and magnetic heating parameters are adjusted based on the feedback from the quantitative analysis of diffused dye into the tissue. For example, if the dye was unable to diffuse into the tissue after 30 min of magnetic heating, we could increase the exposure time or the MNP concentration to reach BBB opening levels. We understand that this trial and error method is not an optimal solution and it should be improved for future investigations.

The accumulation of MNPs may have led to ischemic stroke, which would translate into BBB leakage [22]. However, despite evidence of accumulated MNPs as seen in TEM images shown in Figure 5.5b and c, these images do not show any sign of neuronal death or glial reactivity as observed in ischemic stroke. A recent study by Darwazeh et al. [23] suggests that mild elevation of brain temperature may have positive effects on the injured central nervous system. Regardless of ischemic occurrence, our results simply imply that the BBB leakage rate is substantially higher with magnetic heating and it is lower after recovery.

The EB dye is considered a blood-borne molecule, which is at equilibrium between bound and unbound forms. A more thorough investigation using molecular tracers of different sizes would allow us to determine what is the size of the molecule that can be delivered by this method. Other future work include assessment of the BBB permeability for longer periods of time, use of neuronal and axonal markers to ensure the safety of this protocol, as well as surface modification, synthesis and optimization of the MNPs. Conveniently, the coating of the MNPs in this study

provides an adhesive property (hydrophobic/ hydrophilic interaction) to anchor onto the surface of the endothelium. The final concentration of the MNPs in the brain is highly dependent on the exact location of the injection site, as well as the blood flow rate at the time of injection.

As shown in Figure 5.2— Camera, the MNPs are seen in the vasculature of only the Normothermia group. The MRI section of the same figure shows darker reflection for the MNPs in that group. While a multitude of factors may be at play, we speculate that the thermal energy facilitates MNP liberation from the surface of the endothelium in Hyperthermia and Recovery groups. Also, the reticuloendothelial (macrophage) clearance system (RCS) actively cleans the capillaries from the intruding MNPs (see TEM image on Fig. 5c). However, even after magnetic heating and/or the work of the RCS, some of the MNPs remain in the target location. This is evident from the images shown in Figure 5.2— MRI. In this figure, the MNPs are detected as distortions of the image because they greatly change the spin–spin relaxation rate (T2) of the surrounding water molecules in the tissue [24]. The exact quantity of the MNPs that remain in the target is yet to be investigated. Nevertheless, the images in Figure 5.5b and c suggest that the MNPs stay in the capillaries and do not cross the BBB. Conversely, in a recent *in vitro* study Bramini et al. [25] have reported significant crossing of the MNPs through the BBB. In our case however, other than a few lysosomal-like accumulations, we did not observe large accumulations inside the endothelium membrane (image not shown). This shows that different coatings, composition and size of the MNPs interact differently with the BBB.

5.10.3 Primary immune response

The complex effects of BBB opening on the brain immune system have important implications for clinical practice. In reaction to inflammation or homeostatic disturbances, microglial cells play a central role in immune responses of the brain environment. These cells present themselves as resting during local surveying of the microenvironment, and activated during an immune response. TEM images reveal the presence of these cells around the capillaries in resting state (Figure 5.4c). The morphological change of microglia from resting to activated state is largely associated with an increase in CD68 glycoprotein on the cytoplasm of the microglial cells. This marker is also expressed on various macrophages/monocyte lineage cells [26] and it is a commonly used antibody as a primary indicator of the immune response. Although we have not

yet fully verified this using all histological methods, the screening for CD68 marker showed no apparent immune response to our treatment in the brain tissue.

It is evident that once the BBB is opened, the brain is exposed to blood-derived factors from which it is normally isolated. While there are other examples where the treatments for chronic and lethal diseases may temporarily jeopardize the patient's health as a whole, for a patient with severe brain disorder such as a lethal tumour, the benefit of having much needed therapeutics cross the BBB outweighs the risks. The unfortunate sequelea of chemotherapy-induced immunosuppression that seriously increases susceptibility of the patient to harmful pathogens is one of many examples. To minimize the entry of opportunistic pathogens to the brain, the extent of BBB opening must be engineered to exact molecular weight and size of the drug of interest. Adjusting the RF field parameters, the duration of the exposure to the field, as well as surface modification of MNPs, concentration, and volume will also enhance our control on the magnitude of the BBB opening and it will minimize possible pathological risks.

5.10.4 Properties of the MNPs

In addition to being multifunctional entities that make MNPs great candidates for targeted drug delivery [4,27,28], they have been extensively studied for their magnetic heating abilities as a complementary therapy that yields maximum benefit from radiotherapy and chemotherapy [5,29]. Among various chemical compositions, iron oxide MNPs (Fe_3O_4) have been given special attention due to biodegradability and low toxicity [30,31]. To minimize direct exposure of the iron oxide core while in biological settings, MNPs are often coated with a protective polymer shell. In addition, the coating decreases the dipole–dipole interaction between individual particles and prevents undesired aggregation [32]. Our investigation showed that among commercially available particles, polymaleic acid-co-olefin (PMO)-coated MNPs have the highest thermal effect (see Supplementary Information Appendix B S1). Other properties such as particle diameter and size distribution (mono-dispersed vs. poly-dispersed) can also play an important role in MNP heating ability [33,34]. To obtain maximum efficacy from the MNPs, these parameters should be well considered.

5.10.5 Regulations for safe RF Field

Guidelines that limit the RF field parameters are set to prevent deleterious physiological responses. These responses are stimulations of peripheral and skeletal muscles, possible cardiac stimulation, arrhythmia and non-specific inductive heating of tissue. For biomedical purposes, the frequency of the field has to be higher than 50 kHz to avoid neuromuscular electrostimulation and lower than 10 MHz for appropriate penetration [35]. In addition, when an electromagnetic wave such as the RF field passes through the human body, as it collides with the tissue it declines in intensity. This decline is supported by a mathematical equation and it is further discussed in supporting information (Supplementary Information Appendix B2). We found frequencies ranging near 100 kHz suitable for proper tissue penetration and excitation of the MNPs at a target area deep in the brain. The tolerable exposure of living tissue to RF field is limited by its physiological constraints and depends on the field parameters. The ICNIRP guideline suggests a load threshold of 10 W kg^{-1} for the human head [36]. Plugging appropriate conductivity values for the human brain tissue (white matter, gray matter and skull) at 100 kHz [37], we obtained the upper limit curve for the RF field amplitude and frequency inside a cylindrical coil large enough to fit a human head (Supplementary Information Appendix B, S. 6).

5.10.6 Prospect in targeted drug delivery to the brain

Among all disorders, brain tumours are extremely lethal and incredibly invasive and despite the remarkable progress in pharmaceutical advances, the clinical translation of drug delivery to the brain faces a bottleneck. The inability to permeate through the BBB as well as lack of a localized therapy increases the cytotoxic risks of the therapeutics on normal tissue and thus hampers their efficacy. This is well apparent in the case of gliomas that account for approximately 70% of all malignant primary brain tumours and despite important advances in understanding their molecular pathogenesis, as well as in surgical resection and radiotherapy, they remain difficult to treat and the average survival length is only 12 to 15 months after diagnosis [38,39]. Therefore, highly selective permeability of BBB and limited pharmacological interventions, as well as high cytotoxicity of systemically administered therapeutics reinforces the importance of a controlled, localized and targeted remedy for brain related disorders.

Glioblastoma multiforme is the most common and invasive malignant primary brain tumour in children. With magnetic heating of MNPs that are attached to the BBB, we can evaluate the efficacy of orally administered chemotherapeutic drugs such as temozolomide on this tumour. In addition, transferrin has receptors specifically localized on the BBB and at higher concentration in and around brain tumours [40], therefore, the spatial specificity of transferrin-conjugated MNPs to open BBB at the vicinity of the tumour can be investigated. This strategy will allow us to optimize the MNP concentration required to control the BBB permeability and to use lower dosage of toxic therapeutic agents to combat the tumour.

In contrast to other forms of drug delivery mechanisms, MNPs have shown great advantages in tumour targeting [28] and treatment [41]. In fact, our team has previously displaced and tracked therapeutics that were bounded to the MNPs in the vasculature of an anesthetised animal [20]. With the help of an applied 3D driving force from the magnetic fields of the MRI, aggregates of MNPs can be propelled towards a target region such as the brain. In addition, they can be tracked using the same distortion that they create on the images of the MRI shown in Figure 5.2— MRI. In this paper, we introduced magnetic heating ability of the same MNPs to yet expand their capabilities in drug delivery. We believe that the integration of the MRI-based propelling and tracking technique, as well as the BBB opening by magnetic heating provides the start of a non-invasive localized and targeted drug delivery mechanism to the brain.

5.11 Conclusion

In this preliminary investigation, we introduced a method to transiently and locally open the BBB. It consists of the application of a regulated RF field to the locally administered MNPs in the brain. The MNPs in this configuration act as miniaturized heat sources that deliver the thermal energy uniquely to the endothelium with a higher spatial precision. We showed that large dye molecules are able to cross the BBB after application of this technique. We also showed that the BBB is able to naturally fully recover. Although the results shown here are only a proof of concept, the final goal of this research is to develop a mechanism that uses MRI and engineered MNPs to deliver therapeutics anywhere in the brain. The scientific ingenuity of the proposed technique combines simplicity, localized reversible drug delivery and accessibility throughout all regions of the brain, together with cell-specificity and apparent lack of primary immune response.

Potentially, this approach opens up a new window in search for a local drug delivery mechanism to treat various disorders including psychiatric, neurological and neurodegenerative disorders.

5.12 Acknowledgment

SUPPLEMENTARY DATA

Supplementary data to this article can be found online at Appendix B.

Microglia - Fluorescent
(CD68 LPS Positive Control)

Macrophages - Fluorescent
(CD68 Hyperthermia)

Macrophages -TEM
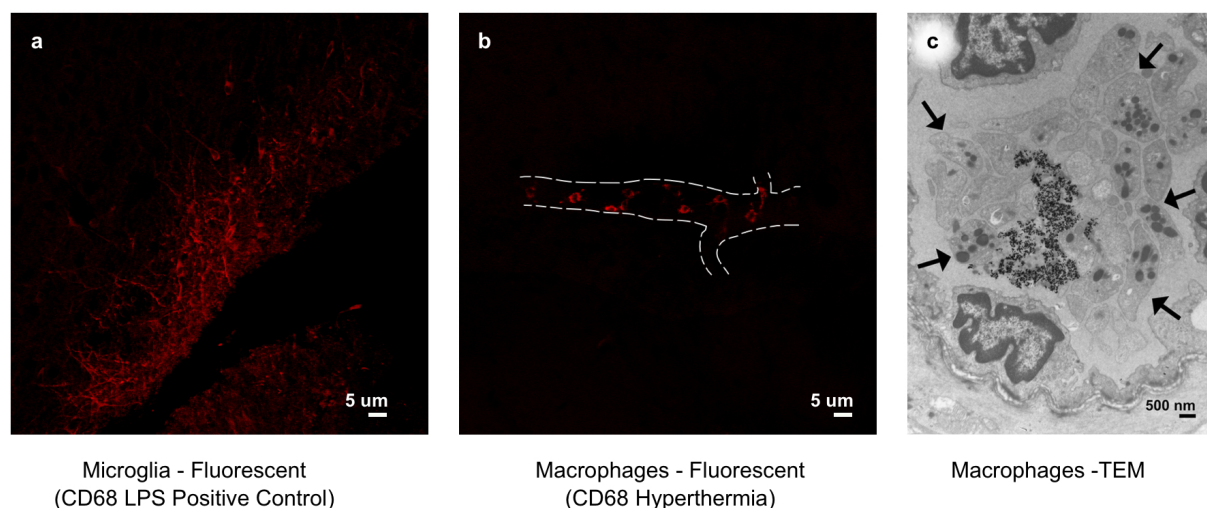
Figure 5.4: Immunohistochemistry and Microphages

a) The activated microglia is shown by the fluorescent CD68 marker on lipopolysaccharide (LPS) injected brain sample (Positive Control) at the injection site. b) There is no evidence of activated microglia in the brain parenchyma of Hyperthermia treated rats. CD68 markers are only found on macrophages inside capillaries at the MNPs injection site. The brain capillary in this image is outlined by dotted lines. c) TEM image shows that macrophages (shown by arrows) have quickly gathered to start the clean-up process of the capillary from the MNPs.
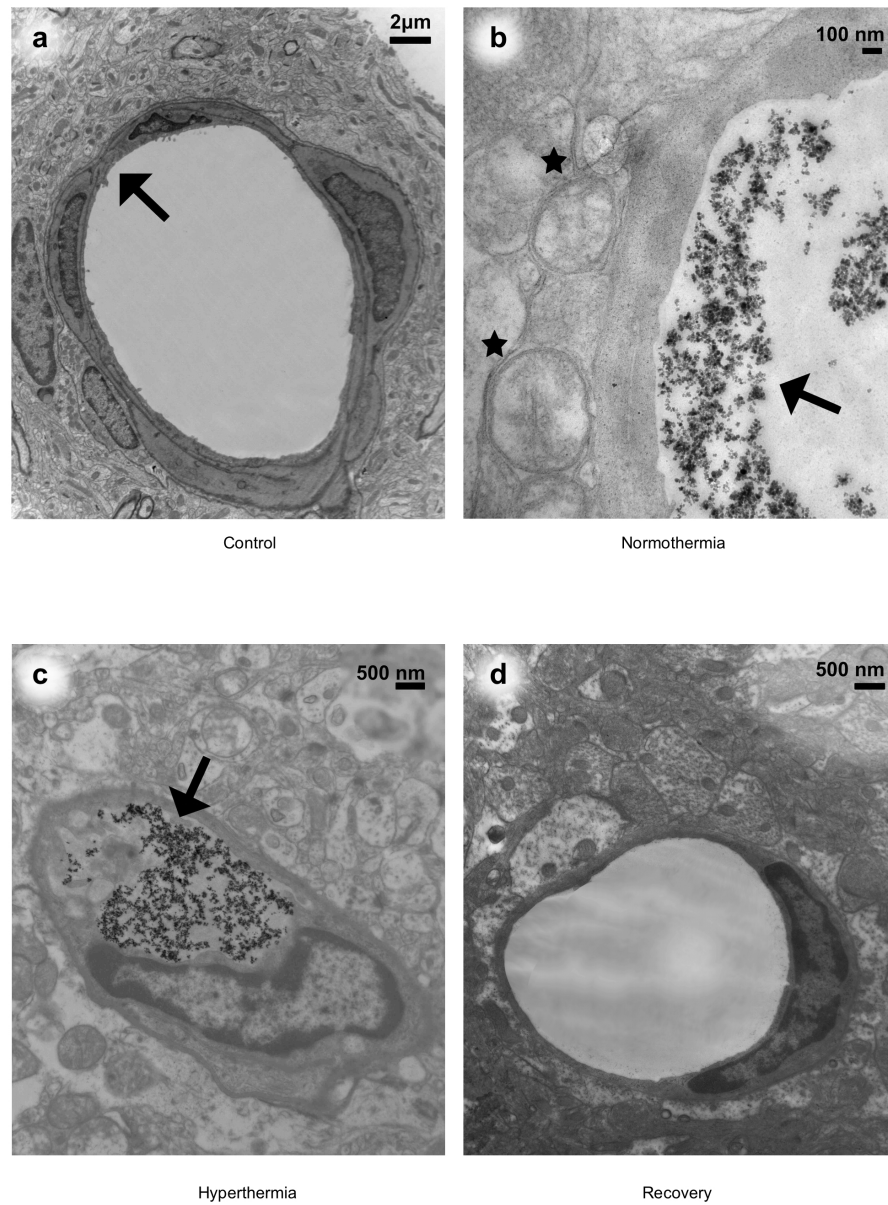
Figure 5.5: Micrographs from TEM images

a) Control: A cross section of a blood vessel in the cortex region. There was no difference between the Control and Control RF groups. The arrow indicated the location of a tight junction between two adjacent endothelial cells. b) Normothermia: A cross section of a blood vessel in the cortex region with MNPs. The MNPs are shown by an arrow inside a capillary. The black stars show the location of microglia cells around the capillary. c) Hyperthermia: After 30 min of exposure to the RF field, the MNPs are still present in the capillary. The MNPs are shown by an arrow. d) Recovery: MNPs could not be seen in the images acquired by TEM, the brain structure seemed healthy after 2 h of recovery.

CHAPTER 6   COMPLEMENTARY RESULTS: BLOOD–RETINAL BARRIER

6.1 Background

6.1.1 Blood-Retinal Barrier (BRB)

Similar to the brain microvasculature, the retinal capillaries consist of very complex inter-endothelial tight junctions that interconnect the endothelial cells (Figure 6.1). The tight junctions seal the cell interspace and form a diffusion barrier that markedly controls the flow of molecules across blood vessel walls. This mainly constitutes the BRB [73]. A functioning BRB limits the passage of therapeutic molecules into the retina of the eye including majority of acting biomolecules [74].

6.1.2 Ocular drug delivery

Drug delivery to the eye can be classified into invasive and non-invasive approaches. The invasive approach consists of an intravitreal, intracameral, posterior juxtascleral, or retrobulbar injection of the medication into the eye. These approaches often lead to acute side effects and complete or partial lost of vision. The non-invasive drug delivery approaches include application of high drug dosage through topical, oral, systemic, or sub-tenon administration [17]. Despite encouraging results presented in some preclinical models, in the case of ocular tumours these approaches have been less promising. The results vary from increased normal tissue toxicity to only small increase in patients' survival rate. That is because either the approach is extremely harsh for the ocular environment, or it is specific to a small group of drug molecules. An alternative approach from engineering's perspective is to develop a mechanism to oversee a physical opening of the BRB. This mechanism should be non-invasive, localized, transient, and it should not cause activation of the ocular immune system.

6.1.3 Localized disruption of the BRB

Our team has been investigating a strategy to deliver therapeutics anywhere in the body including the brain and the eye. More specifically, this system combines the use of non-invasive colloidal carrier systems to magnetic targeting for reversible local disruption of the BRB. The MNPs in the

colloidal carrier system are the main key advantage in this approach. The intrinsic magnetic properties of the MNPs enable their use as contrast agents in MR imaging (MRI) techniques [75]. While the MRI uses this contrast ability to track the MNPs in the vasculature, we have shown that the gradient fields of the same MRI can also propel and direct them to a biological target location [54]. Once at the target, interventions with the BRB must remain exclusively at the surface of the endothelium. This minimizes excessive damage to the complex and sensitive environment of the retina. Interestingly, MNPs can act as miniaturized heat sources that, when under the influence of the radiofrequency field, dissipate a thermal energy directly and exclusively to the monolayer lining of the vessel walls and the endothelial cells. Our recent *in vivo* data in the brain suggests that thermal energy released by magnetic nanoparticles (MNPs) upon application of alternating magnetic field can transiently and locally open the endothelial barrier (tight junction). In this investigation, we applied the same technique in the retinal tissue of rat model. To enhance localization, the MNPs were commercially coated with human transferrin (Tf-MNPs). Transferrin has receptors specifically localized on the surface of the endothelium [23] therefore this strategy will maximize the concentration of MNPs at the target barrier.
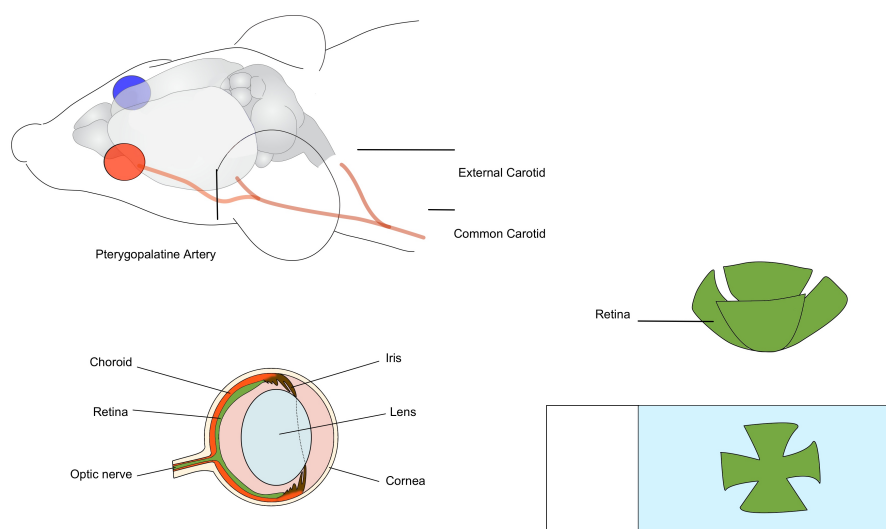
Figure 6.1: Experimental schematics

The Tf-MNPs reach the left retina through the pterygopaletine artery. Hyperthermia of these particles under the influence of an alternating magnetic field increases BRB permeability. Traces of EB dye and Na-F are detected on extracted retinas.

6.1.4 Fluorescent dye molecules

In order to evaluate barrier permeability during hyperthermia of MNPs, sodium fluorescein (Na-F) and Evans blue (EB) dye were systemically injected in the blood stream. Na-F is one of the smallest (molecular weight of 376 Da [76]), and EB is one of the largest (molecular weight of 68 kDa when bound to albumin [77]) fluorescent dye molecules that are commonly used to assess barrier leakage. In this investigation, Na-F was detected by spectrofluorometery and EB dye was counted by microscopic image analysis.

6.2 Methods and experimental procedure

6.2.1 Animal preparation

All animal procedures were performed according to the guidelines approved by the Ethics and Experimentation on Animal Committee (CDEA) of the University of Montreal. Thirty-seven pathogen-free male rats (350-450 g) were examined to confirm the efficacy of the proposed approach. During the experiments, the body temperature of the animals were kept at 37 °C by means of a homoeothermic plate.

6.2.2 Animal protocol

Animals were randomly separated into two groups of Na-F (n=25) and EB (n=12) :

Normothermia (n=8): Every animal in this group first received either 0.6 mL kg^{-1} 10% Na-F dye (n=5), or 2 mL kg^{-1} EB dye (n=3), through the tail vein after being anesthetized (2.5 % isoflurane in Oxygen). The dye was then allowed to circulate in the vasculature for at least 30 minutes. The animal was then placed supinely on a heated platform. The neck of the animal was shaved and the skin was cut about 1 cm in the middle. Then left common carotid artery (CCA), internal carotid artery (ICA), external carotid artery (ECA), and Pterygopalatine artery were carefully isolated (see in Figure 6.1). The distal portion of the ECA and the cerebral portion of the ICA were ligated with a 4-0 suture. A 32G needle (Hamilton, USA) was used to manually inject 150 μL Tf-MNPs (concentration: 25 mg mL^{-1}) into the CCA. After the injection, occluded arteries were opened and the animal was then kept alive under anesthesia for 30 minutes. Quickly after, the animal was sacrificed via intra-cardiac perfusion of 60 mL 0.9% sterile saline followed by 60 mL of 4% paraformaldehyde at a rate of 10 mL min^{-1} to wash out the dye remaining in

retinal capillaries. It was determined previously that this infusion rate does not damage the barrier [78]. Once perfusion was completed, the eyes of the animal were enucleated and conserved in 4% PFA overnight.

Hyperthermia (n=8): To see the effect of the alternating magnetic field, under anesthesia, all animals in this group received either 0.6 mL kg^{-1} 10% Na-F dye (n=5), or 2 mL kg^{-1} EB dye (n=3), through the tail vein and allowed circulating in the vasculature for 30 minutes. An average of 150 μL Tf-MNPs were then injected into the left CCA as described in Normothermia. Each animal was then placed inside the alternating magnetic field coils for 30 minutes. The animals were sacrificed after application of hyperthermia by an intra-cardiac perfusion as described for Normothermia.

Recovery (n=8): To examine the ability of BRB to recover following hyperthermic disruption, all animals in this group received a dosage average of 150 μL Tf-MNPs into the left CCA as discussed before. They were then placed inside the alternating magnetic field for 30 minutes and kept alive under anesthesia for 2 hours. After the 2 hours recovery period, the animals received either 0.6 mL kg^{-1} 10% Na-F dye (n=5), or 2 mL kg^{-1} EB dye (n=3) as described in previous groups. After 30 minutes, the animals were sacrificed via an intra-cardiac perfusion as explained before.

Control and Background (n=13): Animals in the Control group (n=8) received either 0.6 mL kg^{-1} 10% Na-F dye (n=5), or 2 mL kg^{-1} EB dye (n=3) and placed inside the alternating magnetic field for 30 minutes and sacrificed as mentioned before. Animals in the Background group (n=5) were only sacrificed via an intra-cardiac perfusion as explained before.

6.2.3 Alternating magnetic field

In this study, the alternating magnetic field was set to 7.6 kA m^{-1} at 150 kHz by a 2-kW HotShot induction-heating amplifier (Ameritherm Inc, New York). The current that conducted through a cylindrical 3-turn copper tube coil with 7 cm in diameter generated this field.

6.2.4 Spectrofluorometery analysis

All retinas with Na-F dye were extracted and placed upward in a black 96 well plate filled with 100 μL phosphate buffer solution (PBS), and sent for spectrofluorometer reading (SPECTRAmax GEMINI XS, Molecular Devices) set at excitation wavelength of 480 nm and emission wavelength of 525 nm.

Recovery

Hyperthermia

Normothermia

Control

Left Retina

Right Retina
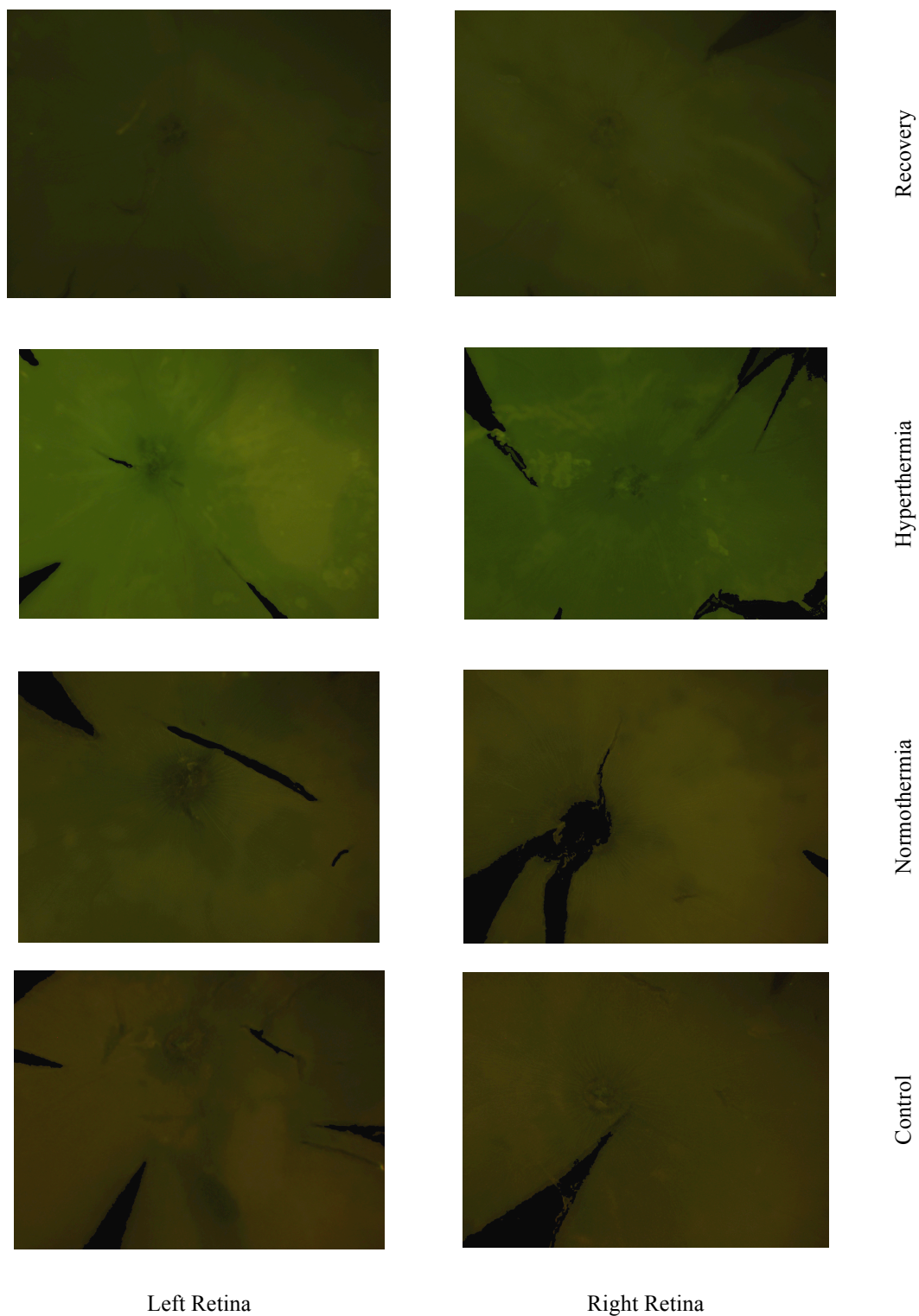
Figure 6.2: Mounted retinas are shown under the epifluorescence microscope.

The fluorescent EB dye has a higher rate of luminosity in the left retina where hyperthermia of Tf-MNPs has been applied.

6.2.5 Fluorescence microscopy

All retinas with EB dye were extracted and placed on microscopy glass slides. Sections were then mounted using a mounting medium and the EB staining was directly imaged at the center of each retina with a fluorescent microscope (Leica DM2000, Germany). EB containing samples were imaged at 4x in phase-contrast mode with a 20 ms exposure time. Images were exported for luminosity analysis in tagged image file format (TIFF). Total input was computed by summing the suprathreshold pixels within the mask. This defined the area of the retina with EB dye. The threshold was defined as the maximal intensity for 95% of pixels in the right eye. EB concentration was assessed across all groups using one-way ANOVA and Bonferroni Multiple/Post-Hoc comparisons.
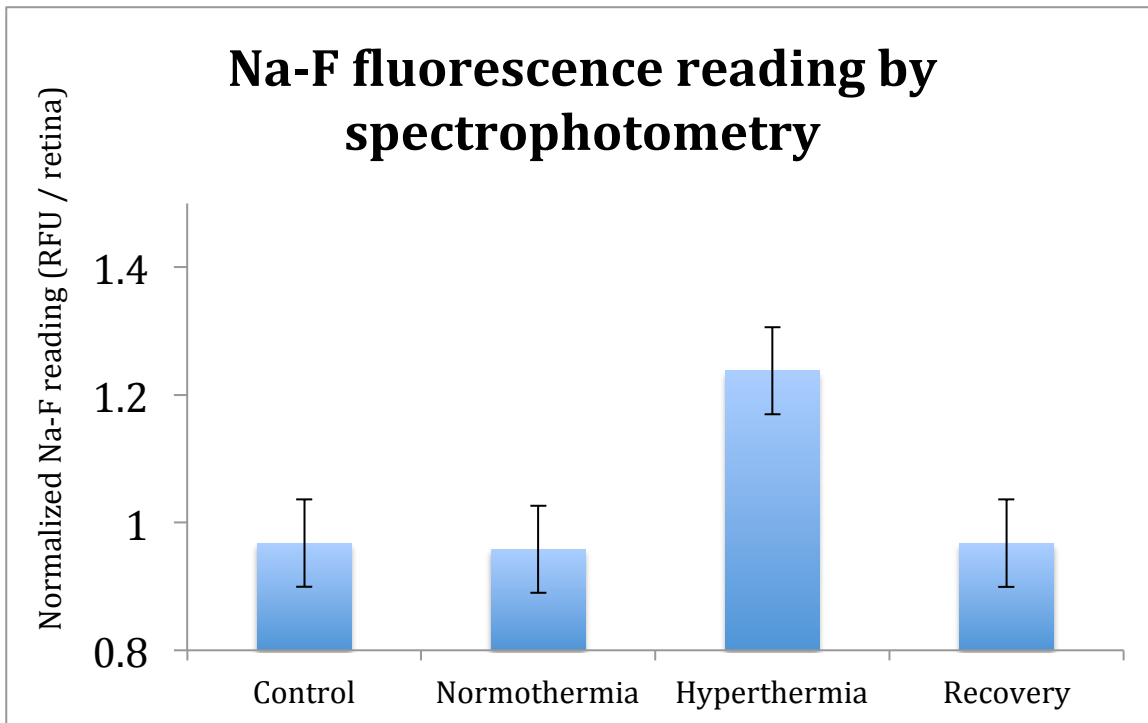
Figure 6.3 : Spectrofluorometer readings of whole retinal tissue.

The readings from the left retinas were normalized by the readings from the right retina. Then, those fall in a range between twice the standard deviation and the mean value were selected and averaged.

6.3 Results

6.3.1 BRB opening analysis by spectrofluorometery

Spectrofluorometer readings are plotted in Figure 6.3. These findings clearly indicates that hyperthermia of Tf-MNPs facilitates diffusion of small Na-F dye molecules in the retinal tissue. Note that, the readings for Control, Normothermia, and Recovery groups are very similar but there is a 22.5% increase in Na-F detection when Hyperthermia is applied.

6.3.2 BRB opening analysis by epifluorescence microscopy image analysis

Various images of mounted retinal tissue are displayed in Figure 6.2. Results from image analysis done by a MatLab ® program is shown in Figure 6.4. In this figure, each column represents the relative fluorescent units (RFU) computed from all samples (n=3) in each group. To obtain this, retinas were mounted on glass slides imaged by an epifluorescence microscope.
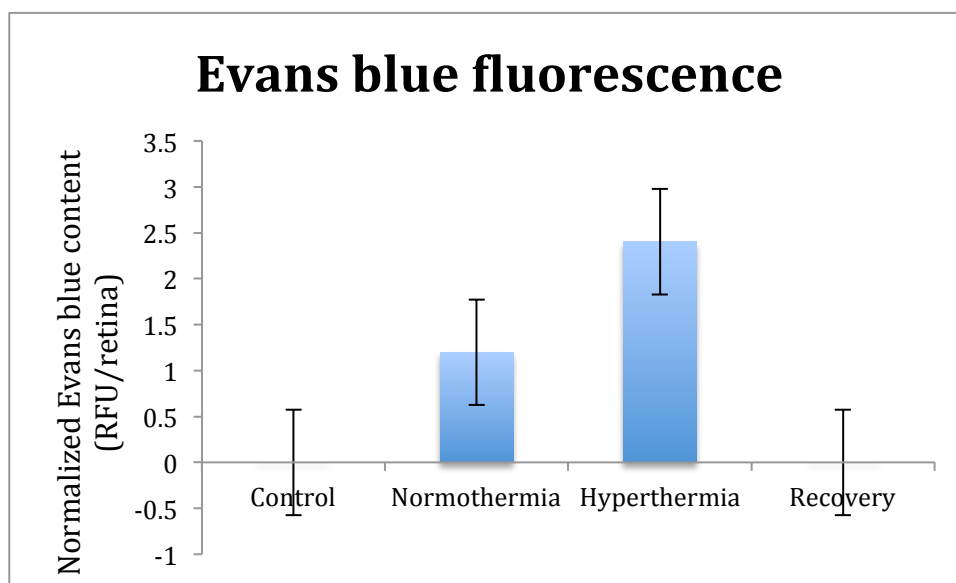
Figure 6.4: Results from microscopy image analysis for the EB dye.

In this study, the left eye was the target site and the right eye served as contralateral. The luminescence intensity thresholds for the contralateral images were computed and applied to their left counterparts. The ratio of the difference in the luminescence intensity between the two eyes with respect to the size of the retina was defined as the amount of fluorescence for each particular group. These ratios were then added and averaged.

As expected for Hyperthermia, the RFU is clearly higher than in any other group. Also, in the case of Recovery, the amount of fluorescent units counted after 2 hours of recovery period from hyperthermic disruption of the BRB is substantially lower than Hyperthermia and Normothermia.

6.4 Discussion

The BRB is a highly organized multicellular complex consisting of endothelial cells that are tightly interconnected. This barrier markedly protects neurons by controlling the passage of the molecules into the retinal tissue. By the same line of argument, therapeutic molecules are also exempt from reaching the retinal tissue. For instance, in the case of retinoblastoma, an aggressive tumour that occurs in the developing retina of children, the main reason for failure of systemic administration of chemotherapeutics and subsequent enucleation (surgical removal of the eye) is the recurrence of subretinal or vitreous seeds, and lack of drug penetration, and high toxicity of the drugs on normal cells [79]. Given the disadvantages of current remedies, a localized, safe, and reversible strategy is therefore highly desirable. This strategy will reduce systemic toxicity thereby decreasing the need for hospitalization. Furthermore, a localized therapy allows the administration of significantly higher doses of therapeutics directly to the tumour site, which enhances the biological effect, improves the tumour control, and, thus, reduces the rate of recurrence. Recently, our team was able to use hyperthermia of MNPs to locally manipulate another similarly structured barrier in the CNS [80]. In this short presentation, we used the same technique to illustrate the effect of thermal energy on the BRB. As a part of a greater objective for targeted CNS drug delivery [30], in this investigation we used Tf-MNPs to target the left retina of the anaesthetized animals. The alternating magnetic field was used to elevate local temperature of the Tf-MNPs, and the induced thermal energy allowed both small Na-F molecules and large EB molecules into the retinal tissue. It is important to note that after two hours of recovery period, the BRB did not allow small Na-F molecules to diffuse into the neural tissue. This means that regardless of the molecular weight, the BRB was able to recover from the hyperthermic disruption.

We have shown effective traversing of dye molecules across the BRB, however, a more thorough investigation using drug molecules and a tumour model would allow us to examine its performance in a therapeutic setting.

In the recent years MNPs have drawn a lot of attention for their theranostic (therapeutic and diagnostic) capabilities, therefore, our findings presented in this investigation are particularly encouraging for novel targeted drug delivery system to the eye. Evidently, hyperthermia with Tf-MNPs and alternating magnetic field has increased the permeability of the BRB for the EB and Na-F dye. The barrier can then recover from the thermal stress and regain full functionality. Today, due to the functioning barrier, drug delivery to the CNS including the eye faces a bottleneck. The present study provides preliminary evidence that hyperthermia of MNPs can open new possibilities for localized drug delivery to treat various CNS-related disorders.

CHAPTER 7   GENERAL DISCUSSION

The demanding function of the neural tissue requires an extremely stable environment. In fact, any small change in the composition of the interstitial fluid in the CNS plays a predominant role in regulating the brain microenvironment and thus neuronal activity. Therefore, the brain is conceived to protect itself from frequent fluctuations of extracellular concentration of hormones, amino acids, and potassium levels that occur after meals, exercise, or stress - as well as from toxic pathogens that may be circulating in the blood stream. This preventive defense mechanism is known as the blood-brain barrier (BBB) in the brain, and the blood-retinal barrier (BRB) in the retina. It consists mainly of tightly interconnected endothelial cells that carpet the inner surface of most blood vessels in the brain [7]. While the barrier provides a stable neuronal environment for a healthy CNS, it represents an insurmountable challenge for neuropharmacologists to combat CNS-related chronic disorders. According to Pardridge [15], more than 98% of all drug molecules are not able to cross this barrier. In the case of lethal brain neoplasm such as GBM, the tumour cells are located in the middle of the brainstem where they infiltrate amidst the nerves, making surgery practically impossible. Despite of weakened BBB in most developed tumours, the blood-tumour barrier (BTB) prevents many drugs to act upon the tumour which leads to low survival rate and poor quality of life. The BTB is a barrier that is formed between the tumour tissues and brain microvessels by highly specialized endothelial cells. In summary, during the development of the brain tumour, the cancer cells begin to invade the surrounding healthy tissue. As tumour cell clusters reach a certain volume, BBB gradually starts to collapse and the BTB begins to shape. With the deterioration of the tumour, progressive impairment of the BBB and angiogenesis, BTB becomes the main barrier to limit drug delivery. At this stage, the abnormal tumour neovasculature supports the growth and development of tumours by enhancing the permeability of the BTB. However, the cranial microenviroment and/or the tumour specificity make malignant tumours less permeable. Although the BBB is now compromised, at the proliferating tumour edge, this barrier persists with full functionality while the tissue could be well affected by the malignancy. Therefore, for an effective infiltration of the therapeutics, drugs still need to be delivered through the BBB to the surrounding tumour tissue. A recent effort presented in this doctoral thesis provides evidence for the emergence of a novel approach to overcome this problem. This technique uses MNPs in conjunction with an alternating magnetic field to transiently increase barrier permeability for drug delivery. In addition to novelty, the

findings confirm that the technique does not damage the neurovascular unit, i.e. neurons, astrocytes, etc.

A current popular strategy is called HIFU that promises localized infiltration of therapeutics across the barrier. While this technique has shown promising, it offers low spatial and temporal resolution and it propagates non-linearly over a broad region of biological structures. Other physical stimuli approaches such as microwave or electromagnetic fields are among techniques that utilize hyperthermia to elevate the homeostatic temperature of the cerebrovascular unit. While elevation of temperature may create risks to the surrounding cerebrovascular unit, it offers an increase in CNS barrier permeability through a mechanism that widens the tight junctions [33], [81]. To minimize the risks, and increase spatial and temporal resolution, MNPs-induced hyperthermia is proposed. In this technique MNPs release a thermal energy when exposed to an alternating magnetic field. The heat can dissipate to adjacent endothelial cells (tight junctions) of the CNS creating an opening in the barrier [82], [83]. There are many advantages to this technique; chief among them is that the barrier leakage appears to be entirely reversible and it is not associated with an increase in CNS immune response. Also, the intrinsic magnetic properties of the MNPs enable their use as contrast agents in MRI techniques [75]. While the MRI uses this contrast ability to track the MNPs in the vasculature, the gradient fields of the same MRI can also propel and direct them to a biological target location [5]. Therefore, MNPs can offer non-systemic delivery to spatially determined regions of the CNS using the MRN system [30]. This system provides physicians with a platform that allows targeting and delivery of medications to any specific location in the human body. In addition, MNPs induced hyperthermia is effective to target deep physiological regions. In this configuration, the alternating magnetic field parameters (field strength and frequency) are set to be compatible with human physiology and limitations of exposure to high magnetic fields. Furthermore, MNPs can be chemically engineered to specifically target the surface of the vascular endothelium by means of adhesion antibodies. For instance, transferrin has receptors specifically localized on the surface of the endothelium and at higher concentration around certain brain disorders [23]. This strategy could optimize the required MNPs concentration at the target site and lower side effects.

Previously, hyperthermia of MNPs was thoroughly investigated and among number of different commercially available coatings, PMO coated particles showed highest heating profile (Appendix B, S. 1). In this doctoral thesis, hyperthermia of PMO coated MNPs was used to deliver otherwise

impermeable fluorescent dye molecules to the CNS in a rat model. Our preliminary results show that hyperthermia induced by MNPs translates to an increase in BBB permeability towards large albumin bonded Evans blue dye molecules in the brain. In this process, TEM images revealed the endocytosis of an infinitesimal amount of MNPs by the endothelium (Figure 7.1). Nevertheless, these images indicate that most particles were not able to cross the BBB (Figure 5.5b). The polymer coating (PMO) of the MNPs may have provided an adhesive property (hydrophobic / hydrophilic interaction) to anchor onto the surface of the endothelium. Data analysis including immunohistochemistry suggests that this technique goes beyond former methods to access the CNS with higher spatial precision and advanced control without perturbing surrounding structures of the cerebrovascular unit.

In the ocular organ, transferrin conjugated MNPs were used to examine extravasation of sodium fluorescein across BRB and into the retinal tissue. Spectrofluorometery and microscopic imaging analysis strongly support the idea that hyperthermia of MNPs can transiently open BRB for penetration of therapeutic molecules into the retinal tissue.
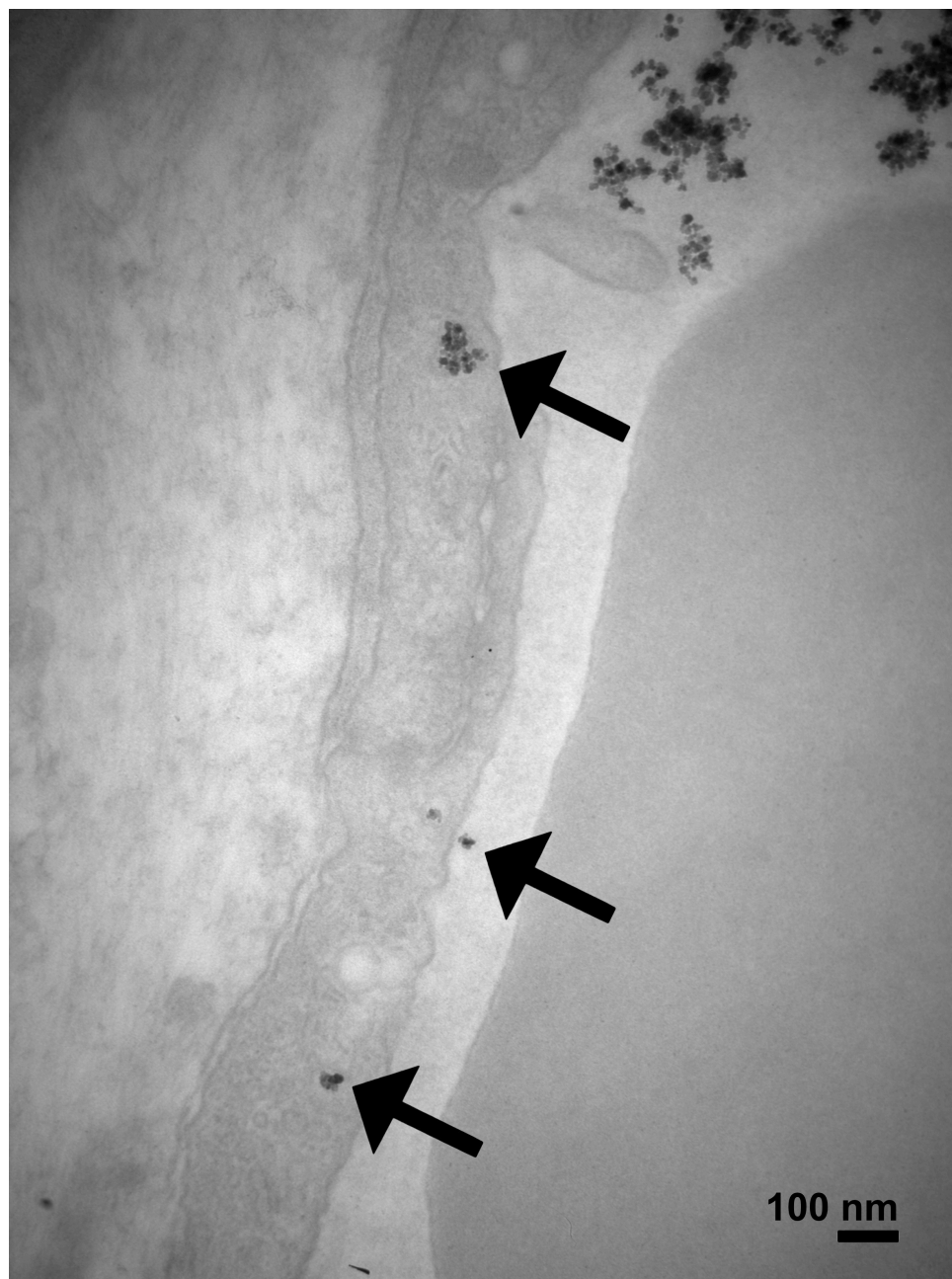
Figure 7.1: Endocytosis of MNPs by the endothelium surface

The arrows indicate few MNPs that are found in the lumen of the vessel while the rest of the MNPs on the top right corner could not penetrate across the BBB

It is evident that once the barrier is opened, the CNS is exposed to opportunistic pathogens from which it is normally isolated. This is in fact a major obstacle. To address this alarming problem, barrier permeability must be engineered to molecular weight and size of the drug of interest. Adjusting the alternating magnetic field parameters, the duration of the exposure to the field, as

well as surface modification of MNPs, concentration, volume, and administration of antibiotics to the patient just before the intervention in a sterile environment could minimize possible pathological risks. The faith and the risk of MNPs in the blood stream especially in the brain is also among other alerting issues that needs to be well investigated. However, for patients with chronic and lethal CNS-related diseases the benefits associated with this technique seems to outweigh the risks. The collective assembly of hyperthermia of MNPs along with the MRN system makes MNPs a principal component of the proposed non-invasive targeted drug delivery mechanism to the CNS. Notably, when constructing the overall system, the limitations that the large one directional magnetic field of the MRI may introduce to the relatively smaller alternating magnetic field amplitude of the hyperthermia system (for example the distance between the MRI and the hyperthermia generator) should be well contemplated. Needless to say, it is clear that the proposed form of hyperthermia opens a door to new clinical trials involving otherwise very efficient anticancer treatments which do not readily cross the BBB and the BRB. The long-term goal is the development of a fully operational targeted drug delivery platform for the retina and the brain. By assessing the therapeutic efficacy of the hyperthermia technique in animal models, we have gotten closer to a great expectation for patients affected by CNS-related disorders.

CHAPTER 8   CONCLUSION

The large number of individuals suffering from chronic brain diseases underlies the enormous potential growth of the neuro-pharmaceutical market. However, due to the presence of an intact endothelial barrier (tight junctions), most drugs do not enter the CNS following systemic administration. The present thesis has introduced localized thermal energy as a potential remedy to deliver therapeutics to treat various CNS disorders. In this technique, MNPs can act as miniaturized heat sources that, when under the influence of the alternating magnetic field, dissipate a thermal energy directly and exclusively to the ambient endothelial cells.

After successfully propelling therapeutic agents encapsulated in magnetic micro-carriers [84] to a specific biological location in animal model by the gradient magnetic field of a modified clinical MRI scanner (MRN system) [30], we aimed to perform local drug delivery to the CNS. To achieve localized drug delivery and increase efficacy, this project advances the theme that the therapeutic agents must be administered to the CNS by means no more invasive than an intravenous injection followed by remote propulsion, controlled tracking, and on-command actuation. Clearly, more efforts are required to marry MRN with hyperthermia of MNPs before it becomes clinically viable, however, the work of this thesis opens a new window in search for a local drug delivery mechanism to treat various neurological disorders.

BIBLIOGRAPHY

[1]   J. A. Aarli, T. Dua, A. Janca, and A. Muscetta, "WHO | Neurological Disorders: Public Health Challenges," in *WHO*, Switzerland, pp. 27–39.

[2]   "Brain Tumour Facts," 12-Jun-2015. [Online]. Available: http://www.braintumour.ca/2494/brain-tumour-facts.

[3]   "Central Brain Tumor Registry of the United States. 2007-2008 primary brain tumors in the United States: Statistical report.," *CBTRUS*. [Online]. Available: http://www.cbtrus.org/reports/2007-2008/2007report.pdf.

[4]   Y. Persidsky, M. Stins, D. Way, M. H. Witte, M. Weinand, K. S. Kim, P. Bock, H. E. Gendelman, and M. Fiala, "A model for monocyte migration through the blood-brain barrier during HIV-1 encephalitis.," *J. Immunol.*, vol. 158, no. 7, pp. 3499–3510, Apr. 1997.

[5]   P. Pouponneau, J.-C. Leroux, G. Soulez, L. Gaboury, and S. Martel, "Co-encapsulation of magnetic nanoparticles and doxorubicin into biodegradable microcarriers for deep tissue targeting by vascular MRI navigation," *Biomaterials*, vol. 32, no. 13, pp. 3481–3486, May 2011.

[6]   S. N. Tabatabaei Shafie, "Evaluation of Hyperthermia Using Magnetic Nanoparticles and Alternating Magnetic Field," masters, École Polytechnique de Montréal, 2010.

[7]   E. Kandel, J. Schwartz, and T. Jessell, *Principles of Neural Science*, 4 edition. New York: McGraw-Hill Medical, 2000.

[8]   H. Fischer, R. Gottschlich, and A. Seelig, "Blood-brain barrier permeation: molecular parameters governing passive diffusion," *J. Membr. Biol.*, vol. 165, no. 3, pp. 201–211, Oct. 1998.

[9]   A. Béduneau, P. Saulnier, and J.-P. Benoit, "Active targeting of brain tumors using nanocarriers," *Biomaterials*, vol. 28, no. 33, pp. 4947–4967, Nov. 2007.

[10]   W. M. Pardridge, *Brain Drug Targeting: The Future of Brain Drug Development*. Cambridge University Press, 2001.

[11]   N. J. Abbott, L. Rönnbäck, and E. Hansson, "Astrocyte-endothelial interactions at the blood-brain barrier," *Nat. Rev. Neurosci.*, vol. 7, no. 1, pp. 41–53, Jan. 2006.

[12]   K. Nagpal, S. K. Singh, and D. N. Mishra, "Drug targeting to brain: a systematic approach to study the factors, parameters and approaches for prediction of permeability of drugs across BBB," *Expert Opin. Drug Deliv.*, vol. 10, no. 7, pp. 927–955, Jul. 2013.

[13]   W. M. Pardridge, "Drug and gene targeting to the brain via blood–brain barrier receptor-mediated transport systems," *Int. Congr. Ser.*, vol. 1277, pp. 49–62, Apr. 2005.

[14]   K. E. Schlageter, P. Molnar, G. D. Lapin, and D. R. Groothuis, "Microvessel Organization and Structure in Experimental Brain Tumors: Microvessel Populations with Distinctive Structural and Functional Properties," *Microvasc. Res.*, vol. 58, no. 3, pp. 312–328, Nov. 1999.

[15]   W. M. Pardridge, "Drug transport across the blood–brain barrier," *J. Cereb. Blood Flow Metab.*, vol. 32, no. 11, pp. 1959–1972, Nov. 2012.

[16]   R. J. Boado, E. K.-W. Hui, J. Z. Lu, R. K. Sumbria, and W. M. Pardridge, "Blood-Brain Barrier Molecular Trojan Horse Enables Imaging of Brain Uptake of Radioiodinated Recombinant Protein in the Rhesus Monkey," *Bioconjug. Chem.*, vol. 24, no. 10, pp. 1741–1749, Oct. 2013.

[17]   R. Gaudana, H. K. Ananthula, A. Parenky, and A. K. Mitra, "Ocular Drug Delivery," *AAPS J.*, vol. 12, no. 3, pp. 348–360, May 2010.

[18]   M. Mak, L. Fung, J. F. Strasser, and W. M. Saltzman, "Distribution of drugs following controlled delivery to the brain interstitium," *J. Neurooncol.*, vol. 26, no. 2, pp. 91–102, Nov. 1995.

[19]   P. R. Lockman, R. J. Mumper, M. A. Khan, and D. D. Allen, "Nanoparticle technology for drug delivery across the blood-brain barrier," *Drug Dev. Ind. Pharm.*, vol. 28, no. 1, pp. 1–13, Jan. 2002.

[20]   L. Fenart, A. Casanova, B. Dehouck, C. Duhem, S. Slupek, R. Cecchelli, and D. Betbeder, "Evaluation of effect of charge and lipid coating on ability of 60-nm nanoparticles to cross an in vitro model of the blood-brain barrier," *J. Pharmacol. Exp. Ther.*, vol. 291, no. 3, pp. 1017–1022, Dec. 1999.

[21]   W. M. Pardridge, "Molecular Trojan horses for blood-brain barrier drug delivery," *Curr. Opin. Pharmacol.*, vol. 6, no. 5, pp. 494–500, Oct. 2006.

[22]   S. I. Rapoport, "Advances in osmotic opening of the blood-brain barrier to enhance CNS chemotherapy," *Expert Opin. Investig. Drugs*, vol. 10, no. 10, pp. 1809–1818, Oct. 2001.

[23]   S. Wang, O. O. Olumolade, T. Sun, G. Samiotaki, and E. E. Konofagou, "Noninvasive, neuron-specific gene therapy can be facilitated by focused ultrasound and recombinant adeno-associated virus," *Gene Ther.*, vol. 22, no. 1, pp. 104–110, Jan. 2015.

[24]   K. Hynynen, N. McDannold, N. Vykhodtseva, and F. A. Jolesz, "Noninvasive MR Imaging–guided Focal Opening of the Blood-Brain Barrier in Rabbits," *Radiology*, vol. 220, no. 3, pp. 640–646, Sep. 2001.

[25]   N. Sheikov, N. McDannold, S. Sharma, and K. Hynynen, "Effect of Focused Ultrasound Applied With an Ultrasound Contrast Agent on the Tight Junctional Integrity of the Brain Microvascular Endothelium," *Ultrasound Med. Biol.*, vol. 34, no. 7, pp. 1093–1104, Jul. 2008.

[26]   P. Prentice, A. Cuschieri, K. Dholakia, M. Prausnitz, and P. Campbell, "Membrane disruption by optically controlled microbubble cavitation," *Nat. Phys.*, vol. 1, no. 2, pp. 107–110, Nov. 2005.

[27]   C.-H. Fan, C.-Y. Ting, H.-J. Lin, C.-H. Wang, H.-L. Liu, T.-C. Yen, and C.-K. Yeh, "SPIO-conjugated, doxorubicin-loaded microbubbles for concurrent MRI and focused-ultrasound enhanced brain-tumor drug delivery," *Biomaterials*, vol. 34, no. 14, pp. 3706–3715, May 2013.

[28]   M. Fujii, K. Sakamoto, Y. Toda, A. Negishi, and H. Kanai, "Study of the cause of the temperature rise at the muscle-bone interface during ultrasound hyperthermia," *IEEE Trans. Biomed. Eng.*, vol. 46, no. 5, pp. 494–504, May 1999.

[29]   S. D. Kong, J. Lee, S. Ramachandran, B. P. Eliceiri, V. I. Shubayev, R. Lal, and S. Jin, "Magnetic targeting of nanoparticles across the intact blood-brain barrier," *J. Control. Release Off. J. Control. Release Soc.*, vol. 164, no. 1, pp. 49–57, Nov. 2012.

[30]   A. Bigot, C. Tremblay, G. Soulez, and S. Martel, "Magnetic Resonance Navigation of a Bead Inside a Three-Bifurcation PMMA Phantom Using an Imaging Gradient Coil Insert," *IEEE Trans. Robot.*, vol. 30, no. 3, pp. 719–727, Jun. 2014.

[31]   P. Wust, B. Hildebrandt, G. Sreenivasa, B. Rau, J. Gellermann, H. Riess, R. Felix, and P. M. Schlag, "Hyperthermia in combined treatment of cancer," *Lancet Oncol.*, vol. 3, no. 8, pp. 487–497, Aug. 2002.

[32]   Y. Ohmoto, H. Fujisawa, T. Ishikawa, H. Koizumi, T. Matsuda, and H. Ito, "Sequential changes in cerebral blood flow, early neuropathological consequences and blood-brain barrier disruption following radiofrequency-induced localized hyperthermia in the rat," *Int. J. Hyperthermia*, vol. 12, no. 3, pp. 321–334, Jan. 1996.

[33]   E. Moriyama, M. Salcman, and R. D. Broadwell, "Blood-brain barrier alteration after microwave-induced hyperthermia is purely a thermal effect: I. Temperature and power measurements," *Surg. Neurol.*, vol. 35, no. 3, pp. 177–182, Mar. 1991.

[34]   J. Friedl, E. Turner, and H. R. Alexander, "Augmentation of endothelial cell monolayer permeability by hyperthermia but not tumor necrosis factor: evidence for disruption of vascular integrity via VE-cadherin down-regulation," *Int. J. Oncol.*, vol. 23, no. 3, pp. 611–616, Sep. 2003.

[35]   C. W. Song, "Effect of local hyperthermia on blood flow and microenvironment: a review," *Cancer Res.*, vol. 44, no. 10 Suppl, p. 4721s–4730s, Oct. 1984.

[36]   R. R. Shivers and J. A. Wijsman, "Blood-brain barrier permeability during hyperthermia," *Prog. Brain Res.*, vol. 115, pp. 413–424, 1998.

[37]   A. G. Macdonald, "The homeoviscous theory of adaptation applied to excitable membranes: a critical evaluation," *Biochim. Biophys. Acta*, vol. 1031, no. 3, pp. 291–310, Oct. 1990.

[38]   G. P. Raaphorst, J. Mao, and C. E. Ng, "Thermotolerance in human glioma cells," *Int. J. Hyperth. Off. J. Eur. Soc. Hyperthermic Oncol. North Am. Hyperth. Group*, vol. 11, no. 4, pp. 523–529, Aug. 1995.

[39]   V. V. Jeliazkova-Mecheva, W. C. Hymer, N. C. Nicholas, and D. J. Bobilya, "Brief heat shock affects the permeability and thermotolerance of an in vitro blood-brain barrier model of porcine brain microvascular endothelial cells," *Microvasc. Res.*, vol. 71, no. 2, pp. 108–114, Mar. 2006.

[40]   H. S. Sharma, J. A. Duncan, and C. E. Johanson, "Whole-body hyperthermia in the rat disrupts the blood-cerebrospinal fluid barrier and induces brain edema," in *Brain Edema XIII*, J. T. Hoff, R. F. Keep, G. Xi, and Y. Hua, Eds. Springer Vienna, 2006, pp. 426–431.

[41]   A. H. Mesiwala, L. Farrell, H. J. Wenzel, D. L. Silbergeld, L. A. Crum, H. R. Winn, and P. D. Mourad, "High-intensity focused ultrasound selectively disrupts the blood-brain barrier in vivo," *Ultrasound Med. Biol.*, vol. 28, no. 3, pp. 389–400, Mar. 2002.

[42]   H. Masuda, A. Hirata, H. Kawai, K. Wake, S. Watanabe, T. Arima, F. Poulletier de Gannes, I. Lagroye, and B. Veyret, "Local exposure of the rat cortex to radiofrequency electromagnetic fields increases local cerebral blood flow along with temperature," *J. Appl. Physiol. Bethesda Md 1985*, vol. 110, no. 1, pp. 142–148, Jan. 2011.

[43]   J. C. Lin, P. M. K. Yuan, and D. T. Jung, "Enhancement of anticancer drug delivery to the brain by microwave induced hyperthermia," *Bioelectrochem. Bioenerg.*, vol. 47, no. 2, pp. 259–264, Dec. 1998.

[44]   L. Recht, C. O. Torres, T. W. Smith, V. Raso, and T. W. Griffin, "Transferrin receptor in normal and neoplastic brain tissue: implications for brain-tumor immunotherapy," *J. Neurosurg.*, vol. 72, no. 6, pp. 941–945, Jun. 1990.

[45]   B. D. Cullity and C. D. Graham, *Introduction to Magnetic Materials*, 2 edition. Hoboken, N.J: Wiley-IEEE Press, 2008.

[46]   L. A. Harris, "Polymer Stabilized Magnetite Nanoparticles and Poly(propylene oxide) Modified Styrene-Dimethacrylate Networks," 15-May-2002. [Online]. Available: http://scholar.lib.vt.edu/theses/available/etd-05052002-231800/. [Accessed: 13-Jun-2015].

[47]   D. C. Jiles, *Introduction to Magnetism and Magnetic Materials, Second Edition*, 2 edition. London u.a: CRC Press, 1998.

[48]   E. Duguet, S. Vasseur, S. Mornet, G. Goglio, A. Demourgues, J. Portier, F. Grasset, P. Veverka, and E. Pollert, "Towards a versatile platform based on magnetic nanoparticles for in vivo applications," *Bull. Mater. Sci.*, vol. 29, no. 6, pp. 581–586, Nov. 2006.

[49]   C.-R. Lin, R.-K. Chiang, J.-S. Wang, and T.-W. Sung, "Magnetic properties of monodisperse iron oxide nanoparticles," *J. Appl. Phys.*, vol. 99, no. 8, p. 08N710, Apr. 2006.

[50]   E. C. Stoner and E. P. Wohlfarth, "A Mechanism of Magnetic Hysteresis in Heterogeneous Alloys," *Philos. Trans. R. Soc. Lond. Math. Phys. Eng. Sci.*, vol. 240, no. 826, pp. 599–642, May 1948.

[51]   M. K. Yoo, I. Y. Kim, E. M. Kim, H.-J. Jeong, C.-M. Lee, Y. Y. Jeong, T. Akaike, and C. S. Cho, "Superparamagnetic Iron Oxide Nanoparticles Coated with Galactose-Carrying Polymer for Hepatocyte Targeting," *J. Biomed. Biotechnol.*, vol. 2007, 2007.

[52]   W. F. Brown, "Thermal Fluctuations of a Single-Domain Particle," *Phys. Rev.*, vol. 130, no. 5, pp. 1677–1686, Jun. 1963.

[53]   D. Weller and A. Moser, "Thermal effect limits in ultrahigh-density magnetic recording," *IEEE Trans. Magn.*, vol. 35, no. 6, pp. 4423–4439, Nov. 1999.

[54]   B. Fischer, B. Huke, M. Lücke, and R. Hempelmann, "Brownian relaxation of magnetic colloids," *J. Magn. Magn. Mater.*, vol. 289, pp. 74–77, Mar. 2005.

[55]   R. E. Rosensweig, "Heating magnetic fluid with alternating magnetic field," *J. Magn. Magn. Mater.*, vol. 252, pp. 370–374, Nov. 2002.

[56]   M. Lévy, C. Wilhelm, J.-M. Siaugue, O. Horner, J.-C. Bacri, and F. Gazeau, "Magnetically induced hyperthermia: size-dependent heating power of γ-Fe(2)O(3) nanoparticles," *J. Phys. Condens. Matter Inst. Phys. J.*, vol. 20, no. 20, p. 204133, May 2008.

[57]   "Electromagnetic Theory : Adams Stratton Julius. : Free Download & Streaming," *Internet Archive*. [Online]. Available: https://archive.org/details/electromagnetict031016mbp. [Accessed: 13-Jun-2015].

[58]   T. A. Moore and J. a. C. Bland, "Mesofrequency dynamic hysteresis in thin ferromagnetic films," *J. Phys. Condens. Matter*, vol. 16, no. 46, p. R1369, Nov. 2004.

[59]   L.-Y. Zhang, H.-C. Gu, and X.-M. Wang, "Magnetite ferrofluid with high specific absorption rate for application in hyperthermia," *J. Magn. Magn. Mater.*, vol. 311, no. 1, pp. 228–233, Apr. 2007.

[60]   "Guidelines for limiting exposure to time-varying electric, magnetic, and electromagnetic fields (up to 300 GHz). International Commission on Non-Ionizing Radiation Protection," *Health Phys.*, vol. 74, no. 4, pp. 494–522, Apr. 1998.

[61]   Q. A. Pankhurst, J. Connolly, S. K. Jones, and J. Dobson, "Applications of magnetic nanoparticles in biomedicine," *J. Phys. Appl. Phys.*, vol. 36, no. 13, p. R167, Jul. 2003.

[62]   K. Okawa, M. Sekine, M. Maeda, M. Tada, M. Abe, N. Matsushita, K. Nishio, and H. Handa, "Heating ability of magnetite nanobeads with various sizes for magnetic hyperthermia at 120kHz, a noninvasive frequency," *J. Appl. Phys.*, vol. 99, no. 8, p. 08H102, Apr. 2006.

[63]   M. Johannsen, U. Gneveckow, L. Eckelt, A. Feussner, N. Waldöfner, R. Scholz, S. Deger, P. Wust, S. A. Loening, and A. Jordan, "Clinical hyperthermia of prostate cancer using magnetic nanoparticles: presentation of a new interstitial technique," *Int. J. Hyperth. Off. J. Eur. Soc. Hyperthermic Oncol. North Am. Hyperth. Group*, vol. 21, no. 7, pp. 637–647, Nov. 2005.

[64]   R. Hergt, W. Andra, C. G. d' Ambly, I. Hilger, W. A. Kaiser, U. Richter, and H.-G. Schmidt, "Physical limits of hyperthermia using magnetite fine particles," *IEEE Trans. Magn.*, vol. 34, no. 5, pp. 3745–3754, Sep. 1998.

[65]   R. Hergt and S. Dutz, "Magnetic particle hyperthermia—biophysical limitations of a visionary tumour therapy," *J. Magn. Magn. Mater.*, vol. 311, no. 1, pp. 187–192, Apr. 2007.

[66]   C. N. Marin, I. Malaescu, and A. Ercuta, "The dependence of the effective anisotropy constant on particle concentration within ferrofluids, measured by magnetic resonance," *J. Phys. Appl. Phys.*, vol. 34, no. 10, pp. 1466–1469, May 2001.

[67]   W. Prentice, *Principles of Athletic Training: A Competency-Based Approach*, 15 edition. New York, NY: McGraw-Hill Education, 2013.

[68]   A. Jordan, P. Wust, H. Fähling, W. John, A. Hinz, and R. Felix, "Inductive heating of ferrimagnetic particles and magnetic fluids: physical evaluation of their potential for hyperthermia," *Int. J. Hyperth. Off. J. Eur. Soc. Hyperthermic Oncol. North Am. Hyperth. Group*, vol. 9, no. 1, pp. 51–68, Feb. 1993.

[69]   W. J. Atkinson, I. A. Brezovich, and D. P. Chakraborty, "Usable Frequencies in Hyperthermia with Thermal Seeds," *IEEE Trans. Biomed. Eng.*, vol. BME-31, no. 1, pp. 70–75, Jan. 1984.

[70]   *Handbook of Biological Effects of Electromagnetic Fields, Third Edition - 2 Volume Set*. .

[71]   S. Dutz, R. Hergt, J. Mürbe, R. Müller, M. Zeisberger, W. Andrä, J. Töpfer, and M. E. Bellemann, "Hysteresis losses of magnetic nanoparticle powders in the single domain size range," *J. Magn. Magn. Mater.*, vol. 308, no. 2, pp. 305–312, Jan. 2007.

[72]   R. A. Freitas, *Nanomedicine, Volume I: Basic Capabilities*, 1 edition. Austin, TX: CRC Press, 1999.

[73]   *Advances in Experimental Medicine and Biology*.

[74]   S. Nag, Ed., *The Blood-Brain and Other Neural Barriers*, vol. 686. Totowa, NJ: Humana Press, 2011.

[75]   M. M. Yallapu, S. F. Othman, E. T. Curtis, B. K. Gupta, M. Jaggi, and S. C. Chauhan, "Multi-functional magnetic nanoparticles for magnetic resonance imaging and cancer therapy," *Biomaterials*, vol. 32, no. 7, pp. 1890–1905, Mar. 2011.

[76]   L. Shi, M. Zeng, Y. Sun, and B. M. Fu, "Quantification of blood-brain barrier solute permeability and brain transport by multiphoton microscopy," *J. Biomech. Eng.*, vol. 136, no. 3, p. 031005, Mar. 2014.

[77]   A. Hoffmann, J. Bredno, M. Wendland, N. Derugin, P. Ohara, and M. Wintermark, "High and Low Molecular Weight Fluorescein Isothiocyanate (FITC)-Dextrans to Assess Blood-Brain Barrier Disruption: Technical Considerations," *Transl. Stroke Res.*, vol. 2, no. 1, pp. 106–111, Mar. 2011.

[78]   T. L. Davidson, A. Monnot, A. U. Neal, A. A. Martin, J. J. Horton, and W. Zheng, "The Effects of a High-energy Diet on Hippocampal-dependent Discrimination Performance and Blood-brain Barrier Integrity Differ for Diet-induced Obese and Diet-Resistant Rats," *Physiol. Behav.*, vol. 107, no. 1, pp. 26–33, Aug. 2012.

[79]   M. Zanaty, G. Barros, N. Chalouhi, R. M. Starke, P. Manasseh, S. I. Tjoumakaris, C. L. Shields, D. Hasan, K. Bulsara, R. H. Rosenwasser, and P. Jabbour, "Update on Intra-Arterial Chemotherapy for Retinoblastoma," *Sci. World J.*, vol. 2014, p. e869604, Oct. 2014.

[80]   S. N. Tabatabaei, H. Girouard, A.-S. Carret, and S. Martel, "Remote control of the permeability of the blood-brain barrier by magnetic heating of nanoparticles: A proof of concept for brain drug delivery," *J. Control. Release Off. J. Control. Release Soc.*, vol. 206, pp. 49–57, May 2015.

[81]   L.-B. Qiu, G.-R. Ding, K.-C. Li, X.-W. Wang, Y. Zhou, Y.-C. Zhou, Y.-R. Li, and G.-Z. Guo, "The role of protein kinase C in the opening of blood-brain barrier induced by electromagnetic pulse," *Toxicology*, vol. 273, no. 1–3, pp. 29–34, Jun. 2010.

[82]   E. A. Kiyatkin and H. S. Sharma, "Permeability of the blood-brain barrier depends on brain temperature," *Neuroscience*, vol. 161, no. 3, pp. 926–939, Jul. 2009.

[83]   K. Dokladny, P. L. Moseley, and T. Y. Ma, "Physiologically relevant increase in temperature causes an increase in intestinal epithelial tight junction permeability," *Am. J. Physiol. Gastrointest. Liver Physiol.*, vol. 290, no. 2, pp. G204–212, Feb. 2006.

[84]   P. Pouponneau, J.-C. Leroux, and S. Martel, "Magnetic nanoparticles encapsulated into biodegradable microparticles steered with an upgraded magnetic resonance imaging system for tumor chemoembolization," *Biomaterials*, vol. 30, no. 31, pp. 6327–6332, Oct. 2009.

Reference – Article 1

[1]   W. M. Pardridge, "Blood-brain barrier drug targeting: the future of brain drug development," Molecular Interventions, vol. 3, pp. 90-105, March 1, 2003 2003.

[2]   P. Pouponneau, J.-C. Leroux, and S. Martel, "Magnetic nanoparticles encapsulated into biodegradable microparticles steered with an upgraded magnetic resonance imaging system for tumor chemoembolization," Biomaterials, vol. 30, pp. 6327-6332, 2009.

[3]   P. Pouponneau, J.-C. Leroux, G. Soulez, L. Gaboury, and S. Martel, "Co-encapsulation of magnetic nanoparticles and doxorubicin into biodegradable microcarriers for deep tissue targeting by vascular MRI navigation," Biomaterials, vol. In Press, Corrected Proof, 2011.

[4]   E. Moriyama, M. Salcman, and R. D. Broadwell, "Blood-brain barrier alteration after microwave-induced hyperthermia is purely a thermal effect: I. Temperature and power measurements," Surgical Neurology, vol. 35, pp. 177-182, 1991.

[5]   H. S. Sharma, J. A. Duncan, and C. E. Johanson, "Whole-body hyperthermia in the rat disrupts the blood-cerebrospinal fluid barrier and induces brain edema," in Brain Edema XIII. vol. 96, J. T. Hoff, R. F. Keep, G. Xi, and Y. Hua, Eds., ed: Springer Vienna, 2006, pp. 426-431.

[6]   J. C. Lin, P. M. K. Yuan, and D. T. Jung, "Enhancement of anticancer drug delivery to the brain by microwave induced hyperthermia," Bioelectrochemistry and Bioenergetics, vol. 47, pp. 259-264, 1998.

[7]   H. Masuda, A. Hirata, H. Kawai, K. Wake, S. Watanabe, T. Arima, F. Poulletier de Gannes, I. Lagroye, and B. Veyret, "Local exposure of the rat cortex to radiofrequency electromagnetic fields increases local cerebral blood flow along with temperature," Journal of Applied Physiology, vol. 110, pp. 142-148, 2011.

[8]   P. Wust, B. Hildebrandt, G. Sreenivasa, B. Rau, J. Gellermann, H. Riess, R. Felix, and P. M. Schlag, "Hyperthermia in combined treatment of cancer," The Lancet Oncology, vol. 3, pp. 487-497, 2002.

[9]   Q. A. Pankhurst, J. Connolly, S. K. Jones, and J. Dobson, "Applications of magnetic nanoparticles in biomedicine," Journal of Physics D: Applied Physics, vol. 36, pp. R167-R181, 2003.

[10]   E. R. Kandel, J. H. Schwartz, and T. M. Jessell, Principles of Neural Science, 4th ed.: McGraw-Hill, 2000.

[11]   H. Fischer, R. Gottschlich, and A. Seelig, "Blood-Brain Barrier Permeation: Molecular Parameters Governing Passive Diffusion," Journal of Membrane Biology, vol. 165, pp. 201-211, 1998.

[12]   A. BÈduneau, P. Saulnier, and J.-P. Benoit, "Active targeting of brain tumors using nanocarriers," Biomaterials, vol. 28, pp. 4947-4967, 2007.

[13]   W. M. Pardridge, Brain drug targeting. United Kingdom: Cambridge University Press, 2001.

[14]   W. M. Pardridge, "Drug and gene targeting to the brain via blood-brain barrier receptor-mediated transport systems," International Congress Series, vol. 1277, pp. 49-62, 2005.

[15]   N. J. Abbott, L. Ronnback, and E. Hansson, "Astrocyte-endothelial interactions at the blood-brain barrier," Nat Rev Neurosci, vol. 7, pp. 41-53, 2006.

[16]   K. E. Schlageter, P. Molnar, G. D. Lapin, and D. R. Groothuis, "Microvessel Organization and Structure in Experimental Brain Tumors: Microvessel Populations with Distinctive Structural and Functional Properties," Microvascular Research, vol. 58, pp. 312-328, 1999.

[17]   Josef Friedl, Ewa Turner, and H. R. Alexander, "Augmentation of endothelial cell monolayer permeability by hyperthermia but not tumor necrosis factor: Evidence for disruption of vascular integrity via VE-cadherin down-regulation," International Journal of Oncology, vol. 23, pp. 611-616, 2003.

[18]   V. V. Jeliazkova-Mecheva, W. C. Hymer, N. C. Nicholas, and D. J. Bobilya, "Brief heat shock affects the permeability and thermotolerance of an in vitro blood-brain barrier model of porcine brain microvascular endothelial cells," Microvascular Research, vol. 71, pp. 108-114, 2006.

[19]   L. v. Michael and et al., "Magnetically induced hyperthermia: size-dependent heating power of β-Fe 2 O 3 nanoparticles," Journal of Physics: Condensed Matter, vol. 20, p. 204133, 2008.

[20]   R. Hergt and S. Dutz, "Magnetic particle hyperthermia--biophysical limitations of a visionary tumour therapy," Journal of Magnetism and Magnetic Materials, vol. 311, pp. 187-192, 2007.

[21]   W. H. Suh, K. S. Suslick, G. D. Stucky, and Y.-H. Suh, "Nanotechnology, nanotoxicology, and neuroscience," Progress in Neurobiology, vol. 87, pp. 133-170, 2009.

[22]   S. N. Tabatabaei, J. Lapointe, and S. Martel, "Shrinkable Hydrogel-Based Magnetic Microrobots for Interventions in the Vascular Network," Advanced Robotics, vol. 25, pp. 1049-1067, 2011.

[23]   S. N. Tabatabaei, "Evaluation of hyperthermia using magnetic nanoparticles and alternating magnetic field," Master, Institute of Biomedical Engineering, University of Montreal, Montreal, 2010.

[24]   J.-H. Lee, J.-t. Jang, J.-s. Choi, S. H. Moon, S.-h. Noh, J.-w. Kim, J.-G. Kim, I.-S. Kim, K. I. Park, and J. Cheon, "Exchange-coupled magnetic nanoparticles for efficient heat induction," Nat Nano, vol. 6, pp. 418-422, 2011.

[25]   O. Pillai and R. Panchagnula, "Polymers in drug delivery," Current Opinion in Chemical Biology, vol. 5, pp. 447-451, 2001.

[26]   D. Jiles, Introduction to magnetism and magnetic materials, 1st ed. New York: Chapman and Hall, 1990.

[27]   C. Alexiou, W. Arnold, R. J. Klein, F. G. Parak, P. Hulin, C. Bergemann, W. Erhardt, S. Wagenpfeil, and A. S. L√ºbbe, "Locoregional Cancer Treatment with Magnetic Drug Targeting," Cancer Research, vol. 60, pp. 6641-6648, December 1, 2000 2000.

[28]   S. Martel, O. Felfoul, J.-B. Mathieu, A. Chanu, S. Tamaz, M. Mohammadi, M. Mankiewicz, and N. Tabatabaei, "MRI-based Medical Nanorobotic Platform for the Control of Magnetic Nanoparticles and Flagellated Bacteria for Target Interventions in Human Capillaries," The International Journal of Robotics Research, vol. 28, pp. 1169-1182, September 1, 2009 2009.

[29]   J. Lin and M. Lin, "Microwave hyperthermia-induced blood-brain barrier alterations," Radiation Research, vol. 89, pp. 77-87, 1982.

[30]   E. A. Kiyatkin and H. S. Sharma, "Permeability of the blood-brain barrier depends on brain temperature," Neuroscience, vol. 161, pp. 926-939, 2009.

[31]   J. Hed, C. Dahlgren, and I. Rundquist, "A simple fluorescence technique to stain the plasma membrane of human neutrophils," Histochemistry and Cell Biology, vol. 79, pp. 105-110, 1983.

[32]   E. Duguet, L. Hardel, and S. Vasseur, "Cell Targeting and Magnetically Induced Hyperthermia," in Thermal Nanosystems and Nanomaterials. vol. 118, S. Volz, Ed., ed: Springer Berlin / Heidelberg, 2009, pp. 343-365.

[33]   S. M. Moghimi, A. C. Hunter, and J. C. Murray, "Long-Circulating and Target-Specific Nanoparticles: Theory to Practice," Pharmacological Reviews, vol. 53, pp. 283-318, June 1, 2001 2001.

Reference – Article 2

[1] N. Joan Abbott, Blood–brain barrier structure and function and the challenges for CNS drug delivery, J. Inherit. Metab. Dis. 36 (3) (2013) 437–449. http://dx.doi.org/ 10.1007/s10545-013-9608-0.

[2] W.M.Pardridge, Drugtransportacrosstheblood–brainbarrier,J.Cereb.BloodFlow Metab. 32 (11) (2012) 1959–1972. http://dx.doi.org/10.1038/jcbfm.2012.126.

[3] Ravi Kant Upadhyay, Drug delivery systems, CNS protection, and the blood brain barrier, BioMed Res. Int. 2014 (2014)http://dx.doi.org/10.1155/2014/869269.

[4] P. Dames, B. Gleich, A. Flemmer, K. Hajek, N. Seidl, F. Wiekhorst, D. Eberbeck, I. Bittmann, C. Bergemann, T. Weyh, L. Trahms, J. Rosenecker, C. Rudolph, Targeted de- livery of magnetic aerosol droplets to the lung, Nat. Nanotechnol. 2 (8) (2007) 495–499. http://dx.doi.org/10.1038/nnano.2007.217.

[5] V.I. Shubayev, T.R. Pisanic II, S. Jin, Magnetic nanoparticles for theragnostics, Adv. Drug Deliv. Rev. 61 (6) (2009) 467–477. http://dx.doi.org/10.1016/j.addr.2009.03. 007.

[6] M. Nair, R. Guduru, P. Liang, J. Hong, V. Sagar, S. Khizroev, Externally controlled on-demand release of anti-HIV drug using magneto-electric nanoparticles as carriers, Nat. Commun. 4 (2013)http://dx.doi.org/10.1038/ncomms2717 (Article number: 1707).

[7] R. Qiao, Q. Jia, S.H. Wel, R. Xia, T. Liu, F. Gao, H.J. Galla, M. Gao, Receptor-mediated delivery of magnetic nanoparticles across the blood–brain barrier, ACS Nano 6 (4) (2012) 3304–3310. http://dx.doi.org/10.1021/nn300240p.

[8] E.A.Kiyatkin, H.S.Sharma, Permeability of the blood–brain barrier depends on brain temperature, Neuroscience 161 (3) (2009) 926–939. http://dx.doi.org/10.1016/j. neuroscience.2009.04.004.

[9] K.Dokladny, P.L.Moseley, T.Y.Ma, Physiologically relevant increase in temperature causes an increase in intestinal epithelial tight junction permeability, Am. J. Physiol. Gastrointest. Liver Physiol. 290 (2) (2006) G204–G212. http://dx.doi.org/10.1152/ ajpgi.00401.2005.

[10] S.N. Tabatabaei, S. Duchemin, H. Girouard, S. Martel, Towards MR-navigable nanorobotic carriers for drug delivery into the brain, IEEE Conf. Robot. Autom. 14 (2012) 727–732. http://dx.doi.org/10.1109/ICRA.2012.6225041.

[11] R.E. Rosensweig, Heating magnetic fluid with alternating magnetic field, J. Magn. Magn. Mater. 252 (2002) 370–374. http://dx.doi.org/10.1016/S0304-8853(02)00706-0.

[12] Q.A.Pankhurst, J.Connolly, S.K.Jones, J.Dobson, Applications of magnetic nanoparticles in biomedicine, J. Phys. D. Appl. Phys. 36 (13) (2003) R167–R181. http://dx.doi.org/10.1088/0022-3727/36/13/201.

[13] M. Wankhede, A. Bouras, M. Kaluzova, C.G. Hadjip, Magnetic nanoparticles: an emerging technology for malignant brain tumor imaging and therapy, Expert. Rev. Clin. Pharmacol. 5 (2) (2012) 173–186. http://dx.doi.org/10.1586/ecp.12.1.

[14] N. Joan Abbott, P.A. Revest, Control of brain endothelial permeability, Cerebrovasc.

Brain Metab. Rev. 3 (1) (1991) 39–72. [15] Hwa Jeong Lee, Yun Zhang, William M. Pardridge, Blood–brain barrier disruption following the internal carotid arterial perfusion of alkyl glycerols, J. Drug Target. 10 (6) (2002) 463–467. http://dx.doi.org/10.1080/1061186021000038337.

[16] K. Hynynen, N. McDannold, N. Vykhodtseva, F.A. Jolesz, Noninvasive MR imaging-guided focal opening of the blood–brain barrier in rabbits, Radiology 220 (3) (2001) 640–646. http://dx.doi.org/10.1148/radiol.2202001804.

[17] N. Sheikov, N. McDannold, S. Sharma, K. Hynynen, Effect of focused ultrasound applied with an ultrasound contrast agent on the tight junctional integrity of the brain microvascular endothelium, Ultrasound Med. Biol. 34 (7) (2008) 1093–1104. http://dx.doi.org/10.1016/j.ultrasmedbio.2007.12.015.

[18] P. Prentice, A. Cuschierp, K. Dholakia, M. Prausnitz, P. Campbell, Membrane disrup- tion by optically controlled microbubble cavitation, Nat. Phys. 1 (2005) 107–110. http://dx.doi.org/10.1038/nphys148.

[19] S. Wang, O.O. Olumolade, T. Sun, G. Samiotaki, E.E. Konofagou, Noninvasive, neuron-specific gene therapy can be facilitated by focused ultrasound and recombinant adeno-associated virus, Gene Ther. 22 (1) (2015) 104–110. http://dx.doi.org/10. 1038/gt.2014.91.

[20] P. Pouponneau, J.C. Leroux, G. Soulez, L. Gaboury, S. Martel, Co-encapsulation of magnetic nanoparticles and doxorubicin into biodegradable microcarriers for deep tissue targeting by vascular MRI navigation, Biomaterials 32 (13) (2011) 3481–3486. http://dx.doi.org/10.1016/j.biomaterials.2010.12.059.

[21] A. Hoffmann, J. Bredno, M. Wendland, N. Derugin, P. Ohara, High and low molecular weight fluorescein isothiocyanate (FITC)-dextrans to assess blood–brain barrier dis- ruption: technical considerations, Transl. Stroke Res. 2 (2011) 106–111. http://dx. doi.org/10.1007/s12975-010-0049-x.

[22] K.E. Sandoval, K.A. Witt, Blood–brain barrier tight junction permeability and ischemic stroke, Neurobiol. Dis. 32 (2) (2008) 200–219. http://dx.doi.org/10.1016/j. nbd.2008.08.005.

[23] R. Darwazeh, Y. Yan, Mild hypothermia as a treatment for central nervous system injuries: positive or negative effects, Neural Regen. Res. 8 (28) (2013) 2677–2686. http://dx.doi.org/10.3969/j.issn. 1673-5374.2013.28.010.

[24] M.M. Yallapu, Sh.F. Othman, E.T. Curtis, B.K. Gupta, M. J, S.C. Chauhan, Multi-functional magnetic nanoparticles for magnetic resonance imaging and cancer therapy, Biomaterials 32 (7) (2011) 1890–1905. http://dx.doi.org/10.1016/j. biomaterials.2010.11.028.

[25] M. Bramini, D. Ye, A. Hallerbach, M.N. Raghnaill, A. Salvati, C. Aberg, K.A. Dawson, Imaging approach to mechanistic study of nanoparticle interactions with the blood–brain barrier, ACS Nano 8 (5) (2014) 4304–4312. http://dx.doi.org/10. 1021/nn5018523.

[26] M. Olah, K. Biber, J. Vinet, H.W.G.M. Boddeke, Microglia phenotype diversity, CNS Neurol. Disord. Drug Targets 13 (10) (2014) 108–118.

[27] O. Veiseh, J.W. Gunn, M. Zhang, Design and fabrication of magnetic nanoparticles for targeted drug delivery and imaging, Adv. Drug Deliv. Rev. 62 (3) (2010) 284–304. http://dx.doi.org/10.1016/j.addr.2009.

[28] A. Amirfazli, Nanomedicine: magnetic nanoparticles hit the target, Nat. Nanotechnol. 2 (8) (2007) 467–468. http://dx.doi.org/10.1038/nnano.2007.234.

[29] W. Rao, Z.S. Deng, J. Liu, Review of hyperthermia combined with radiotherapy/chemotherapy on malignant tumors, Crit. Rev. Biomed. Eng. 38 (1) (2010) 101–116.

[30] L. Momtazi, S. Bagherifam, G. Singh, A. Hofgaard, M. Hakkarainen, W.R. Glomm, N. Roos, G.M. Maelandsmo, G. Griffiths, B. Nystrom, Synthesis, characterization, and cellular uptake of magnetic nanocarriers for cancer drug delivery, J. Colloid Interface Sci. 433C (2014) 76–85. http://dx.doi.org/10.1016/j.jcis.2014.07.013.

[31] W.H. Suh, Nanotechnology, nanotoxicology, and neuroscience, Prog. Neurobiol. 87 (3) (2009) 133–170. http://dx.doi.org/10.1016/j.pneurobio.2008.09.009.

[32] J. Jiang, G. Oberdorster, P. Biswas, Characterization of size, surface charge, and agglomeration state of nanoparticle dispersions for toxicological studies, J. Nanoparti- cle Res. 11 (1) (2009) 77–89. http://dx.doi.org/10.1007/s11051-008-9446-4.

[33] C.R. Lin, R.K. Chiang, Magnetic properties of monodisperse iron oxide nanoparticles (J. App. Phys), Vol. 99 (2006)http://dx.doi.org/10.1063/1.2172891 08 N710.

[34] P.A. Khandhar, R.M. Ferguson, J.A. Simon, K.M. Krishnan, Enhancing cancer therapeutics using size-optimized magnetic fluid hyperthermia, J. Appl. Phys. 111 (2012) 07B306. http://dx.doi.org/10.1063/1.3671427.

[35] W. Prentice, Arnheim's Principles of Athletic Training: a Competency-Based Approach, McGraw-Hill, New York, 2006.

[36] ICNIRP, Guidelines for limiting exposure to time-varying electric, magnetic, and electromagnetic fields (up to 300 gHz), Health Phys. 74 (1998) 494–522.

[37] C. Polk, E. Postow, Handbook of Biological Effects of Electromagnetic Fields, CRC Press, Florida, 1995.

[38] P.Y. Wen, S. Kesari, Malignant gliomas in adults, N. Engl. J. Med. 359 (2008) 492–507. http://dx.doi.org/10.1056/NEJMra0708126.

[39] D.N. Louis, H. Ohgaki, O.D. Wiestler, W.K. Cavenee, P.C. Burger, A. Jouvet, B.W. Scheithauer, P. Kleihues, The 2007 WHO classification of tumors of the central nervous system, Acta Neuropathol. 114 (2) (2007) 97–109. http://dx.doi.org/10.1007/ s00401-007-0243-4.

[40] W.L. Jiang, H. Xie, D. Ghoorah, Y. Shang, H. Shi, F. Liu, X. Yang, H. Xu, Conjugation of functionalized SPIONs with transferrin for targeting and imaging brain glial tumors in rat model, PLoS One 7 (5) (2012) e37376. http://dx.doi.org/10.1371/journal.pone. 0037376.

[41] J.H. Lee, J.T. Jang, J.S. Choi, S.H. Moon, S.H. Noh, J.W. Kim, J.G. Kim, I.S. Kim, K.I. Park, J. Cheon, Exchange-coupled magnetic nanoparticles for efficient heat induction, Nat. Nanotechnol. 6 (7) (2011) 418–422. http://dx.doi.org/10.1038/nnano.2011.95.

Reference – Appendix B

 [1] Polk, C., Postow, E. Handbook of Biological Effects of Electromagnetic Fields (Florida, CRC Press, 1995)

[2] Freitas, R. A. J. Nanomedicine vol. Basic Capabilities (Georgetown, TX: Landes Bioscience, 1999)

APPENDIX A – MATLAB [®] PROGRAMING CODE

A1   Figure 2.9: Relaxation time vs. Particle size for MNPs

```matlab
u_0=pi*4e-7;                        % volts.second/amp/meter
Anisotropy = 2.64e4;                %J m^-3 for magnetite
Temperature = 297;                  %Kelvin room temperature
Viscosity=1e-3;                     %Pa.s (kg/m/s);
t_0=1e-9;
k=1.38e-23;                         % J/K (Boltzman Constant)(J=w.s)
Density = 5.18;                     %g/cm^3 for Magnetite
Ms_VSM =60;                         %emu/g
Ms = Ms_VSM * Density * 1e3;        %A/m
Coating = 40e-9;                    %meter
Radius = 5e-9:1e-9:10e-9;           %nm


for r=1:length(Radius)

    volume(r) = Volume(Radius(r));

    %%% t_Neel

    GAMMA(r) = Anisotropy * volume(r) / k / Temperature;

    t_Neel(r) = (sqrt(pi) / 2) * t_0 * exp(GAMMA(r))/((GAMMA(r))^(1/2));

    %%%% Brownian relaxation

    volume_hydro(r) = volume(r) * (1 + Coating/Radius(r))^3 ;

    t_Brownian(r) = 3 * Viscosity * volume_hydro(r)/k/Temperature;

    %%% t_effect

    t_effect(r) = t_Neel(r) * t_Brownian(r) /(t_Neel(r) + t_Brownian(r));

end

semilogy (Radius, t_Brownian,'r','Linewidth',3)
hold on
semilogy (Radius, t_Neel,'b','Linewidth',3)
hold on
semilogy (Radius, t_effect,'g','Linewidth',3)

title('Relaxation time vs. Particle size for MNP', 'FontSize',15)
ylabel('\tau(s)','FontSize',15);
xlabel('Particle Radius (m)','FontSize',15);
text(8.6e-9, 1, '\tau_N_e_e_l', 'FontSize',15)
text(5.5e-9, 1e-4, '\tau_B_r_o_w_n_i_a_n', 'FontSize',15)
text(9e-9, 9e-5, '\tau_e_f_f_e_c_t', 'FontSize',15)
set(gca,'FontSize',14);
grid on
```

A.2   Figure 2.12: Susceptibility components vs. Frequency

```matlab
%%% Stoner-Wohlfarth Losses for small particles

u_0=pi*4e-7;                        % volts.second/amp/meter

Aisotropy = 2.64e4;                 %J m^-3 for magnetite
Temperature = 297;                  %Kelvin room temperature
Viscosity=1e-3;                     %Pa.s (kg/m/s) for ferrofluids
volume_fraction=0.071;              %volume fraction solid
Density = 5.18;                     %g/cm^3 for Magnetite
Ms_VSM =60;                         %emu/g
Ms = Ms_VSM * Density * 1e3         %A/m
Radius = 6e-9;                      %meter
Md = Ms / volume_fraction

volume = Volume(Radius);
Field = 10e3;                       %A/m
Coating = 40e-9;                    %meter
frequency = 0:1e5:1e7;              %Hz



%Hydrodynamic diameter = shell thickness + core diameter + shell thickness =
20 nm + 10 nm + 20 nm = 50 nm



t_Neel = t_Neel(u_0, Anisotropy, Ms,volume,Temperature)
t_Brownian = t_Brownian(Viscosity, volume, Radius, Temperature, Coating)
t_effect = t_effect(t_Neel, t_Brownian);

for f=1:length(frequency)

    Phi(f) = t_effect * 2 * pi * frequency(f);          %dimentionless
    Initial_Susc = Initial_Susceptibility (Ms,volume,volume_fraction,
    Temperature);                                        %dimensionless
    DC_Susc = DC_Susceptibility (Initial_Susc, Field, volume_fraction, Ms ,
    volume,Temperature);
    Susc(f) = Susceptibility (DC_Susc,Phi(f));
    sus_real(f) = DC_Susc / (1+(Phi(f))^2);
    sus_img(f) = Phi(f)* DC_Susc / (1+(Phi(f))^2);

end

semilogx (frequency, sus_img/DC_Susc,'r','Linewidth',3)
hold on
semilogx (frequency, real(sus_real/DC_Susc),'b','Linewidth',3)
title('Susceptibility components vs. Frequency', 'FontSize',15)
ylabel('\chi/\chi_0','FontSize',15);
xlabel('Frequency (Hz)','FontSize',15);
text(7e5, 0.4, '\chi_i_m_a_g_i_n_a_r_y', 'FontSize',15)
text(8e5, 0.8, '\chi_r_e_a_l', 'FontSize',15)
set(gca,'FontSize',14);
grid on;
```

A.3 Figure 2.14: Power loss due to Neel relaxation vs. Radius of MNPs

```matlab
%%%%%%%%%%%%%%%%%%%%%%%%%
%%% Grain size dependence
%%% of the loss power denisty
%%% due to Neel-relaxation
%%% for small magnetite
%%%%%%%%%%%%%%%%%%%%%%%%%


%%% SAR_Neel = (u0 f pi x0 (H)^2 2pi f t / [rho (1+(wt)^2)]
%%% w = Angular_Freq
%%% t = t_Neel


clc
clear all


k=1.38e-23;                            % J/K (Boltzman Constant)(J=w.s)
K=1.18e4;                              % Shape anisotropy Fe3O4 J/m^3 aspect
ratio of 1.4
u_0=pi*4e-7;                           % volts.second/amp/meter
Temperature = 273+37;                  % Kelvin (Body temperature)
volume_fraction=0.071;                 % volume fraction solid
Density = 5.18;                        % g/cm^3
H_field = 82.0;                        % Oe = 6.5 kA/m
Magnetization = 40;                    % @ H = 82 Oe, (emu /g)
Ms_emu_g = 90;                         % Magnetization saturation (emu/g)
Ms = Ms_emu_g * Density * 1e3;         % A/m
t_0 = 1e-10;
Radius = 7e-9:1e-10:12e-9;             % meter
Frequency = [2e4,2e5,2e6];             % Hz

for i=1:length(Radius)


    Volume(i)=4/3 * pi * (Radius(i))^3;                        % m^3
    t_Neel(i) = t_0 * exp(K * Volume(i)/k/Temperature);       % second

    %domain magnetization of a suspended particle
    Md = Ms / volume_fraction;

    %from Langevin relationship:
    Initial_Susc(i) = u_0 * volume_fraction * (Md^2) * volume(i) / 3 / k /
Temperature;

    xi(i) =  u_0* Md * H_field * volume(i) / k / Temperature; %dimensionless
    DC_Susc(i) = Initial_Susc(i) * 3 * (coth (xi(i)) - (1/xi(i))) / xi(i);

    for f=1:length(Frequency)
```

```
        Angular_Freq(f) = 2 * pi * Frequency(f);        % radian

        A=u_0*Frequency(f)*H_field^2*pi*DC_Susc(i)*Angular_Freq(f)*t_Neel(i);

        B=1+(Angular_Freq(f)*t_Neel(i))^2;

        SAR(i,f)=A/B/Density/1e6;

    end

end

semilogy (Radius,SAR,'Linewidth',1.5);
ylabel('SAR (W/g)','FontSize',15);
xlabel('Radius (m)','FontSize',15);
text(6.5e-9,3e1,'f = 2x10^6 Hz \rightarrow','FontSize',14);
text(7.6e-9,3,'f = 2x10^5 Hz \rightarrow','FontSize',14);
text(8.2e-9,0.2,'f = 2x10^4 Hz \rightarrow','FontSize',14);
set(gca,'FontSize',14);
%print -djpeg -r300 SARvsParticle_Jpeg_REVISED!!!
```

A.4   Figure 2.15: Biological limitation to field and frequency

```
%%%%%%%%%%%%%%%%%%%%%%%%%%%%%%%%%%%%%%%
% this will calculate the amount of
% SAR that is absorbed by body tissue
%%%%%%%%%%%%%%%%%%%%%%%%%%%%%%%%%%%%%%%
%%
u0 = pi*4e-7;              % permeability of vacuum (H/m)
u  = 100*u0;              % permeability of  (H/m)
Conductivity = 0.6;       % tissue conductivity (ohm^-1 m^-1)
Radius = 10;              % radius of the region EMF is applied on (cm)

density=0.8;             %average tissue density (g/cm^3)


%limitation set by 'Usable Frequencies for Hyperthemria with Thermal
%Seeds' --> 13.56 MHz at 35.8 A/m  for extended time --> 25 mW/ml


Limit = 0.025;            %SAR (W/ml) or (W/cm^3)
                          %Ref: Usable Frequencies in Hyperthermia with
                          %Thermal Seeds: limit H0f <=  4.85x10^8 A/m/s
% The resulting SAR value is
% unlikely to produce a localized temperature increment of
% more than 1°C in the limbs (Chatterjee et al. 1986; Chen
% and Gandhi 1988; Hoque and Gandhi 1988), which has
% been suggested as the upper limit of temperature increase
% that has no detrimental health effects (UNEP/WHO/
% IRPA 1993).
% In general, these have
% demonstrated that exposure for up to 30 min, under
% conditions in which whole-body SAR was less than
% 4 W/kg, caused an increase in the body core temperature
% of less than 1°C.


% Summary of biological effects and epidemiological
% studies (100 kHz–300 GHz)


% Available experimental evidence indicates that the
% exposure of resting humans for approximately 30 min to
% EMF producing a whole-body SAR of between
% 1 and 4 W/kg results in a body temperature increase of
% less than 1 °C. Animal data indicate a threshold for
% behavioral responses in the same SAR range. Exposure
% to more intense fields, producing SAR values in excess
% of 4 W/kg, can overwhelm the thermoregulatory
% capacity of the body and produce harmful levels of tissue
% heating. Many laboratory studies with rodent and nonhuman
% primate models have demonstrated the broad
% range of tissue damage resulting from either partial-body
% or whole-body heating producing temperature rises in
% excess of 1–2°C. The sensitivity of various types of
% tissue to thermal damage varies widely, but the threshold
% for irreversible effects in even the most sensitive tissues
% is greater than 4 W/kg under normal environmental
% conditions. These data form the basis for an occupational
% exposure restriction of 0.4 W/kg, which provides a
```

```matlab
% large margin of safety for other limiting conditions such
% as high ambient temperature, humidity, or level of
% physical activity.

%initializing vectors of frequency and field amplitude
freq=[];
field=[];


H_field=1e3:1e2:10e3;        %initial to final field (A/m)

for i=1:length(H_field)

    A=0;                     %initial to final (Hz)
    B=1e6;
    Frequency=A:1e4:B;


    for ii=1:length(Frequency)


        w(ii) = 2*pi*Frequency(ii);      %angular frequency

        %W/cm^3
        P_N(i,ii) =   1e-
6*(w(ii)^2)*(u0^2)*(Conductivity/8)*(H_field(i))^2*(Radius*1e-2)^2;

        %W/g
        P_N_2(i,ii)=P_N(i,ii)/density;

          if P_N(i,ii) <= Limit && P_N(i,ii) >= (Limit-1e-3)

            freq = [freq; Frequency(ii)];
            field = [field; H_field(i)];


          end

    end

end

plot (freq,field,'LineWidth',2);
grid on;
xlabel('Frequency (Hz)','FontSize',15);
ylabel('Field (A/m)','FontSize',15);
title(['Field vs. Frequency for Loss Power limit of ',num2str(Limit*1000),'
mW/ml'],'FontSize',15)
text(2e5,8000,'Radius of the applied AC magnetic field = 10
cm','FontSize',14);
text(1.6e5,4800,'\leftarrow f = 160 kHz ','FontSize',14);
text(1.9e5,4200,'H = 4.5 kA/m','FontSize',14);
set(gca,'FontSize',14);
```

<div align="center">**APPENDIX B – SUPPLEMENTARY INFORMATION**</div>

B1. Magnetic Nanoparticles Heating Ability

Magnetite nanoparticles (MNPs) purchased from Chemicell GmbH came in eight different coatings; Starch, Oleic acid, Polyacrylic acid, Poly (maleic acid-co-olefin), Polyvinyl alcohol, SiMAG Carboxyl and two types of uncoated MNP: anionic and cationic charge. Each sample was placed in a 2 kW induction heating machine. The primary purpose of this experiment was to see how various coatings would influence the temperature rise of the MNPs. Therefore, 0.5 ml MNP samples of the various coatings with a concentration of 12 mg Fe_3O_4 mL^{-1} in distilled water were prepared in separate eppendorfs. Each sample was placed in a custom made isolation foam (Styrofoam) fitted to the inside of the copper tube coil. This coil was designed to generate a radiofrequency (RF) field strength of 2 kA m^{-1} at 160 kHz. A fibre optic temperature sensor (Reflex, SN: T18 217A, Neoptix Inc, QC, Canada) recorded temperatures of the sample at the center of the eppendorf every 15 seconds for a total time of 3000 seconds. A control sample containing deionised water was placed inside the coil to measure the effect of the RF field on the thermocouple, the eppendorf and the isolation foam. This effect was found to be negligible. Temperature increments as a function of time for all samples are depicted in Appendix B, S. 1. The images provided by Transmission Electron Microscopy (TEM) are presented below in Appendix B, S. 2 and show that some nanoparticles have different shapes and core size distribution than others. For these MNPs, the crystal diffraction patterns corresponded to magnetite (Fe_3O_4) composition (Appendix B, S. 5). The M - H curves provided by Vibrating Sample Magnetometer (VSM) show very narrow hysteresis losses and in some cases a complete lack of hysteresis losses is evident. These curves are depicted below in Appendix B, S. 3. From the images of TEM, the diameters of more than 630 single PMO coated particles were measured and recorded. The results are depicted in Appendix B, S. 4 and show a relatively wide size distribution ranging approximately from 3 - 18 nm in diameter, peaking at 11 and 13 nm.

B2. Limitations To The RF Field Parameters

In Figure S6, the curve represents the upper limit for field amplitude and frequency that can be used for patients with a body (head) cross section of 10 centimeters in radius at tissue load limit

of 25 mW/cm. This simulation also took into account values for biological tissue conductivity ranging from 0.0144 S/m to 0.68 S/m as tabulated in [1] for frequencies in the range of 100 kHz to 1 MHz. Since eddy current power density is proportional to the square of the diameter of the induced current loops, the proposed upper limit can be accordingly larger for smaller body regions under RF field exposure.

When an electromagnetic wave passes through the human body, as it heats the tissue it also declines in intensity. This is given by

$$I = I_0 \exp\left(-2 \propto_E x\right) \qquad\qquad (\mathrm{W\,m^{-2}})$$

$$I_0 < 100 \quad (\mathrm{W\,m^{-2}}) \text{ maximum safe incident intensity} \qquad\qquad \propto_E = \propto_e n_E^{1/2}$$

Where I is the power per unit area transmitted through the tissue, x is the penetration depth of the tissue, α_E is the total attenuation factor including scattering and absorption. n_E is the incident frequency and α_e averages about 5 x 10^{-3} $\sec^{1/2}$/m for soft tissue [2].

To simplify calculations, here the biological load is assumed to be isotropic and homogeneous and it's cross section exhibits cylindrical symmetry to the induction coil. Also the RF field within the coil and tissue load is assumed to be uniform and field penetration into the dielectric material is complete. Moreover, the tissue under study is far away from any metallic implants that could affect the field in any way. Last but not least, it is assumed that there is no axial electric field within the coil.
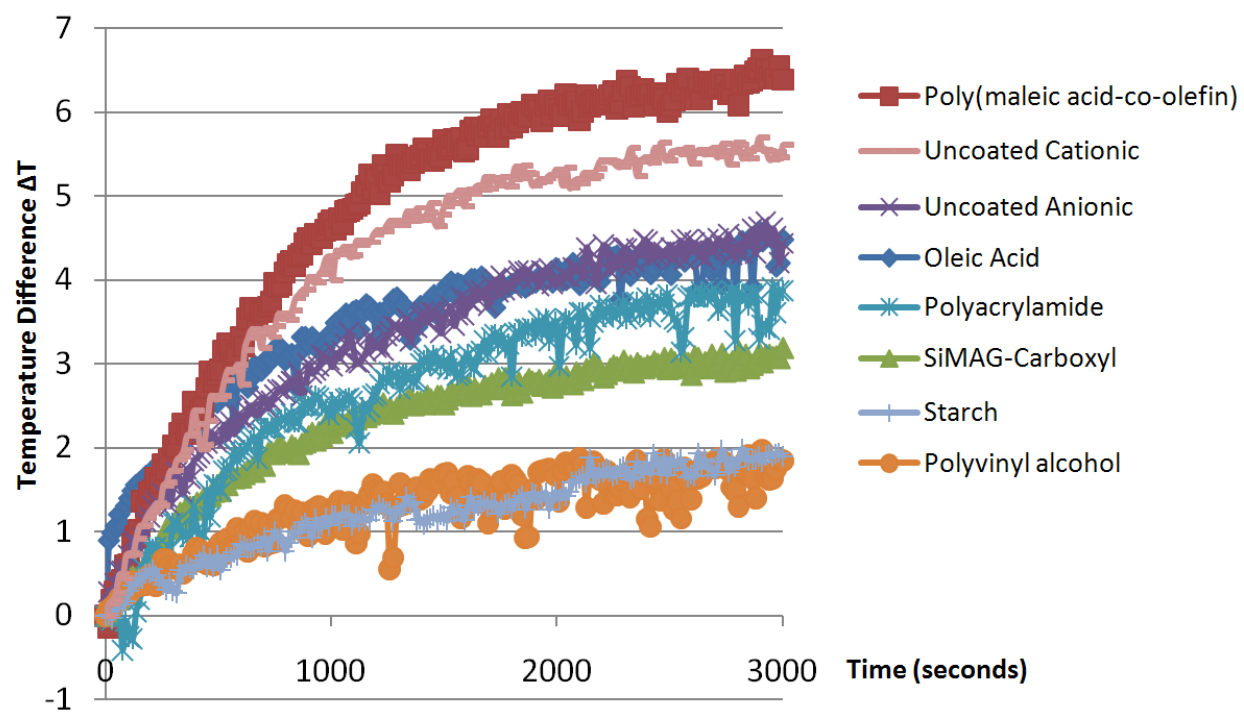
Appendix B, S. 1 - Temperature profile for MNPs with eight different coatings
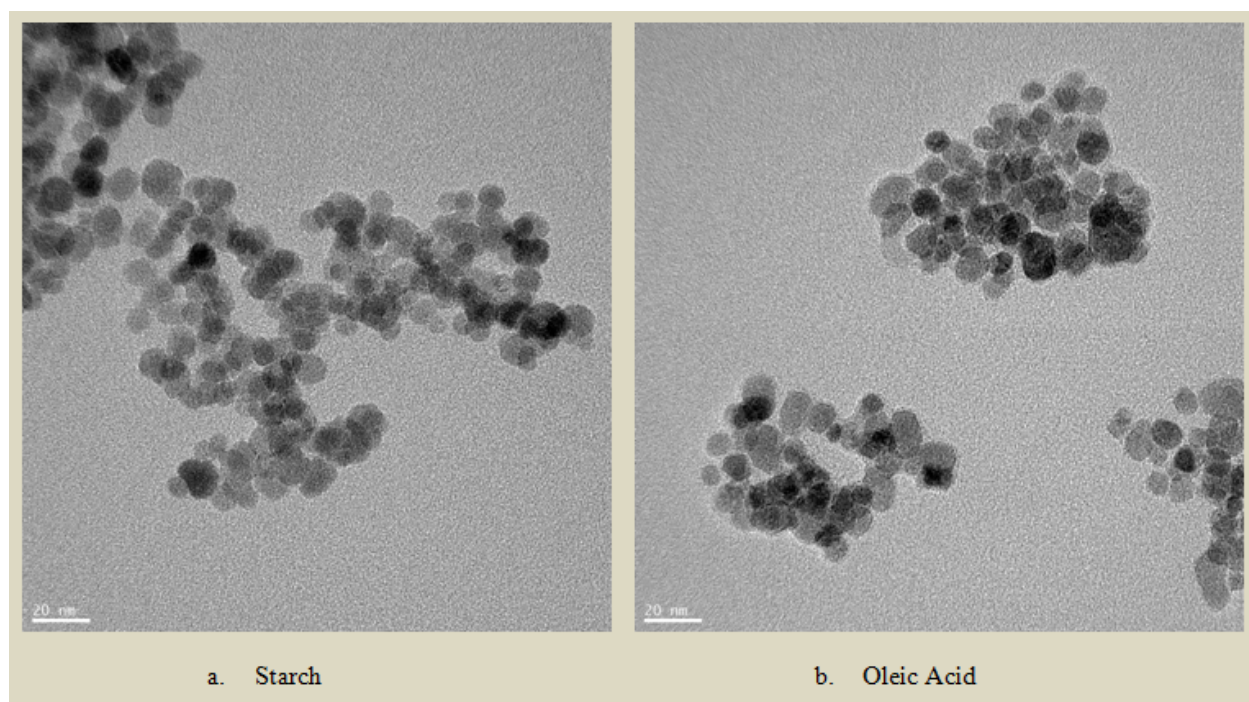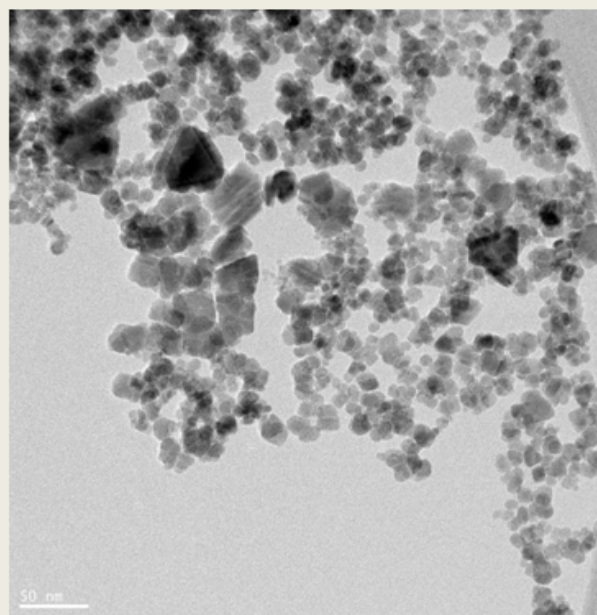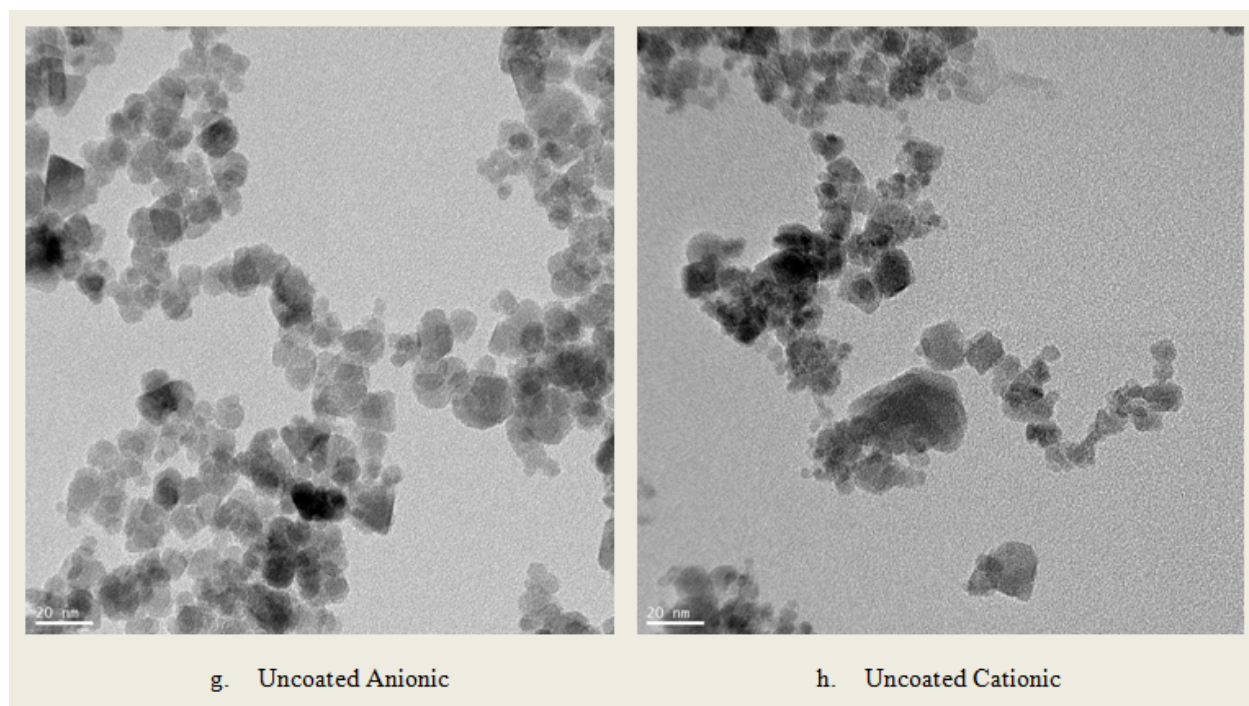
c.   Polyacrylamide
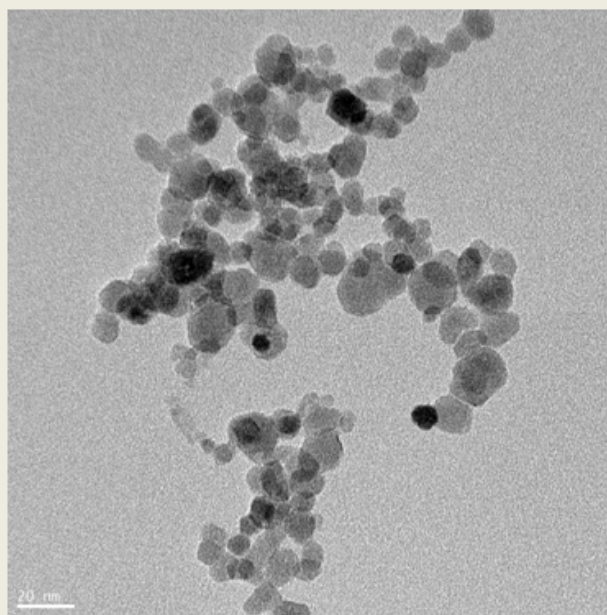
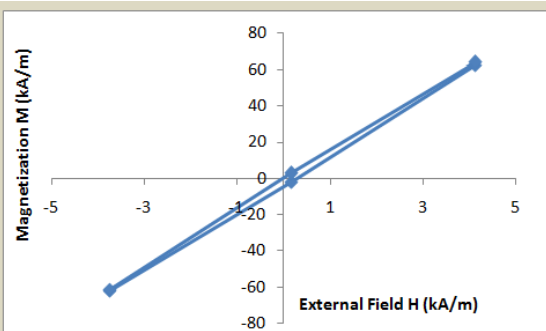d.   Poly(maleic acid-co-olefin)
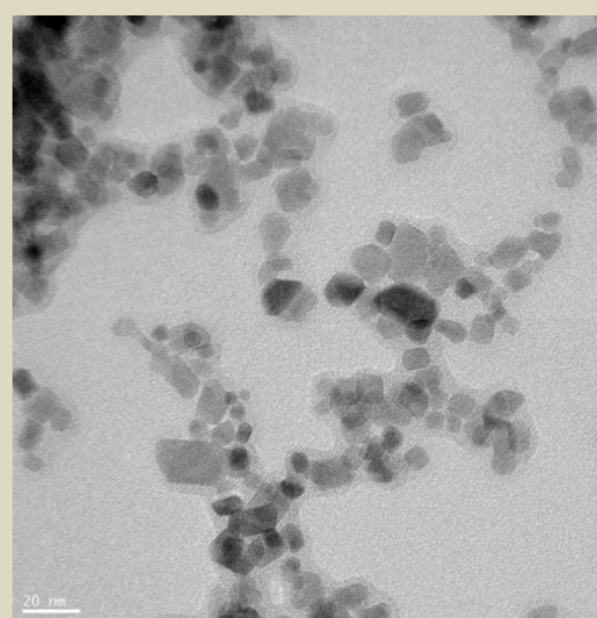
e.   Polyvinyl alcohol
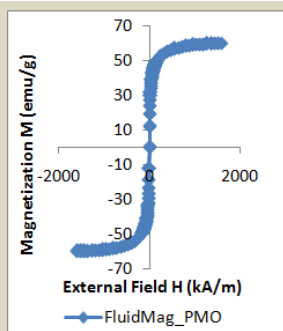

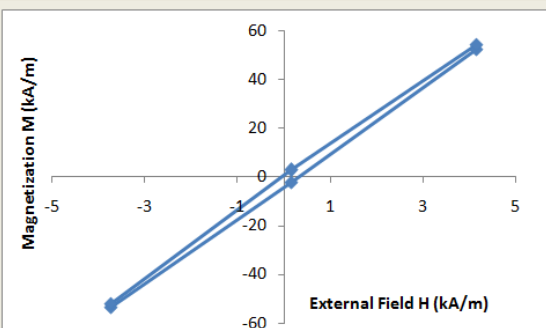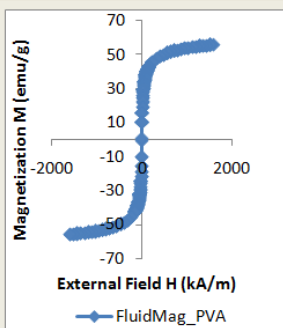f.   SiMAG, Carboxyl

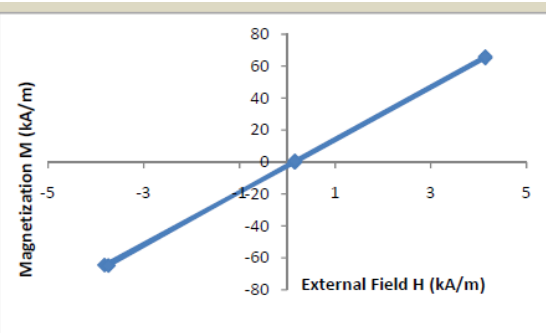g. Uncoated Anionic   h. Uncoated Cationic
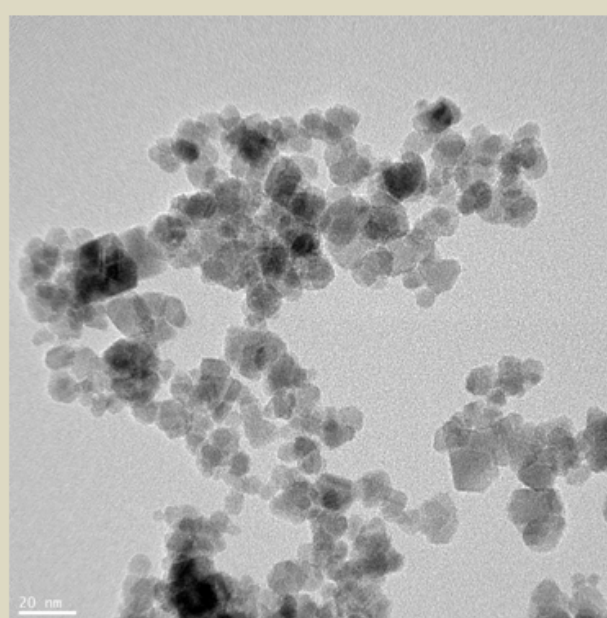
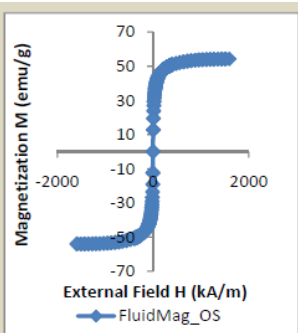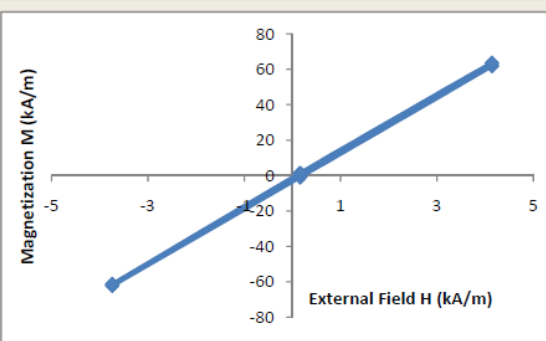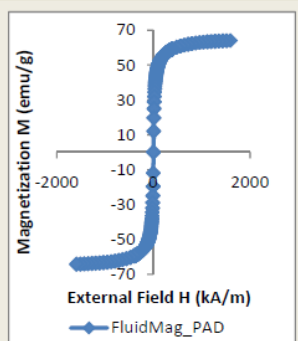Appendix B, S. 2 - TEM images of different coatings
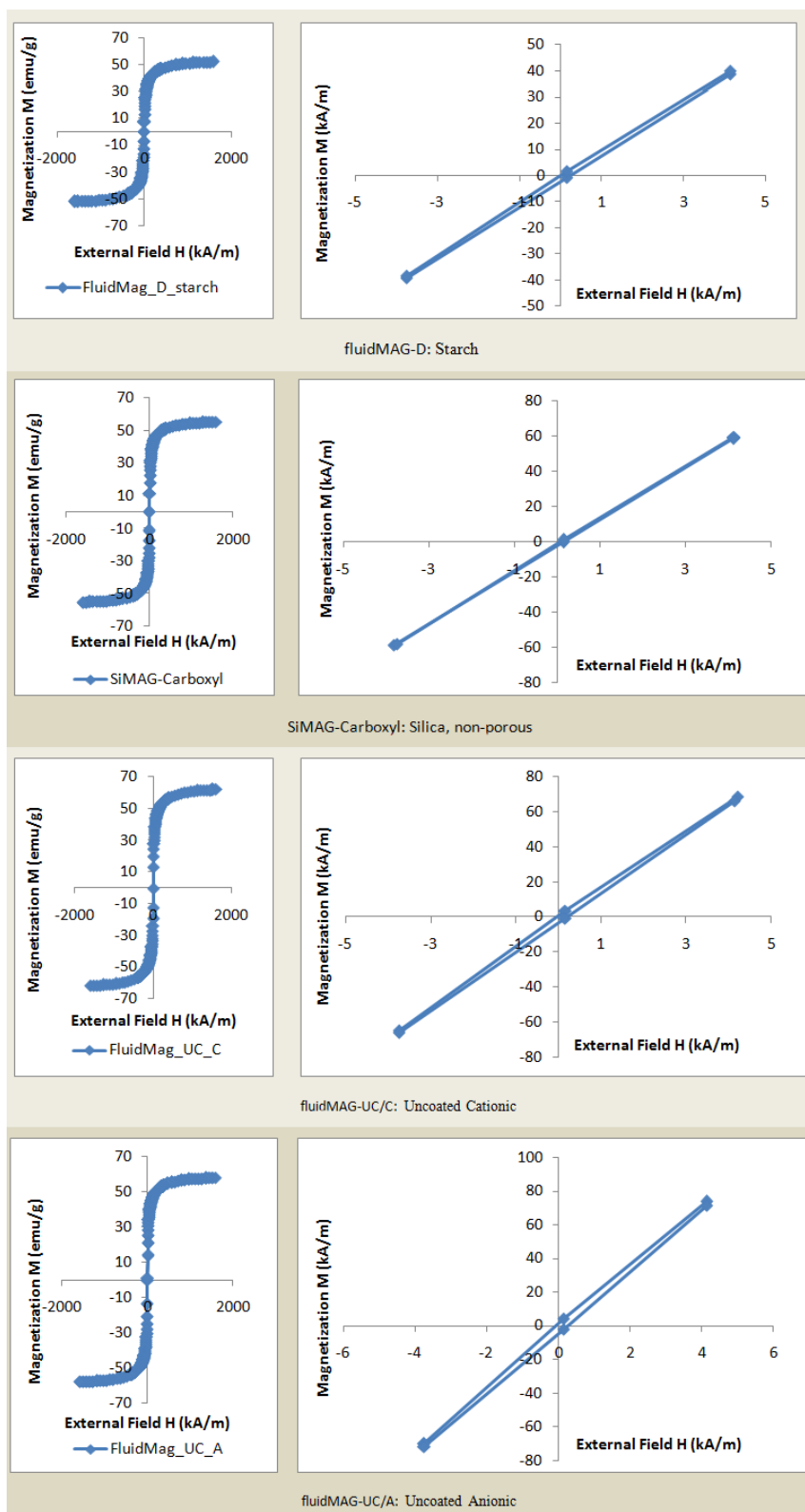
fluidMAG-PMO: Poly(maleic acid-co-olefin)

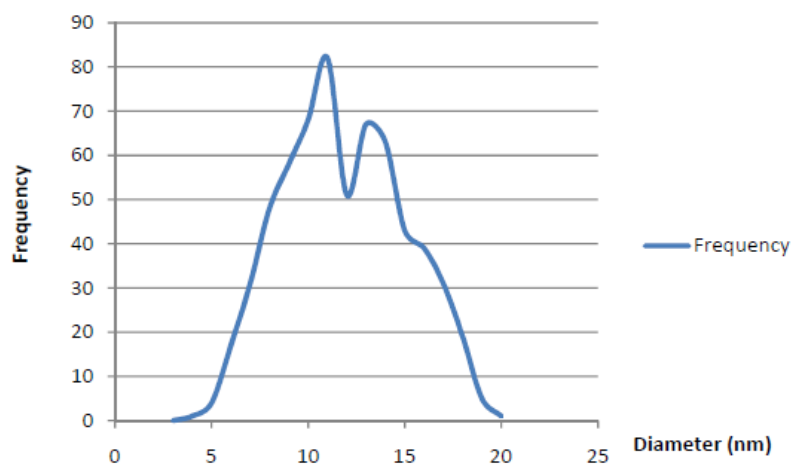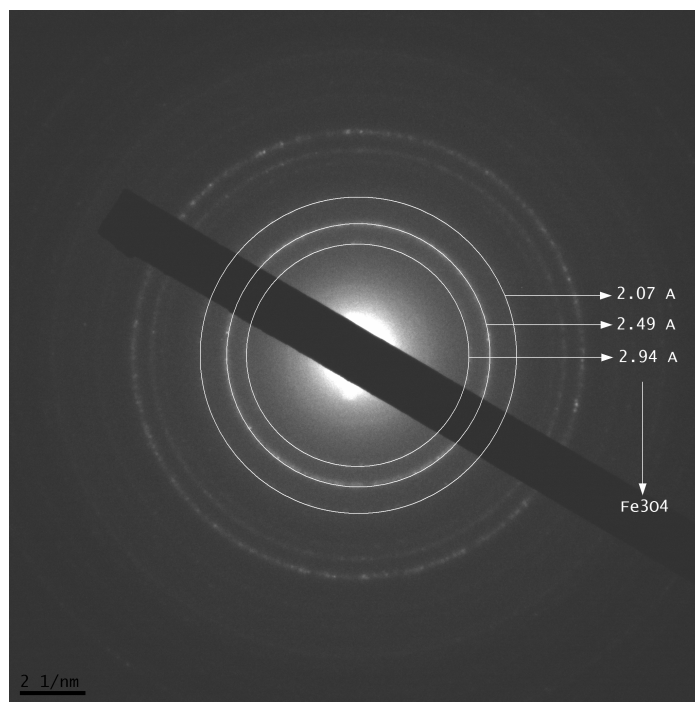fluidMAG-PVA: Polyvinyl alcohol

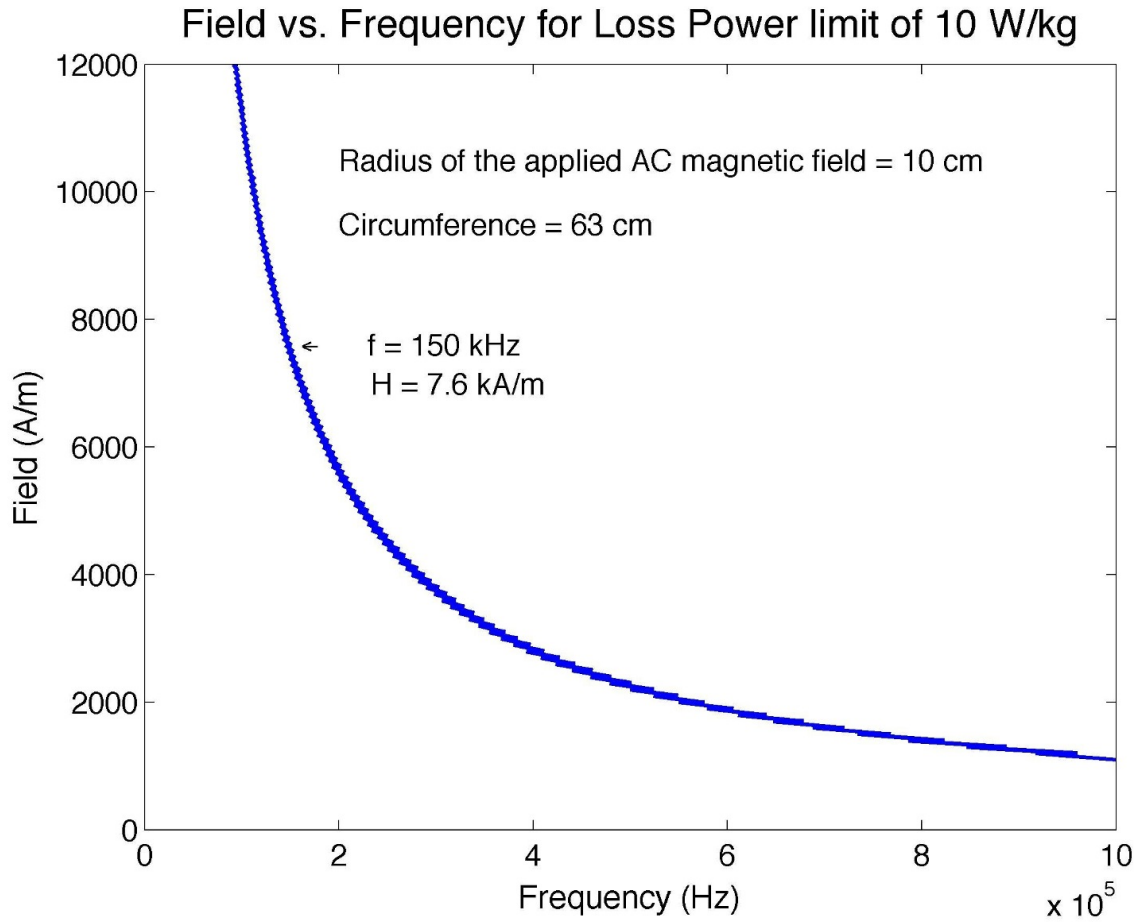fluidMAG-OS: Oleic Acid

fluidMAG-PAD Polyacrylamide

Appendix B, S. 3 - VSM images of different coatings

Appendix B, S. 4 - Size distribution for the PMO – MNPs using Transmission Electron Microscopy imaging

Appendix B, S. 5 - X-Ray diffraction for the PMO coated iron oxide nanoparticles

Field vs. Frequency for Loss Power limit of 10 W/kg

Radius of the applied AC magnetic field = 10 cm

Circumference = 63 cm

f = 150 kHz
H = 7.6 kA/m

Field (A/m)

Frequency (Hz)

x 10^5

Appendix B, S. 6 - Biological limitation to RF field amplitude and frequency